

Dynamical phase transitions in the nonreciprocal Ising model

Yael Avni,¹ Michel Fruchart,² David Martin,³ Daniel Seara,¹ and Vincenzo Vitelli^{1,4}

¹*University of Chicago, James Franck Institute, 929 E 57th Street, Chicago, IL 60637*

²*Gulliver, ESPCI Paris, Université PSL, CNRS, 75005 Paris, France*

³*University of Chicago, Kadanoff Center for Theoretical Physics and Enrico Fermi Institute, 933 E 56th St, Chicago, IL 60637*

⁴*University of Chicago, Kadanoff Center for Theoretical Physics, 933 E 56th St, Chicago, IL 60637*

Nonreciprocal interactions in many-body systems lead to time-dependent states, commonly observed in biological, chemical, and ecological systems. The stability of these states in the thermodynamic limit and the critical behavior of the phase transition from static to time-dependent states are not yet fully understood. To address these questions, we study a minimalistic system endowed with nonreciprocal interactions: an Ising model with two spin species having opposing goals. The mean-field equation predicts three stable phases: disorder, static order, and a time-dependent swap phase. Large scale numerical simulations support the following: (i) in 2D, the swap phase is destabilized by defects; (ii) in 3D, the swap phase is stable, and has the properties of a time crystal; (iii) the transition from disorder to swap in 3D is characterized by the critical exponents of the 3D XY model, and corresponds to the breaking of a continuous symmetry, time translation invariance; (iv) when the two species have fully anti-symmetric couplings, the static-order phase is unstable in any finite dimension due to droplet growth; (v) in the general case of asymmetric couplings, static order can be restored by a droplet-capture mechanism preventing the droplets from growing indefinitely. We provide details on the full phase diagram which includes first- and second-order-like phase transitions and study how the system coarsens into swap and static-order states.

I. INTRODUCTION

Many-body systems with nonreciprocal interactions emerge in contexts ranging from neuroscience [1–3] and social networks [4–6] to ecology [7–10] and open quantum systems [11–13]. These systems exhibit rich collective behavior including time-dependent states that can arise because the dynamics does not follow from the minimization of a single potential function [14–21]. However, it remains unknown whether these time-dependent states can be thought of as proper non-equilibrium phases of matter, in the sense of the term used in statistical physics; and if so, whether they exhibit well-defined phase transitions and critical behavior. In particular, we are interested in the fate of these time-dependent states in systems made of locally coupled units subject to thermal noise in finite spatial dimensions when they are taken to the thermodynamic limit.

In order to address this question, we consider a nonreciprocal version of the Ising model, in which two species of spins have incompatible goals: spins of species A tend to align with spins of species B, while spins B tend to anti-align with spins A. This leads to a cyclic dynamics where spins of each species tend to flip in turn. We study this system through analytical arguments and extensive Monte-Carlo simulations. A short account of our results is presented in Letter form in Ref. [22]; we summarize here the most salient points. First, numerical simulations indicate that in our model, a time-dependent phase with long-range spatial and temporal order indeed exists in three spatial dimensions. In this phase, the magnetization oscillates for arbitrarily long times. The system acts as a perfect clock in the thermodynamic limit, in the sense that the coherence time of the oscillations diverges with the size of the system. Second, a continu-

ous phase transition between this oscillatory phase and a disordered (*i.e.* paramagnetic) phase, corresponding to a Hopf bifurcation in mean-field, is observed. Numerical evidence shows that it is associated with scale invariance, and the corresponding static critical exponents are compatible with the 3D XY universality class. Third, we found that a static ordered phase (similar to a ferromagnetic phase) can exist when nonreciprocal interactions are present, but only if there is some symmetric coupling between the species. However, we found no evidence of a direct transition between the oscillatory phase and the static-order phase, in contrast with mean-field predictions.

II. BACKGROUND

The following section provides background and context on different aspects related to our work, as well as relations to existing literature. It can be skipped on first reading.

A. Nonreciprocal interactions between groups

There is a rich literature on nonequilibrium lattice models, including variants of the Ising model with asymmetric couplings exhibiting a variety of complex phenomena [23–27]. A distinguishing feature of the nonreciprocal Ising model introduced in this paper is the presence of macroscopic nonreciprocal interactions between two groups of spins of comparable sizes. This is a rather generic feature that arises in a variety of physical contexts, some of which can be captured by Ising or Ising-like minimal models. Examples include:

- *Nonlinear parametric resonators*, that can be mapped to Ising spins. Networks of coupled parametric oscillators have been used as platforms to realize (reciprocal) “Ising machines” that solve combinatorial optimization problems [28–34]. This is essentially because a single of these resonators implements a double-well potential, and a linear coupling effectively produces a (reciprocal) Ising-like coupling. Reference [35] shows experimentally and analytically that driven non-identical parametric resonators can be mapped into nonreciprocally coupled Ising spins. A network of such resonators could directly realize the nonreciprocal Ising model discussed in the present work, as well as implement models of learning with nonreciprocal couplings between the artificial neurons [2, 3, 36–40].
- *Models of collective opinion dynamics*, such as in the voter model [23, 41], where the values of the spins represent different opinions. Different communities may have asymmetric interactions: for instance, this is the case of conformists and contrarians (or alternatively trendsetters) [41–49]. Similarly, spin models have been used to model game theory and decision making of economic agents [6].
- *Models of the collective response of transmembrane receptors*, that have been put forward for the high sensitivity of cells to external chemicals in chemotaxis [50–54]. It has been argued that nonreciprocal couplings between the receptors and the kinases that serve as an output signal is required to account for experimental observations [55–57].
- *Models of neurons* based on networks of spins, such as the Hopfield model [58, 59], can contain asymmetric interactions [1–3, 36, 60–63], that account not only for existence of asymmetric neural connections but also for the presence of different groups of neurons called excitatory and inhibitory, which correspond to different signs of the couplings [36, 64]. This approach has also been extended to larger brain structures like different brain regions: active/non-active regions are represented by spin variables while their interaction is mimicked by the spin alignment interaction [65].
- *Models of spinor Bose-Einstein condensates* based on two populations of Ising spins in a cavity (a Dicke model) that effectively interact nonreciprocally have been considered [11, 66, 67] to account for non-stationary dynamics observed in experiments [68].
- *Model inference* in which symmetric and asymmetric Ising models have also been used as a variational ansatz [37, 69–72].

In several of these classes of systems, it has been conjectured that criticality may play a nontrivial role [73–79]. Our nonreciprocal Ising model can be seen as a stripped down version of these situations. In realistic cases, (i) there may be more than two populations (ii) the spins may take more than two possible states and (iii) the network topology may be more complex than \mathbb{Z}^d (see *e.g.* Refs. [80, 81]). While these differences are likely to induce additional complexities and phenomena, we expect that the basic features of the nonreciprocal Ising model will

persist for systems in the same universality class [23, 74]. In particular, we expect that locally-coupled many-body systems undergoing a Hopf bifurcation in mean-field will enter this universality class even if they are not originally composed of coupled spin-like degrees of freedom.

B. Phase transitions to time-dependent states

An underlying motivation for this work is to construct a bridge between bifurcations in non-variational systems and phase transitions out of equilibrium. In the equilibrium Ising model, for instance, the ferromagnet/paramagnet transition corresponds to a pitchfork bifurcation in mean-field. This means that the scalar order parameter ϕ (*e.g.* the magnetization) follows the dynamics $(d/dt)\phi = \alpha\phi - \phi^3$ in which $\alpha \propto T - T_c$ is proportional to the distance from the critical temperature. Conversely, the thermal field theory corresponding to locally-coupled pitchfork bifurcations where

$$\partial_t \phi = \alpha\phi - \phi^3 + D\Delta\phi + \eta(t, r), \quad (1)$$

in which η is a thermal noise, leads upon renormalization to the Ising critical point [27]. This dynamics can be seen as the model A dynamics (in the formalism of Hohenberg and Halperin [82]) associated to a ϕ^4 free energy \mathcal{F} , namely

$$\Gamma \partial_t \phi = -\frac{\delta \mathcal{F}}{\delta \phi} \quad (2)$$

where Γ is a kinetic coefficient.

In nonreciprocal and other non-equilibrium systems, the dynamics of the (not necessarily scalar) order parameter $\vec{\phi}$ is typically non-variational,

$$\Gamma \partial_t \vec{\phi} = \vec{f}[\vec{\phi}] \neq -\frac{\delta \mathcal{F}}{\delta \vec{\phi}} \quad (3)$$

so bifurcations with no analogue at equilibrium can occur, in particular those leading to limit cycles. The simplest instance is the Hopf bifurcation, which describes the appearance of a limit cycle from a fixed point, see Refs. [83, 84]. Unless otherwise specified, “fixed points” in this paper refer to fixed points of the physical dynamics, not fixed points of a renormalization group (RG) flow. The Hopf bifurcation describes a variety of spatially extended systems [85] ranging from oscillatory chemical reactions and extended lasers [86] to models of mammalian hearing [87, 88]. This bifurcation is described by the equation

$$\dot{z} = (\alpha + i\omega)z - |z|^2 z \quad (4)$$

for the complex numbers z and takes place at $\alpha = 0$. When z is replaced by a complex field ψ with appropriate diffusive couplings, the corresponding equation is known as the complex Ginzburg-Landau equation [86].

The fate of this bifurcation has been analyzed using perturbative RG in Refs. [89, 90], and later reproduced and generalized in Refs. [91, 92]. In these works, a phase transition generalizing the Hopf bifurcation is predicted based on a $d = 4 - \epsilon$ expansion and formally related to the RG fixed point of model A dynamics with $O(2)$ symmetry (i.e., to the XY universality class). Using this analogy Refs. [89, 90] predict that this phase transition, which leads to an oscillating phase with long-range order, should exist for space dimension $d > 2$, while no coherent oscillations are expected in $d < 2$, and quasi-long-range order is conjectured in $d = 2$ [93]. To the best of our knowledge, these predictions have only been tested qualitatively, in Refs. [94, 95], where numerical simulations of coupled three-state oscillators were performed for lattices of size L^d going up to $L = 80$ in $d = 3$. A comparison of the rescaled finite-size scaling data of Refs. [94, 95] with Ising and XY exponents suggested a better collapse with XY exponents. The results of our large-scale simulations with lattices of sizes up to $L = 320$ in $d = 3$ are in agreement with the predictions of Refs. [89, 90] and with the qualitative observations of Refs. [94, 95]. In particular, we obtain values of the critical exponents that are in very good agreement with XY exponents but not with Ising exponents.

The Hopf bifurcation is not the only way to produce a limit cycle. Another relevant bifurcation is the infinite-period bifurcation (or SNIC bifurcation) that describes the creation of a limit cycle by a saddle-node bifurcation that connects heteroclinic orbits together [83]. Here, multiple SNIC bifurcations (related by symmetry) arise at the same time in the mean-field transition from a static ordered (symmetry-breaking) state to a limit cycle. To the best of our knowledge, the field-theoretical version of this class of bifurcations has not been studied. It has been conjectured that it does not exist in spatially extended systems of arbitrary dimension in Ref. [96] based on the instability of the static ordered state in the three-state oscillator model of Refs. [94, 95]. Our simulations suggest that a static ordered state can exist despite the presence of nonreciprocal coupling (provided that they are not fully anti-symmetric, at least in our model), but even in this case we did not find evidence of any direct transition between the static-order and oscillating phases.

C. Stability of spatially coherent oscillations

Our work is also directly related to the question of the stability and spatial coherence of time-periodic phases in noisy locally-coupled classical many-body systems. By considering the nucleation and growth of droplets from fluctuations, Ref. [97–100] argued that spatially coherent oscillations are unstable in the thermodynamic limit if they arise from the spontaneous breaking of a discrete time-translation invariance (in particular when the period of oscillation is commensurate with the discrete

time unit characterizing the evolution) [101]. This is not the case in our model, where the oscillating phase arises from the spontaneous breaking of a continuous time-translation invariance (and the period is generically incommensurate with the discrete time unit). The case of spontaneously broken continuous time-translation invariance is considered in Refs. [99, 100, 102] using a mapping between the desynchronization of local oscillators and the roughening of surfaces described by the Kardar-Parisi-Zhang (KPZ) equation [103]. In the KPZ universality class, surfaces are always rough in $d \leq 2$, while two phases (rough or smooth) are possible for $d > 2$, see *e.g.* § 5.7.4 of Ref. [104]. Based on this mapping, it is argued that temporal order can exist in $d > 2$ but not in $d \leq 2$ in isotropic systems. Note that in the mapping to the KPZ equation, the angular nature of phase variables (defined on a compact space) is neglected, which amounts to ignoring topological defects, expected not to affect the large-scale physics [102]. A compact version of the KPZ equation has been studied in Refs. [105–108], but not in isotropic systems in $d = 3$. Similarly, Refs. [91, 109] suggested an analogy with the Mermin-Wagner theorem [82, 110] in the time domain, according to which the fluctuations of the Goldstone modes associated with broken time-translation invariance destroy order in $d \leq 2$.

References [111–118] performed numerical simulations of cellular automata and coupled map lattices (see Ref. [112] for an introduction) in various space dimensions, from which it emerged that periodic oscillations are possible for $d \geq 3$ within this class of systems [113, 119, 120]. Similar behaviors were reported in simulations of predator-prey models on lattice [23, 27, 121–126]. These results are in agreement with the theoretical arguments reviewed above, and are also consistent with our numerical observations. Similar questions arise in the study of the synchronization of locally coupled oscillators with randomly distributed frequencies (like in the Kuramoto model), see § IV.A of Ref. [127] and references therein, but the physics is different because of the random frequencies.

D. Classical continuous time crystals

The works reviewed in the previous paragraphs are primarily concerned with the *spatial* coherence of the oscillations. In a nutshell, they ask whether there can be macroscopic quantities averaged over the entire system (such as the magnetization; we call these order parameters) that oscillate forever. When this is the case, we can ask another question: is the oscillation of the macroscopic order parameter temporally coherent? In other words, is it acting as a good clock? Addressing this question is another of the key motivations of our work. To illustrate the difference, let us consider a simple noisy phase oscillator

$$\dot{\phi} = \omega + \sqrt{2D_\phi}\eta(t) \quad (5)$$

where $\eta(t)$ is a white noise with $\langle \eta \rangle = 0$ and $\langle \eta(t)\eta(t') \rangle = \delta(t - t')$. Here, ϕ can be seen as the argument of a complex number $z(t) = Ae^{i\phi(t)}$ whose amplitude A is very quickly relaxing to its steady-state value. In this simple system, we observe that the average value $\langle \phi \rangle$ always oscillates (averaging the equation of motion leads to $\langle \phi(t) \rangle = \phi(0) + \omega t$). However, this oscillator only keeps track of time (*i.e.* of its initial phase) for so long. To see that, consider the correlation function $C(t) = \langle e^{i[\phi(t) - \phi(0)]} \rangle$ which describes the average phase that an assembly of independent clocks would have at time t , provided that they were synchronized at time $t = 0$. Here, it behaves as [128]

$$C(t) \propto \cos(\omega t)e^{-t/\tau} \quad (6)$$

where $\tau = 1/D_\phi$, meaning that the oscillator loses track of its original phase after $\mathcal{Q} = \omega\tau$ oscillations (\mathcal{Q} is known as the quality factor of the noisy oscillator). In fact, any noisy oscillator behaves in this way at long times [129].

Thermodynamic bounds on the number \mathcal{Q} of coherent oscillations have been considered [130–133], and suggest that an infinite amount of energy (more precisely of entropy production) is needed to obtain infinite coherence. It is however not excluded that a macroscopic system in the thermodynamic limit can have an infinite coherence time with a finite cost per unit volume. Our numerical results suggest that this indeed happens in our model: we evaluate the coherence time of oscillations, which scales as $\tau(L) \sim L^3$ (in $d = 3$). This points to the existence of perfectly coherent oscillations in the thermodynamic limit. Additionally, we measure the entropy production rate per unit volume and find that it converges to a finite value, independent of system size. In this sense, our model can be seen as a classical continuous time crystal [134–147]. We conjecture that this property may extend to other systems with locally coupled oscillators that spontaneously break a continuous time-translation symmetry.

III. OUTLINE AND SUMMARY

The outline of the paper is as follows: we present the nonreciprocal Ising model with general asymmetric coupling between the two species and derive its mean-field equation in Sec. IV. In Secs. V and VII–XI we restrict ourselves to the fully anti-symmetric case in which the system exhibits C_4 symmetry. In Sec. IV we show that the mean-field equation predicts three distinct phases: disorder, time-dependent order that we dub “swap”, and static order, and analyze the bifurcations that separate the phases. Details on the Monte-Carlo simulations are given in Sec. VI. Our numerical simulations in 2D are presented in Sec. VII, suggesting that the swap phase is unstable in 2D due to spiral defects. In Sec. VIII we show that the swap phase is stable in 3D, and calculate the static critical exponents of the phase transition from disorder to swap. These critical exponents are in excellent

agreement with the equilibrium XY critical exponents, which is compatible with renormalization-group studies and with the breaking of a continuous time-translation symmetry. We calculate the coherence time of the magnetization and show that it grows with system size, suggesting a time-crystal behavior in the thermodynamic limit. In Sec. IX, we provide numerical evidence and theoretical arguments that suggest that the static-order phase is destroyed in any finite dimension due to droplet growth. In Sec. X we discuss how the system coarsens into swap and static-order states. The phase diagram of the fully anti-symmetric case is summarized in Sec. XI. In Sec. XII we allow the presence of inter-species reciprocal couplings, which reduces the symmetry to \mathbb{Z}_2 , and accounts for a general asymmetric interaction. We present mean-field analysis and 2D and 3D simulation results. These results reveal that the swap phase stability is unchanged with respect to the fully anti-symmetric case (*i.e.* it is stable in 3D but not in 2D). However, static order can be restored by an intriguing droplet-capture mechanism. Contrary to the mean-field prediction, we find no evidence of a direct transition between the swap and the static-order phase. We summarize our results and conclusions in Sec. XIII.

IV. THE MODEL

In the equilibrium Ising model, adjacent on-lattice spins ($\sigma = \pm 1$) stochastically align with one another through an energy function. Its dynamics is given by kinetic Ising models which, while lacking uniqueness, always operate by minimizing the global free energy. In what follows, we generalize these kinetic Ising models to the case of nonreciprocal interactions where such global potential function does not exist. To this aim, we define a Glauber dynamics [148] where each spin tends to minimize its own *selfish energy*. Similar formulations were used among the physical sciences [6, 20, 35, 52, 65, 149–154].

A. The nonreciprocal (NR) Ising model

We consider two spin species, labeled by Greek indices $\alpha = A, B$, located on a d -dimensional cubic lattice of linear size L . Each site $i \in \{1, \dots, L^d\}$ contains one A-spin and one B-spin (Fig. 1, left). The state of the system is described by a vector

$$\vec{\sigma} = \{\sigma_1^A, \dots, \sigma_{L^d}^A, \sigma_1^B, \dots, \sigma_{L^d}^B\} \quad (7)$$

in which each spin $\sigma_i^\alpha = \pm 1$.

We consider transition rates given by the generalized Glauber dynamics [148] in which the transition rate $w(\vec{\sigma}|\vec{\sigma}')$ from configuration $\vec{\sigma}$ to $\vec{\sigma}'$ is given by

$$w(F_i^\alpha \vec{\sigma}|\vec{\sigma}) = \frac{1}{2\tau} \left[1 - \tanh \left(\frac{\Delta E_i^\alpha}{2k_B T} \right) \right] \quad (8)$$

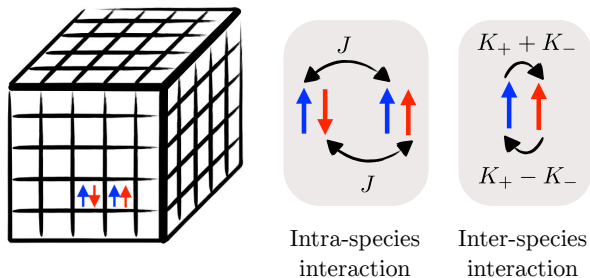


Fig. 1. Nonreciprocal (NR) Ising model. The model includes two species per site with two interaction types: (i) reciprocal nearest-neighbors interaction of strength J between same-species spins and (ii) nonreciprocal same-site interaction of strength $K_+ + K_-$ for species A (blue) and $K_+ - K_-$ for species B (red), between spins of different species.

where T is the temperature, k_B the Boltzmann constant, and τ is a characteristic time for single spin flips. In addition,

$$\Delta E_i^\alpha = E_i^\alpha(F_i^\alpha \vec{\sigma}) - E_i^\alpha(\vec{\sigma}) \quad (9)$$

is the difference in selfish energy between the states. Here F_i^α is a single-spin-flipping operator, *i.e.*, when acting on $\vec{\sigma}$ it flips the α -species spin on site i from σ_i^α to $-\sigma_i^\alpha$ while keeping all the other spins unchanged. For instance,

$$F_i^A \{\sigma_1^A, \dots, \sigma_i^A, \dots, \sigma_{L^d}^A, \sigma_1^B, \dots, \sigma_{L^d}^B\} = \{\sigma_1^A, \dots, -\sigma_i^A, \dots, \sigma_{L^d}^A, \sigma_1^B, \dots, \sigma_{L^d}^B\} \quad (10)$$

For the selfish energy, we choose

$$E_i^\alpha = -J \sum_{j \text{ nn of } i} \sigma_i^\alpha \sigma_j^\alpha - K_{\alpha\beta} \sigma_i^\alpha \sigma_i^\beta, \quad (11)$$

where

$$K_{\alpha\beta} = \begin{pmatrix} 0 & K_+ + K_- \\ K_+ - K_- & 0 \end{pmatrix} \quad (12)$$

and $J, K_+, K_- > 0$. The sum in Eq. (11) runs over nearest neighbors of i and summation over spin indices β is implied. The selfish energy indicates that spins of the same species tend to align with their neighbors, while spins of different species interact nonreciprocally (see Fig. 1, right): spins A tend to align with spins B , whereas spins B either tend to align with spins B but to a lesser extent (if $K_+ > K_-$), or tend to anti-align with spins A (if $K_+ < K_-$). The latter case will be the main focus of this paper as it leads to a rich phenomenology related to limit cycles. Note that in our model, inter-species interactions only occur between spins located on the same site.

In the continuous-time limit, the probability $P(\vec{\sigma}, t)$ to observe a specific configuration of spins $\vec{\sigma}$ at time t

evolves according to the master equation

$$\begin{aligned} \partial_t P(\vec{\sigma}, t) = & - \sum_{i,\alpha} w(F_i^\alpha \vec{\sigma} | \vec{\sigma}) P(\vec{\sigma}, t) \\ & + \sum_{i,\alpha} w(\vec{\sigma} | F_i^\alpha \vec{\sigma}) P(F_i^\alpha \vec{\sigma}, t). \end{aligned} \quad (13)$$

As detailed in Sec. VI, we perform Monte-Carlo simulations that sample trajectories obtained from a discrete-time version of Eq. (13).

We note that the Glauber dynamics of the nonreciprocal Ising model can be written in terms of a new variable θ_i (instead of σ_i^α), which is defined as the angle on the (σ_i^A, σ_i^B) plane. This angle θ_i can take one of the four values respectively corresponding to the four possible states per site: $\pi/4$ ($\uparrow\uparrow$), $3\pi/4$ ($\downarrow\uparrow$), $5\pi/4$ ($\downarrow\downarrow$), and $7\pi/4$ ($\uparrow\downarrow$) (see Fig. 2 and an explicit mapping for the fully anti-symmetric case in Sec. V A). The color code given in Fig. 2 is used throughout the paper.

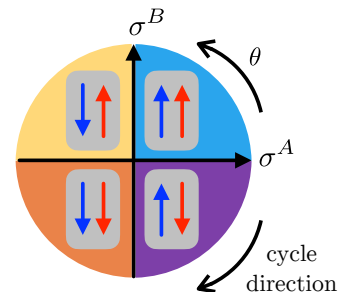


Fig. 2. Mapping between the state of two spins located on the same site (σ^A and σ^B) and their corresponding angle variable θ . The color associated to each quadrant is used throughout the paper to indicate the corresponding spin state. The direction of the cycle is determined by the sign of K_- (throughout the paper $K_- > 0$ which implies clockwise direction).

B. Broken detailed balance

We now show that the nonreciprocal Ising model described in the previous section is out of equilibrium, in the sense that it breaks detailed balance.

A Markov chain with rates w satisfies detailed balance if it has a stationary distribution P^{ss} such that

$$\frac{w(\vec{\sigma} \rightarrow \vec{\sigma}')}{w(\vec{\sigma}' \rightarrow \vec{\sigma})} = \frac{P^{\text{ss}}(\vec{\sigma}')}{P^{\text{ss}}(\vec{\sigma})}. \quad (14)$$

Let us assume that our kinetic model possesses an (unknown) stationary distribution $P^{\text{ss}}(\vec{\sigma})$. Considering a loop $\vec{\sigma}_1 \rightarrow \vec{\sigma}_2 \rightarrow \dots \rightarrow \vec{\sigma}_n$ in state space, as well as the same loop travelled in opposite direction, detailed balance implies [155]

$$\frac{w(\vec{\sigma}_1 \rightarrow \vec{\sigma}_2)}{w(\vec{\sigma}_1 \rightarrow \vec{\sigma}_n)} \cdot \frac{w(\vec{\sigma}_2 \rightarrow \vec{\sigma}_3)}{w(\vec{\sigma}_n \rightarrow \vec{\sigma}_{n-1})} \dots \frac{w(\vec{\sigma}_n \rightarrow \vec{\sigma}_1)}{w(\vec{\sigma}_2 \rightarrow \vec{\sigma}_1)} = 1. \quad (15)$$

If we find a cycle such that this ratio is not unity, then detailed balance cannot be satisfied. This is known as the Kolmogorov criterion. Here, a relevant cycle to consider consists in flipping the spins (σ_i^A, σ_i^B) of a fixed site i according to $\uparrow\uparrow \rightarrow \uparrow\downarrow \rightarrow \downarrow\downarrow \rightarrow \downarrow\uparrow \rightarrow \uparrow\uparrow$, while keeping all the other spins unchanged. Using Eqs. (8), (11) and assuming all the neighboring spins are up, we obtain

$$\begin{aligned}
w(\uparrow\uparrow \rightarrow \uparrow\downarrow) &= f(\tilde{J} + \tilde{K}_+ - \tilde{K}_-) \\
w(\uparrow\downarrow \rightarrow \downarrow\downarrow) &= f(\tilde{J} - \tilde{K}_+ - \tilde{K}_-) \\
w(\downarrow\downarrow \rightarrow \downarrow\uparrow) &= f(-\tilde{J} + \tilde{K}_+ - \tilde{K}_-) \\
w(\downarrow\uparrow \rightarrow \uparrow\uparrow) &= f(-\tilde{J} - \tilde{K}_+ - \tilde{K}_-) \\
w(\uparrow\uparrow \rightarrow \downarrow\uparrow) &= f(\tilde{J} + \tilde{K}_+ + \tilde{K}_-) \\
w(\downarrow\uparrow \rightarrow \downarrow\downarrow) &= f(\tilde{J} - \tilde{K}_+ + \tilde{K}_-) \\
w(\downarrow\downarrow \rightarrow \uparrow\downarrow) &= f(-\tilde{J} + \tilde{K}_+ + \tilde{K}_-) \\
w(\uparrow\downarrow \rightarrow \uparrow\uparrow) &= f(-\tilde{J} - \tilde{K}_+ + \tilde{K}_-)
\end{aligned} \tag{16}$$

where $f(x) \equiv (1 - \tanh(x))/(2\tau)$ and we defined the normalized coupling coefficients $\tilde{K}_- = K_-/(k_B T)$, $\tilde{K}_+ = K_+/(k_B T)$ and $\tilde{J} \equiv 2dJ/(k_B T)$. Using the identity $(1 + \tanh(x))/(1 - \tanh(x)) = e^{2x}$ we find that the forward and reverse cycles satisfy

$$\frac{w(\uparrow\uparrow \rightarrow \uparrow\downarrow) w(\uparrow\downarrow \rightarrow \downarrow\downarrow) w(\downarrow\downarrow \rightarrow \downarrow\uparrow) w(\downarrow\uparrow \rightarrow \uparrow\uparrow)}{w(\uparrow\uparrow \rightarrow \downarrow\uparrow) w(\downarrow\uparrow \rightarrow \downarrow\downarrow) w(\downarrow\downarrow \rightarrow \uparrow\downarrow) w(\uparrow\downarrow \rightarrow \uparrow\uparrow)} = e^{8\tilde{K}_-} \tag{17}$$

which means that detailed balance is broken in our model whenever $\tilde{K}_- \neq 0$. The breaking of detailed balance implies the system is driven away from equilibrium. Under certain assumptions on the physical realization of the model that go by the name of *local detailed balance* [156–158], the cycle produces entropy $\Delta S/k_B = 8\tilde{K}_-$ (see Appendix A for details). We refer to Refs. [159–163] for discussions about irreversibility and entropy production in nonequilibrium phase transitions.

C. The mean-field (MF) equation

We now derive mean-field (MF) equations of motion for the magnetizations of each species from the master equation (13) (see Refs. [164–166]). The mean-field equations are a useful guide, but it is not expected that they accurately describe the behavior of the system in any finite dimension.

The average magnetization of a single spin at time t is

$$\langle \sigma_i^\alpha(t) \rangle = \sum_{\vec{\sigma}} \sigma_i^\alpha P(\vec{\sigma}, t). \tag{18}$$

Using Eq. (13) and changing summation variables, we get

$$\frac{d}{dt} \langle \sigma_i^\alpha \rangle = -2 \langle \sigma_i^\alpha w(F_i^\alpha \vec{\sigma} | \vec{\sigma}) \rangle. \tag{19}$$

Substituting the rates (Eq. (8)) and the selfish energy (Eq. (11)) we obtain

$$\begin{aligned}
\tau \frac{d}{dt} \langle \sigma_i^\alpha \rangle &= - \langle \sigma_i^\alpha \rangle \\
&+ \left\langle \tanh \left[\frac{J}{k_B T} \sum_{j \text{ nn of } i} \sigma_j^\alpha + \frac{K_{\alpha\beta}}{k_B T} \sigma_i^\beta \right] \right\rangle
\end{aligned} \tag{20}$$

where we have used the identity $x \tanh xb = \tanh b$ for $x = \pm 1$. Applying the mean-field approximation, $\langle g(\vec{\sigma}) \rangle = g(\langle \vec{\sigma} \rangle)$ and defining the average magnetization as $\langle \sigma_i^\alpha \rangle \equiv m_i^\alpha$ yields

$$\frac{dm_i^\alpha}{dt} = -\frac{m_i^\alpha}{\tau} + \frac{1}{\tau} \tanh \left(\frac{J \sum_{j \text{ nn of } i} m_j^\alpha + K_{\alpha\beta} m_i^\beta}{k_B T} \right). \tag{21}$$

We now assume that the average magnetization changes over length scales much larger than the lattice spacing and write it as a continuum variable $m_i^\alpha = m_\alpha(\vec{r}, t)$. We thus get

$$\partial_t m_\alpha = -\frac{m_\alpha}{\tau} + \frac{1}{\tau} \tanh \left(\frac{2dJm_\alpha + K_{\alpha\beta} m_\beta + Ja^2 \nabla^2 m_\alpha}{k_B T} \right), \tag{22}$$

where a is the lattice spacing. Finally, upon rescaling time by τ and space by a we obtain

$$\partial_t m_\alpha = -m_\alpha + \tanh \left[\tilde{J} m_\alpha + \tilde{K}_{\alpha\beta} m_\beta + D \nabla^2 m_\alpha \right] \tag{23}$$

where $D \equiv J/(k_B T)$ and $\tilde{K}_{\alpha\beta} \equiv K_{\alpha\beta}/(k_B T)$. Equation (23) is the mean-field equation of the general nonreciprocal Ising model. Note that it is invariant under the diagonal up-down \mathbb{Z}_2 symmetry

$$\mathcal{S}_1 : (m_A, m_B) \mapsto (-m_A, -m_B). \tag{24}$$

V. THE FULLY ANTI-SYMMETRIC CASE

In this section as well as in Secs. VII–XI, we will study the *fully anti-symmetric case*, in which $K_+ = 0$. To simplify the notations, we write $K_- \equiv K$ (and $\tilde{K}_- \equiv \tilde{K}$). In this case, the mean-field equation reads

$$\partial_t m_\alpha = -m_\alpha + \tanh \left[\tilde{J} m_\alpha + \tilde{K} \varepsilon_{\alpha\beta} m_\beta + D \nabla^2 m_\alpha \right] \tag{25}$$

where $\varepsilon_{\alpha\beta}$ is the Levi-Civita symbol. Equation (25) has the symmetry

$$\mathcal{S}_2 : (m_A, m_B) \mapsto (-m_B, m_A) \tag{26}$$

in addition to that in Eq. (24), so overall it is invariant under the cyclic group C_4 .

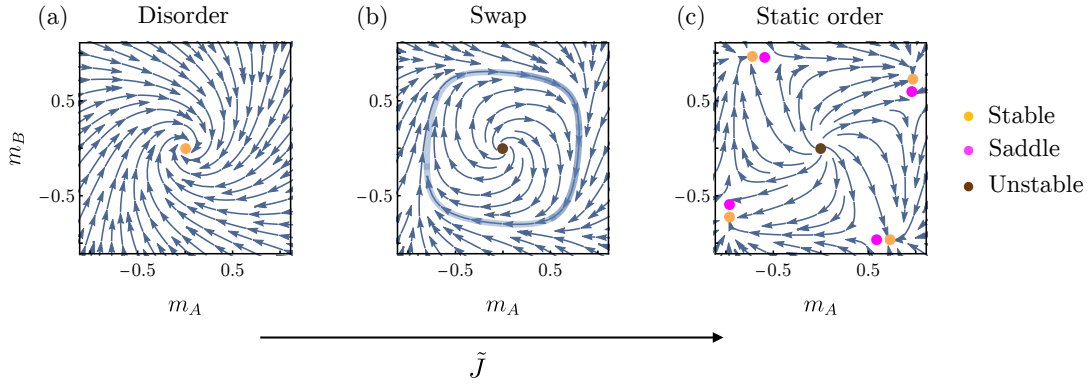


Fig. 3. Mean-field (MF) flow in (m_A, m_B) space. Arrows correspond to the vector $\vec{v} = (\partial_t m_A, \partial_t m_B)$ calculated from the spatially homogeneous full mean-field equation, Eq. (25). Fixed points are represented by dots. The limit cycle in the swap phase is highlighted by a semi-transparent blue line. Nonreciprocal inter-species coupling is $\tilde{K} = 0.4$, and reciprocal coupling between same-species nearest neighbors is (a) $\tilde{J} = 0.8$, (b), $\tilde{J} = 1.3$, and (c) $\tilde{J} = 1.8$, showing the disorder, swap, and static-order phases, respectively.

A. Connection with locally-coupled oscillators

In the fully anti-symmetric case, the dynamics of θ_i is described by the forward and backward moves,

$$\theta_i \rightarrow \theta_i + \frac{\pi}{2} \quad \text{with rate } w^+ \quad (27a)$$

$$\theta_i \rightarrow \theta_i - \frac{\pi}{2} \quad \text{with rate } w^- \quad (27b)$$

where the rates are

$$w^\pm = \frac{1}{2\tau} \left[1 - \tanh \left(\frac{\Delta E(\vec{\theta})}{2K_B T} \pm \tilde{K} \right) \right] \quad (28)$$

and

$$E(\vec{\theta}) = -2J \sum_{\langle i,j \rangle} \cos(\theta_i - \theta_j). \quad (29)$$

with the sum running over nearest-neighbor pairs. Equations (27–29) can be viewed as describing locally-coupled oscillators with internal frequency and discrete states. In this sense, they share similarities with the Wood *et al.* cyclic model [94–96] although oscillators are restricted to forward moves (backward moves are prohibited) in these references. For $K = 0$, our model reaches an equilibrium state that is equivalent to the clock model (vector Potts model) for $q = 4$ [167, 168].

B. Analysis of the bifurcations

In the $m_\alpha \ll 1$ limit and for small gradients, the mean-field equation in the fully anti-symmetric case (Eq. (25)) can be approximated by

$$\begin{aligned} \partial_t m_\alpha = & -(1 - \tilde{J})m_\alpha + \tilde{K}\varepsilon_{\alpha\beta}m_\beta + D\nabla^2 m_\alpha \\ & - \frac{1}{3} \left(\tilde{J}m_\alpha + \tilde{K}\varepsilon_{\alpha\beta}m_\beta \right)^3. \end{aligned} \quad (30)$$

For $\tilde{K} = 0$, Eq. (30) reduces to two uncoupled mean-field equations that derive from a ϕ^4 Ginzburg-Landau potential. For any $\tilde{K} \neq 0$, Eq. (30) does not derive from a potential, and describes a non-equilibrium system. Note that due to the lack of rotational symmetry in the cubic term, Eq. (30) differs from the Complex Ginzburg-Landau (CGL) equation [86, 169], which is given by

$$\partial_t \psi = a\psi + b\nabla^2 \psi + c|\psi|^2 \psi \quad (31)$$

where $\psi(\vec{r}, t)$ is a complex field and a , b and c are complex numbers. However, Eq. (30) becomes CGL-like in limits discussed below.

Here, we restrict our analysis to spatially homogeneous solutions, $m_\alpha(\vec{r}, t) \equiv m_\alpha(t)$. The linear stability of such solutions to Eq. (30) is unaffected by the Laplacian term, and we therefore analyze the spatially homogeneous mean-field equation given by

$$\begin{aligned} \partial_t m_\alpha = & -(1 - \tilde{J})m_\alpha + \tilde{K}\varepsilon_{\alpha\beta}m_\beta \\ & - \frac{1}{3} \left(\tilde{J}m_\alpha + \tilde{K}\varepsilon_{\alpha\beta}m_\beta \right)^3. \end{aligned} \quad (32)$$

Figure 3 shows the phase-space velocity field $\vec{v} = (\partial_t m_A, \partial_t m_B)$ from the spatially homogeneous full mean-field equation, Eq. (25) along with the fixed points which are obtained by numerically solving the $\partial_t m_A = \partial_t m_B = 0$ equations. The stability of the fixed points (shown in the figure as orange, pink, and brown for stable, saddle, and unstable, respectively) is determined by analyzing the eigenvalues of the Jacobian matrix \mathcal{J} of the linearized equation $\partial_t \delta \vec{m} = \mathcal{J} \delta \vec{m}$ where linearization is performed around each fixed point.

Three distinct phases are found: a disordered phase in which $m_A = m_B = 0$ is the only stable fixed point (Fig. 3a), a limit-cycle phase that we dub “swap phase” as both species repeatedly flip their magnetizations (Fig. 3b), and a static-order (ferromagnetic) phase in which, depending on initial conditions, the system ends

up in one out of four stable fixed points with non-zero m_A and m_B (Fig. 3c).

The mean-field phase diagram obtained from the spatially homogeneous full mean-field equation is shown in Fig. 4, as a function of the couplings \tilde{J} and \tilde{K} . The phases are determined by the fixed points and their stability as described above. When nonreciprocal interactions are turned off ($\tilde{K} = 0$), a pitchfork bifurcation at $\tilde{J} = 1$ (red point in Fig. 4) separates the disordered phase (in blue) from the static-order phase (in green), as in the usual Ising model. When nonreciprocal interactions are present ($\tilde{K} \neq 0$), the swap phase arises (in pink) and is separated from the disordered state by a Hopf bifurcation at $\tilde{J} = 1$ (green line), and from the static-order phase by another bifurcation known as a (C_4 -symmetric) saddle-node on an invariant circle (SNIC) bifurcation [64, 83] (blue line). We analyze each of these bifurcations below using Eq. (32).

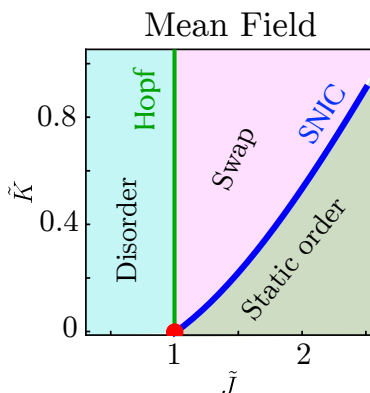


Fig. 4. Mean-field phase diagram. The three phases shown on the diagram are (i) disorder, (ii) swap and (iii) static order. The lines separating the phases are Hopf bifurcation (thin green) and SNIC bifurcation (thick blue). Red dot is the Pitchfork bifurcation. Obtained from numerical analysis of the spatially homogeneous Eq. (25).

1. Pitchfork bifurcation

For $\tilde{K} = 0$, Eq. (32) leads to the standard pitchfork bifurcation at $\tilde{J} = 1$. The $m_A = m_B = 0$ point becomes unstable and four stable fixed points

$$m_A = \pm m_B = \pm \sqrt{\frac{3(\tilde{J} - 1)}{\tilde{J}^3}} \quad (33)$$

emerge, corresponding to the ordered phase.

2. Hopf bifurcation

For $\tilde{K} \neq 0$, the eigenvalues of \mathcal{J} at $m_A = m_B = 0$ are complex,

$$\lambda_{1,2} = -1 + \tilde{J} \pm i\tilde{K}. \quad (34)$$

This means that there is a Hopf bifurcation at $\tilde{J} = 1$: the $m_A = m_B = 0$ point become unstable for $\tilde{J} > 1$ and a stable limit cycle emerges, corresponding to the swap phase.

The limit cycle is more easily analyzed in polar coordinates, $m_A = r \cos \theta$ and $m_B = r \sin \theta$ where Eq. (32) becomes

$$\begin{aligned} \partial_t r = & (\tilde{J} - 1)r - \frac{1}{4}\tilde{J}^3 \left[1 + \kappa^2 \right. \\ & \left. + \left(\frac{1}{3} - \kappa^2 \right) \cos(4\theta) + \left(\kappa - \frac{1}{3}\kappa^3 \right) \sin(4\theta) \right] r^3 \end{aligned} \quad (35)$$

$$\begin{aligned} \partial_t \theta = & -\tilde{K} + \frac{1}{4}\tilde{J}^3 \left[\kappa + \kappa^3 \right. \\ & \left. - \left(\kappa - \frac{\kappa^3}{3} \right) \cos(4\theta) + \left(\frac{1}{3} - \kappa^2 \right) \sin(4\theta) \right] r^2, \end{aligned} \quad (36)$$

with $\kappa \equiv \tilde{K}/\tilde{J}$.

The limit cycle describes anharmonic oscillations, where both r and $\dot{\theta}$ vary with θ . Its shape has a rotational symmetry of order 4 due to the C_4 symmetry of the mean-field equation. However, very close to the bifurcation, *i.e.* $\tilde{J} - 1 \ll 1$ and any fixed \tilde{K} , the oscillations are harmonic [85]. This can be seen as follows.

The equation for θ in the $\tilde{J} - 1 \ll 1$ limit is

$$\partial_t \theta = -\tilde{K} + \mathcal{O}(\tilde{J} - 1), \quad (37)$$

where we used the fact that $r^2 \sim \tilde{J} - 1$. The angle θ then has the solution $\theta = \theta_0 - \tilde{K}t$, and the equation for r becomes

$$\begin{aligned} \partial_t r = & (\tilde{J} - 1)r - \frac{1}{4} \left[1 + \tilde{K}^2 + \left(\frac{1}{3} - \tilde{K}^2 \right) \cos(4\tilde{K}t) \right. \\ & \left. - \left(\tilde{K} - \frac{1}{3}\tilde{K}^3 \right) \sin(4\tilde{K}t) \right] r^3 + \mathcal{O}((\tilde{J} - 1)^{5/2}) \end{aligned} \quad (38)$$

where we have set θ_0 to zero. Equation (38) can be solved analytically. In steady state ($t \rightarrow \infty$ limit), its solution reads

$$r(t) = 2\sqrt{\frac{\tilde{J} - 1}{1 + \tilde{K}^2}} \times \frac{1}{\sqrt{1 - (\tilde{J} - 1)f(\tilde{J}, \tilde{K}, t)}} \quad (39)$$

with

$$f(\tilde{J}, \tilde{K}, t) = \frac{1 - \tilde{J} + 3(\tilde{J} - 3)\tilde{K}^2 + 2\tilde{K}^4}{3(1 + \tilde{K}^2) \left[(\tilde{J} - 1)^2 + 4\tilde{K}^2 \right]} \cos(4\tilde{K}t) - \frac{\tilde{K} \left(5 - 3\tilde{J} + (\tilde{J} - 7)\tilde{K}^2 \right)}{3(1 + \tilde{K}^2) \left[(\tilde{J} - 1)^2 + 4\tilde{K}^2 \right]} \sin(4\tilde{K}t) \quad (40)$$

Taking the limit $\tilde{J} - 1 \ll 1$ once more ($\tilde{J} - 1$) $f(\tilde{J}, \tilde{K}, t)$ goes to zero and we arrive at

$$r(t) = 2\sqrt{\frac{\tilde{J} - 1}{1 + \tilde{K}^2}} \quad (41)$$

which is a circular motion of constant angular velocity in phase space. This harmonic solution can be rationalized by looking at the two times scales corresponding respectively to the angular and radial motion near the bifurcation (described by Eqs. (37) and (38), respectively). The angular motion time scale is $T_\theta \sim \tilde{K}^{-1}$ while the radial motion time scale is determined by the relaxation time of $r(t)$ to its new minimum when θ changes, which scales as $T_r \sim (\tilde{J} - 1)^{-1}$. The two time scales T_θ and T_r can be interpreted as “oscillation time-scale” and “alignment time-scale”, respectively. Since $T_r \gg T_\theta$, the angular motion occurs much more rapidly, leaving insufficient time for r to reach a new minimum when θ changes. Thus, only the θ -averaged value of the right-hand side of Eq. (35) matters. This is supported by Fig. 5 which shows typical phase-space trajectories in the swap phase: as $\tilde{J} - 1$ increases, the motion indeed loses its rotational symmetry and become more “square-like”.

The above result is a consequence of a more general theorem. A reaction-diffusion equation that undergoes a Hopf bifurcation such as the mean-field evolution Eq. (30) can be reduced, close to the bifurcation, to the CGL equation (*i.e.*, the CGL equation is its normal form). The transformation to the CGL equation guarantees that the steady-state solution of the non-transformed set of equations is an elliptical limit cycle (or in special cases like here, circular) [85]. Because of this reduction, we expect the disorder-to-swap phase transition in our model to be in the same universality class as the Hopf bifurcation in the CGL equation, which has been studied in Refs. [89, 90].

3. Infinite-period (SNIC) bifurcation

Let us now start from the limit-cycle swap phase. Upon increasing \tilde{J} or decreasing \tilde{K} , the system goes through a (C_4 -symmetric) saddle-node on an invariant circle (SNIC) bifurcation, where four pairs of stable and saddle fixed points emerge from the limit cycle (pink and orange points in Fig. 3c). The SNIC bifurcation is also

known under several other names: infinite-period bifurcation (because the period of oscillation diverges at the bifurcation point), saddle-node on a limit cycle (SNLC), saddle-node infinite-period (SNIPER), etc. As the dynamics is invariant under the action of the group C_4 (see Sec. V), four copies of the SNIC bifurcation happen at the same time. Bifurcations in such a dynamical system with symmetries are known as equivariant bifurcations, see Refs. [170–172] for an introduction. Once the stable fixed points emerge, the system is in a static-order phase.

Noticing that the SNIC bifurcation occurs when \tilde{K} and $\tilde{J} - 1$ are comparable (see Fig. 4), we now take the limit $\epsilon \rightarrow 0$ with $\tilde{J} - 1 \sim \epsilon$ and $\tilde{K} \sim \epsilon$. At first order in ϵ , Eqs. (35–36) become

$$\partial_t r = (\tilde{J} - 1)r - \frac{1}{4} \left(1 + \frac{1}{3} \cos(4\theta) \right) r^3, \quad (42a)$$

$$\partial_t \theta = -\tilde{K} + \frac{1}{12} \sin(4\theta)r^2. \quad (42b)$$

In a static-order state, $\partial_t r = \partial_t \theta = 0$, with r given by

$$r = 2\sqrt{\frac{\tilde{J} - 1}{1 + \frac{1}{3} \cos(4\theta)}}. \quad (43)$$

The equation for θ then becomes

$$\partial_t \theta = -\tilde{K} + \frac{\sin(4\theta)}{3 + \cos(4\theta)} (\tilde{J} - 1). \quad (44)$$

Since $\sin(4\theta)/(3 + \cos(4\theta))$ is bounded between $-1/(2\sqrt{2})$ and $1/(2\sqrt{2})$, a stationary state (with $\partial_t \theta = 0$) can only exist if $\tilde{K} < (\tilde{J} - 1)/(2\sqrt{2})$. Therefore, in the $\tilde{J} - 1 \ll 1$ regime, the SNIC bifurcation line corresponds to

$$\tilde{K} = \frac{\tilde{J} - 1}{2\sqrt{2}}. \quad (45)$$

Note that, in Fig. 4, the thick blue line corresponding to the SNIC bifurcation was obtained numerically for the full mean-field dynamics Eq. (25). Equation (45) only predicts the tangent of this thick blue line close to the pitchfork bifurcation point ($\tilde{J} = 1$, $\tilde{K} = 0$).

Finally, the fixed points emerging at the SNIC bifurcation are obtained from the θ values that maximize $\sin(4\theta)/(3 + \cos(4\theta))$, which are

$$\theta_n = \left[-\tan^{-1} \left(2\sqrt{2} \right) + \pi(2n + 1) \right] / 4 \quad (46)$$

with $n = 0, 1, 2, 3$. Together with their corresponding r values derived from Eq. (43) we obtain

$$(m_A, m_B) = 3\sqrt{\frac{\tilde{J} - 1}{2}} (\cos(\theta_n), \sin(\theta_n)). \quad (47)$$

Approaching the SNIC bifurcation from the side of the limit cycle (swap phase), $\partial_t \theta$ approaches zero when the system passes at $\theta = \theta_n$. As a result, the oscillation period diverges at the bifurcation (see Fig. 5d-f, where the period increases as we approach the bifurcation). This stands in contrast with the Hopf bifurcation in which the oscillation period remains finite.

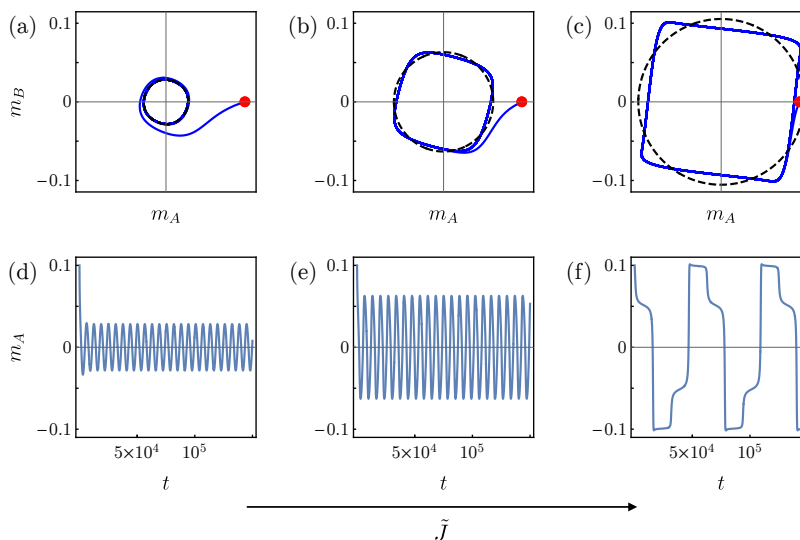


Fig. 5. Mean-field swap phase at different distances from the Hopf and SNIC bifurcations. Numerical solutions of the spatially homogeneous mean-field dynamics, Eq. (32). (a-c) m_B vs. m_A . (d-f) m_A vs. t . From left to right: $\tilde{J} = 1.0002$, 1.001, and 1.0028. In all plots $\tilde{K} = 0.001$. Red dot is the initial state and dashed black line is the steady state predicted from Eq. (41), valid near the Hopf bifurcation.

VI. MONTE-CARLO SIMULATIONS

To go beyond the mean-field description, we perform large-scale Monte-Carlo simulations of the nonreciprocal Ising model in both two and three dimensions (results in one dimension are summarized in Appendix B).

In our 2D discrete-time Monte-Carlo (MC) simulations, we use the standard Glauber algorithm: at each MC step a spin σ_i^α is chosen at random and then flipped with probability

$$p_i^\alpha = \tau w(F_i^\alpha \vec{\sigma} | \vec{\sigma}) \quad (48)$$

(with w defined in Eq. (8)).

Since three-dimensional simulations are much more costly, in 3D we update spins using a checkerboard algorithm to implement Eq. (48) instead of random picking. In the checkerboard algorithm non-interacting spins are flipped in parallel [173]. To generalize the checkerboard approach to the two-species case, we defined the quantity $\mathcal{P} = x_1 + x_2 + x_3 + \alpha$ where x_n is the integer position in the n -th dimension of the cubic lattice, and $\alpha = 0, 1$ labels the two species. Spins with the same parity of \mathcal{P} (even or odd) are then updated simultaneously. This allows us both to parallelize the simulation and avoid random number generation in choosing the spins. We did not observe qualitative changes when changing the update rules from random picking to paralleled checkerboard, as well as when using other update rules, see Appendix C.

Unless mentioned otherwise, we initialize the system in an ordered state where all spins of the same species are either up or down, and let the system evolve until a steady state is reached. Averages are then calculated in the steady state, excluding the initial transient. Time is

measured in simulation sweeps, where a single sweep is defined as $2 \times L^d$ (the number of spins) MC steps (individual attempted flips). To best visualize phenomena of interest, simulation snapshots are presented either with the spin variables σ^A and σ^B , or with the angle variable θ .

Transitions from disorder to time-dependent order and from time-dependent order to stationary order can be quantified by two order parameters. First, the synchronization order parameter

$$R \equiv \langle s \rangle_{t,\Omega} \quad \text{with} \quad s \equiv \sqrt{\frac{M_A^2 + M_B^2}{2}} \quad (49)$$

quantifies how much spins are aligned with each other within each species. Here, $M_\alpha = \sum_i \sigma_i^\alpha / L^d$ are the total magnetizations and the average $\langle \dots \rangle_{t,\Omega}$ is over time (t) and realizations (Ω). Note that s can also be written as

$$s = \frac{1}{L^d} \left| \sum_j e^{i\theta_j} \right|, \quad (50)$$

similarly to the order parameter quantifying the synchronization of oscillations in, for example, the Kuramoto model [127]. Second, the phase-space angular momentum

$$\begin{aligned} \mathcal{L} &\equiv \langle \ell \rangle_{t,\Omega} \quad \text{with} \quad \ell \equiv M_B \partial_t M_A - M_A \partial_t M_B \\ &= M_{B,t} M_{A,t+1} - M_{A,t} M_{B,t+1} \end{aligned} \quad (51)$$

quantifies the macroscopic time-reversal symmetry breaking. It is related to the entropy production [174], see Appendix A for details.

Mean-field behavior of the order parameters

In mean-field and for a spatially uniform state, the synchronization order parameter defined in Eq. (49) is

$$R_{\text{MF}} = \frac{\langle r \rangle_t}{\sqrt{2}} \quad (52)$$

and the phase-space angular momentum defined in Eq. (51) is

$$\mathcal{L}_{\text{MF}} = -\langle r^2 \dot{\theta} \rangle_t. \quad (53)$$

The sign is chosen so that \mathcal{L} is positive when K is positive. In Fig. 6, R_{MF} and \mathcal{L}_{MF} , calculated from a numerical steady-state solution of the spatially homogeneous Eq. (25), are plotted as a function of \tilde{J} for a fixed value of \tilde{K} . It is shown that R_{MF} goes from zero to non-zero values when crossing the Hopf bifurcation at $\tilde{J} = 1$. When crossing the SNIC bifurcation, R_{MF} remains finite, but there is a sharp change in the slope: the slope increases when approaching the bifurcation and decreases in the static order regime. Conversely, \mathcal{L}_{MF} is identically zero in both the disordered and static-order phases, but deviates from zero in the swap phase. Both R_{MF} and \mathcal{L}_{MF} are continuous at the bifurcation points, as in a second-order phase transition. In the swap phase and near the Hopf bifurcation, we can use Eq. (37) and Eq. (41) to obtain

$$R_{\text{MF}} = \sqrt{\frac{2(\tilde{J} - 1)}{1 + \tilde{K}^2}} \quad \text{and} \quad \mathcal{L}_{\text{MF}} = \frac{4\tilde{K}(\tilde{J} - 1)}{1 + \tilde{K}^2}. \quad (54)$$

In the swap phase and near the SNIC bifurcation, \mathcal{L}_{MF} scales with $\mu^{1/2}$ where μ is the distance from the bifurcation line (because the period scales as $T \sim \mu^{-1/2}$ while r remains finite at the bifurcation [83]). We now analyze how these mean-field results hold in finite-dimensional systems using the Monte-Carlo simulations.

VII. DESTRUCTION OF THE SWAP PHASE IN 2D BY SPIRAL DEFECTS

In small 2D systems, simulations show states in which M_A and M_B oscillate in time (like in the mean-field swap phase). These oscillations are irregular, and typically occur through nucleation of droplets of opposite magnetization by the “unsatisfied” species, in alternating order (see Movie 1).

However, as L increases these oscillations become a transient that quickly destabilizes (see Fig. 7) due to the formation and proliferation of spiral defects. Figure 8 and Movie 1 show the emergence of defects after an oscillatory transient. The defects are manifest in the θ variable and appear to have four distinct arms, ordered according to the cycle $\uparrow\uparrow \rightarrow \uparrow\downarrow \rightarrow \downarrow\downarrow \rightarrow \downarrow\uparrow$ that can be followed either clockwise (+ defects) or anti-clockwise (− defects). The 4-fold rotational symmetry in the spiral shape stems from

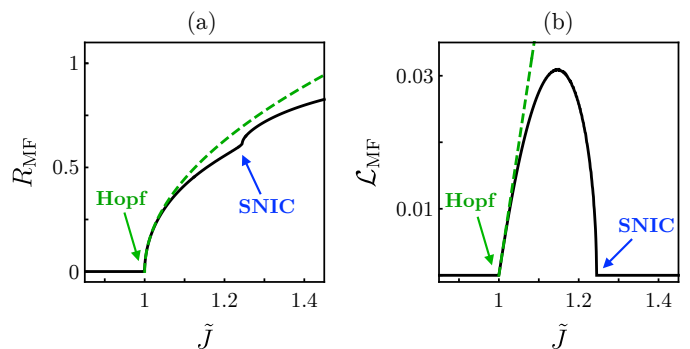


Fig. 6. Mean-field order parameters. (a) The synchronization order parameter R_{MF} (Eq. (52)) and (b) the phase-space angular momentum \mathcal{L}_{MF} (Eq. (53)), shown as a function of \tilde{J} and for fixed $\tilde{K} = 0.1$. Black lines are obtained from numerical solutions of the spatially homogeneous Eq. (25) in steady state. Dashed green lines are approximate solutions that are valid near the Hopf bifurcation, given by Eq. (54).

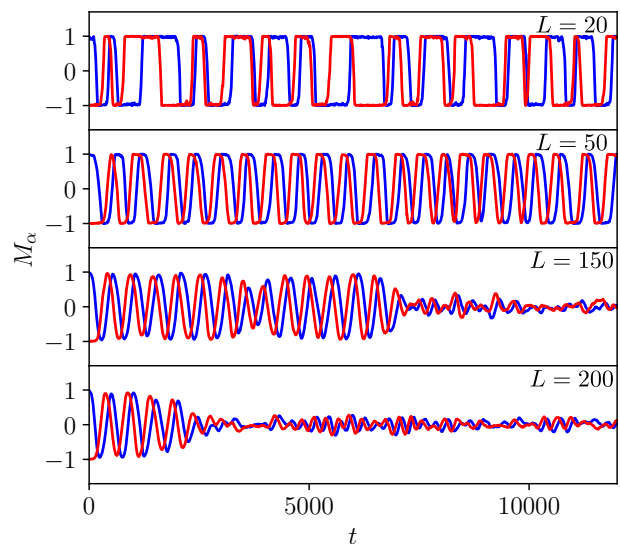


Fig. 7. Swap phase in finite 2D systems. The magnetizations M_A (blue) and M_B (red) as a function of time, for increasing system sizes (from top to bottom: $L = 20, 50, 150, 200$). Obtained from MC simulations with the parameters: $\tilde{J} = 2.8$, $\tilde{K} = 0.3$.

the C_4 symmetry of the model in the fully anti-symmetric case, and is even more visible in the mean-field equation, see Fig. 8c displaying a snapshot of a spiral obtained from integrating numerically Eq. (30) with a boundary condition that imposes a winding number. In terms of the complex order parameter $\psi = m_A + im_B$, the C_4 symmetry of the mean-field equation translates into defects satisfying $e^{-i\theta} \psi(R_\theta \vec{r}, t) = \psi(\vec{r}, t)$ for $\theta = 0, \pi/2, \pi, 3\pi/2$, where R_θ is the rotation matrix with angle θ .

Despite having 4-fold rather than full rotational symmetric shape, the spiral waves observed in the nonreciprocal Ising model appear to behave similarly to those emerging in the CGL equation [86, 102, 106, 107, 177–

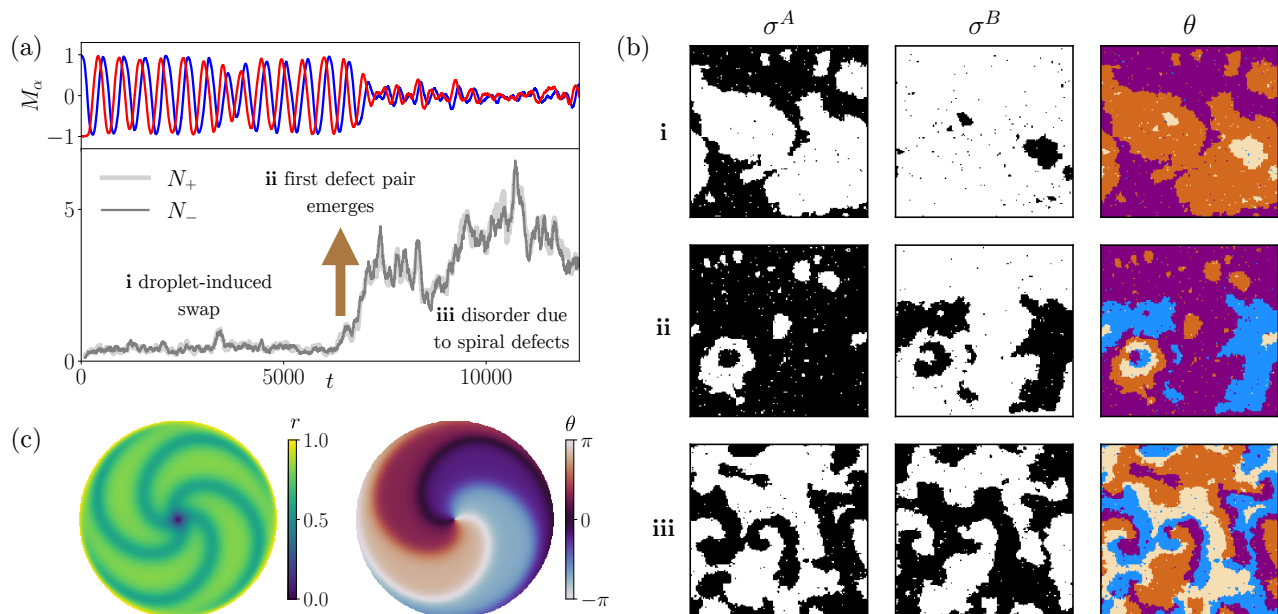


Fig. 8. Destruction of the swap phase by spiral defects in 2D. (a) Top: the magnetizations M_A (blue) and M_B (red) as a function of time (the same as in Fig. 7, third row). Bottom: the number of + and - defects N_+ and N_- averaged over 100 time steps, as a function of time. We identify defects as adjacent 2 by 2 sites with a cycle of $\uparrow\uparrow\rightarrow\uparrow\downarrow\rightarrow\downarrow\downarrow\rightarrow\downarrow\uparrow$, either clockwise (+ defects) or anti-clockwise (- defects). (b) Snapshots of σ^A , σ^B , and θ (i) before, (ii) during, and (iii) after the proliferation of spiral defects. Black and white are up and down spins, respectively, and the θ color code corresponds to Fig. 2. See Movie 1 for the full evolution. (c) Snapshot of a spiral in the mean-field equation, showing r (left) and θ (right). Note the 4-fold rotational symmetry. Panels a-b are produced from the same MC simulation, with the parameters: $\tilde{J} = 2.8$, $\tilde{K} = 0.3$, and $L = 150$. Panel c is obtained by solving numerically Eq. (30) on a disk of radius R_{sim} with boundary conditions $\psi(r = R_{\text{sim}}, \theta) = \psi_0 e^{i\theta}$ (r and θ are polar coordinates) that enforce the existence of a topological defect. We have set $\tilde{J} = 2$, $\tilde{K} = 0.6$, $D = 0.5$, $R_{\text{sim}} = 10$. Equation (30) is integrated using the pseudospectral solver Dedalus [175] on a disk domain discretized with $N_\phi = 201$ azimuthal modes and $N_r = 200$ radial modes using a 1st-order 1-stage diagonally implicit-explicit Runge-Kutta scheme (RK111 in Dedalus) [176] with a fixed time step $dt = 1 \times 10^{-2}$ for 20 simulation time units.

185]. Defects are created and annihilated in pairs and opposite topological charges (+ and - defects) lead to opposite angular velocities (see Movie 1). Finally we note that in mean-field, a homogeneously oscillating system is stable, but given sufficiently strong added noise spirals emerge, as in our Monte-Carlo simulations (see Appendix D).

Quantitatively, the absence of a swap phase in the thermodynamic limit can be seen from the behavior of the order parameters R and \mathcal{L} (Eq. (49) and (51), respectively) as system size increases. In Fig. 9a-d color maps of R and \mathcal{L} are shown as a function of \tilde{J} and \tilde{K} for small ($L = 20$) and large ($L = 80$) systems. For the $L = 20$ system, there is a region in which both R and \mathcal{L} are non-zero, compatible with the swap phase. However, for the $L = 80$ system, both R and \mathcal{L} diminish in this region, indicating instead a disorder phase. Figures 9e and 9f show the order parameters as function of \tilde{J} for fixed \tilde{K} , at different system sizes. The intermediate region ($1.5 \lesssim \tilde{J} \lesssim 3$) corresponds to the finite-system swap state, but both R and \mathcal{L} approach zero as L increases. In addition, the putative critical \tilde{J} marking the transition from disorder to swap depends on the system size, signifying the absence of a well-defined phase transition

in the thermodynamic limit.

To conclude, our numerical simulations indicate that the mean-field swap phase is destroyed by spiral defects in 2D where it is replaced by a disordered state.

VIII. EXISTENCE OF A STABLE SWAP PHASE IN 3D

In 3D, numerical simulations suggest that a stable swap phase does exist. Its behavior is demonstrated in Fig. 10 where we show a kymograph of the θ -field of a single 1D row in the 3D lattice as well as a plot of the total magnetizations and s (Eq. (49)) as a function of time. A full visualization of this phase is shown in Movie 2. Unlike the 2D droplet-induced swap persisting at finite systems (Movie 1), here the oscillations are noisy and spatially homogeneous, without any apparent structures. Moreover, $M_A(t)$ and $M_B(t)$ display coherent oscillations with a fixed period and phase shift between the species.

Simulations with varying system sizes indicate there is a well-defined phase transition between a disordered phase with $R = \mathcal{L} = 0$ to a swap phase with non-zero R and \mathcal{L} . Figure 11 shows color maps of R and \mathcal{L} in

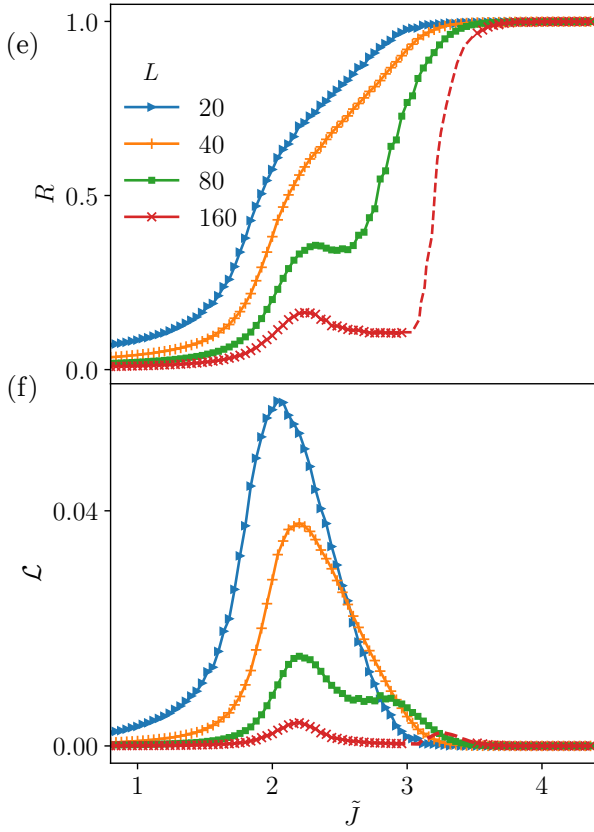
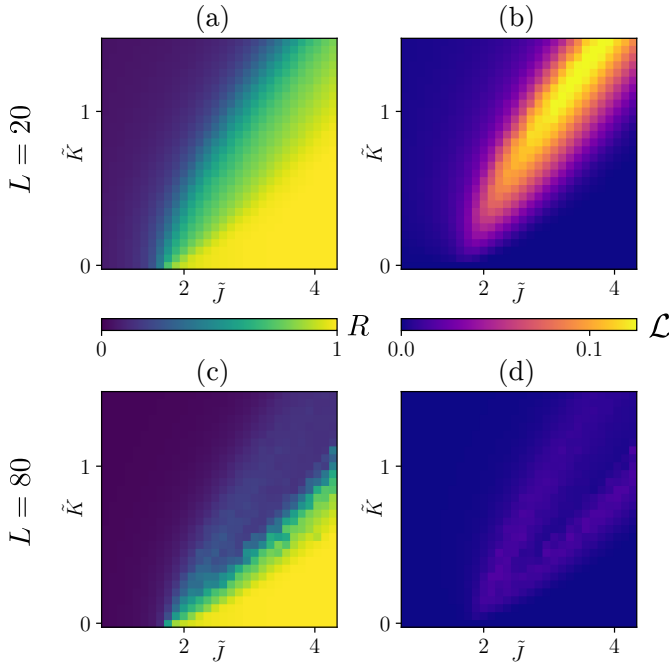


Fig. 9. Instability of the swap phase in 2D as seen by the order parameters. Color map of the (a) synchronization order parameter R and (b) phase-space angular momentum \mathcal{L} , as a function of \tilde{J} and \tilde{K} , for a 2D system with $L = 20$. (c-d) The same with $L = 80$. (e) R and (f) \mathcal{L} , shown as a function of \tilde{J} for $\tilde{K} = 0.3$, for different linear system size L . Dashed red line shows upper bound for R and \mathcal{L} for points that did not converge during simulation running time. Obtained from MC simulations.

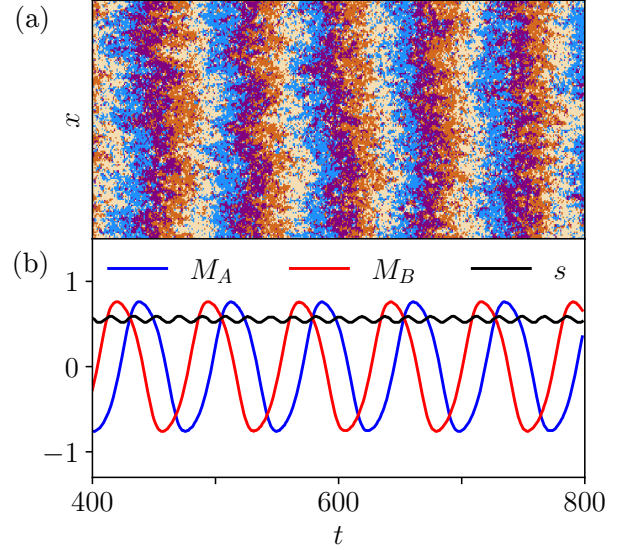


Fig. 10. Time evolution of a stable swap state in 3D. (a) Kymograph of θ for a single 1D row in the 3D system. (b) M_A , M_B and $s = \sqrt{(M_A^2 + M_B^2)}/2$ as a function of time. Obtained from MC simulation with parameters: $\tilde{J} = 1.5$, $\tilde{K} = 0.1$ and $L = 160$.

the (\tilde{K}, \tilde{J}) space, for linear system size $L = 320$, while Fig. 12a-b shows a cut of the color maps for $\tilde{K} = 0.3$ with different L values. The inset of Fig. 12a shows two different behaviors depending on whether \tilde{J} is above or below a critical value \tilde{J}_c , unlike in 2D (Fig. 9). Below \tilde{J}_c , R approaches zero with $R \sim L^{-d/2}$ scaling as L increases: this corresponds to the disordered phase. Above \tilde{J}_c , R converges to a finite non-zero value as L increases: this corresponds to an ordered phase, here the swap phase. Moreover, the phase transition appears to be second-order in the sense that R and \mathcal{L} change continuously.

The critical \tilde{J}_c separating disorder from swap is \tilde{K} dependent (see Fig. 11), in contrast with the mean-field prediction (Fig. 4). In the $\tilde{K} \rightarrow \infty$ limit, and for any \tilde{J} , the swap phase is unstable and both R and \mathcal{L} are zero. This stems from the fact that when $\tilde{K} \gg \tilde{J}$, each spin responds to the local force imposed by the other species and disregards alignment with its neighbors. As a result, each site performs rapid cycles ($\uparrow\uparrow \rightarrow \uparrow\downarrow \rightarrow \downarrow\downarrow \rightarrow \downarrow\uparrow \rightarrow \uparrow\uparrow$), but neighboring sites are not synchronized. A phase transition similar to the one in Fig. 12a-b (continuous in R and \mathcal{L}) is observed for a fixed \tilde{J} cut (see Fig. 12c in which $\tilde{J} = 1.5$). Both R and \mathcal{L} are zero at large \tilde{K} and become finite below some critical \tilde{K}_c ($\tilde{K} \approx 0.5$ in Fig. 12c).

Note that the second-order phase transition between disorder and swap is limited to small \tilde{J} and \tilde{K} values. At high values of \tilde{J} and \tilde{K} , the transition appears to be discontinuous. This is discussed further in Sec. VIII C.

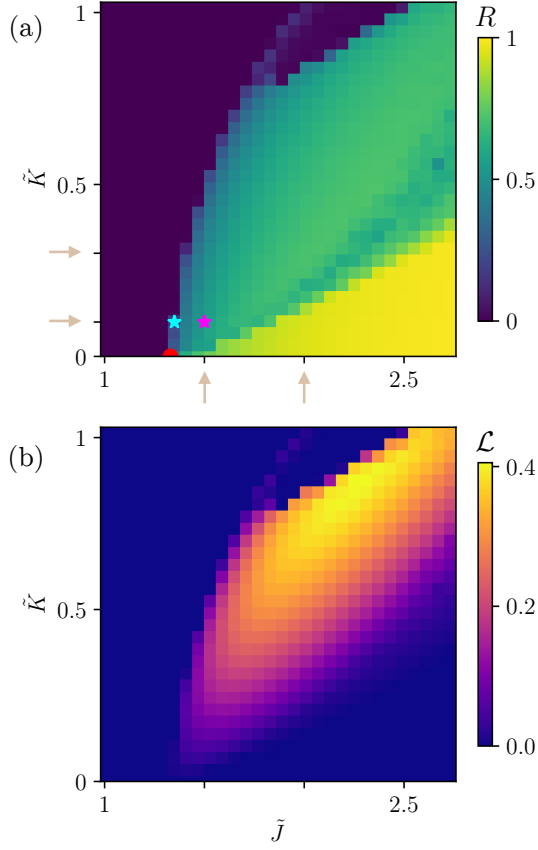


Fig. 11. Order parameters in a large 3D system. Color map of (a) R and (b) \mathcal{L} as a function of \tilde{J} and \tilde{K} for a 3D system with $L = 320$. In (a), red dot marks the 3D Ising phase-transition point ($\tilde{J}_c \approx 1.33$ and $\tilde{K} = 0$), arrows corresponds to fixed \tilde{K} and fixed \tilde{J} cuts analyzed in Figs. 12, 14 and 18 and stars depict points analyzed in Fig. 13. Obtained from MC simulations.

A. Critical exponents

Having numerically confirmed the existence of a continuous phase transition from disorder to swap in 3D, we move on to determine the related critical exponents, focusing on the order parameter $R = \langle s \rangle$ (averages here and in the following discussion are with respect to time and realizations but for brevity, we remove the t and Ω subscripts). Note that \mathcal{L} is not expected to yield novel critical exponents because at the Hopf bifurcation the angular velocity in phase space is finite (see Eq. (37) for mean-field and Fig. 24 for simulation evidence), and so the phase-space angular momentum scales with $\langle s^2 \rangle$.

As predicted by the mean-field analysis, the phase-space trajectories become circular when approaching the transition line (Fig. 13), supporting a CGL-like behavior as explained in Sec. VB2. Moreover, renormalization group studies based on the ϵ -expansion suggest that the synchronization transition of the CGL equation with additive noise belongs to the same universality class as the

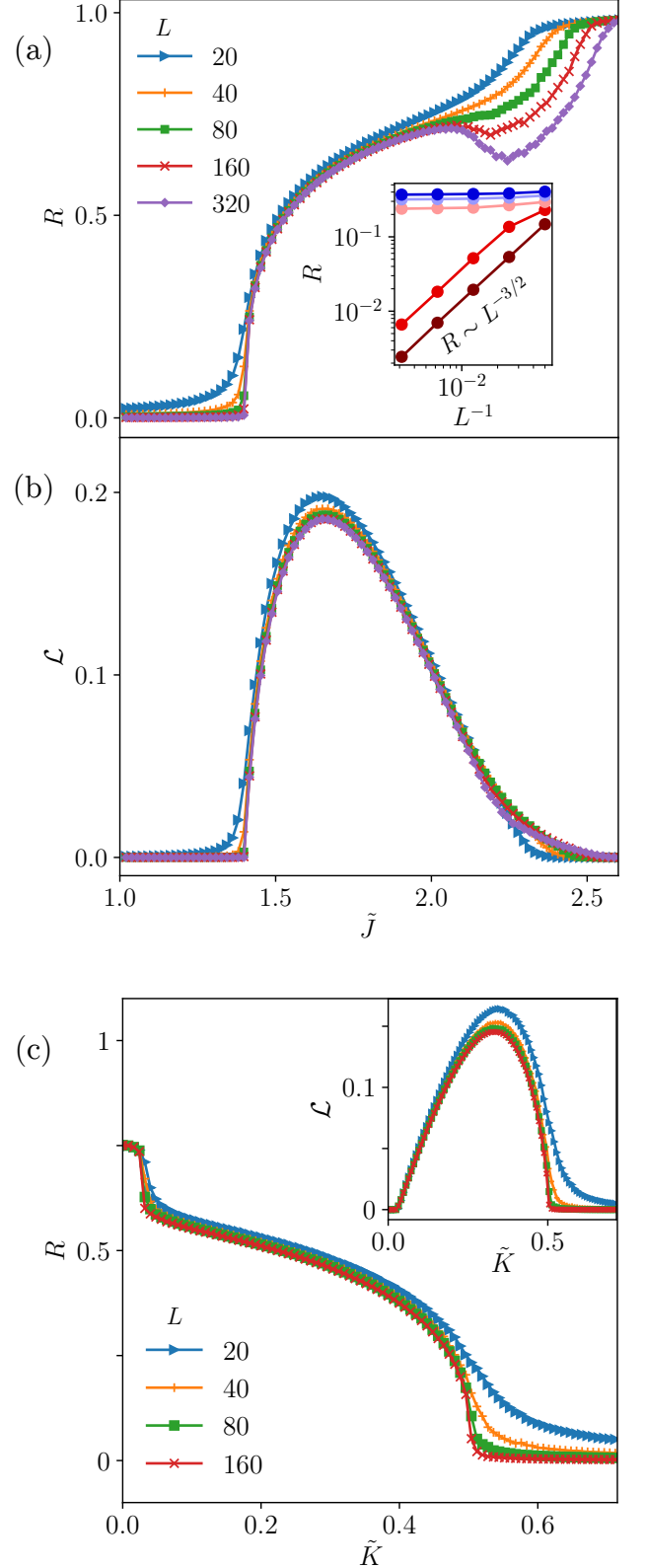


Fig. 12. Phase transition from disorder to swap in 3D. (a) R as a function of \tilde{J} for $\tilde{K} = 0.3$ shown for different linear system size L . Inset: R vs. L^{-1} for $\tilde{K} = 0.3$ and $\tilde{J} = 1.38, 1.40, 1.42, 1.43, 1.45$ from bottom to top on a log-log scale. (b) \mathcal{L} as a function of \tilde{J} with the same parameters as panel a. (c) R vs. \tilde{K} for $\tilde{J} = 1.5$ for different L . Phase-space angular momentum is shown in the inset. Obtained from MC simulations.

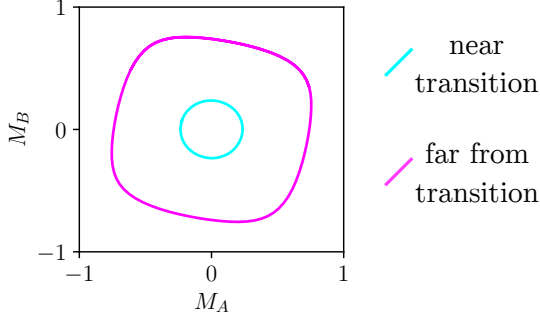


Fig. 13. Phase-space trajectories close to and far from the transition from disorder to swap in 3D. M_B as a function of M_A in steady state for $\tilde{J} = 1.35$ (cyan) and $\tilde{J} = 1.5$ (magenta), with $\tilde{K} = 0.1$ and $L = 320$ (see points marked by stars in Fig. 11). Obtained from MC simulations.

phase transition from disorder to long-range order in the XY model [89, 90]. Thus, in what follows we will compare our results to the 3D XY critical exponents and to the 3D Ising critical exponents corresponding to the $\tilde{K} = 0$ case.

According to the theory of finite-size scaling [186, 187], in a finite system the order parameter R , the susceptibility χ , defined as

$$\chi = L^d (\langle s^2 \rangle - \langle s \rangle^2), \quad (55)$$

and the Binder cumulant [188] defined as

$$U = 1 - \frac{\langle s^4 \rangle}{3\langle s^2 \rangle^2}, \quad (56)$$

satisfy the following relations in the vicinity of the critical point \tilde{J}_c (assuming fixed \tilde{K}) and for large system size:

$$\begin{aligned} R &= L^{-\beta/\nu} \hat{R}(L^{1/\nu}(\tilde{J} - \tilde{J}_c)) \\ \chi &= L^{\gamma/\nu} \hat{\chi}(L^{1/\nu}(\tilde{J} - \tilde{J}_c)) \\ U &= \hat{U}(L^{1/\nu}(\tilde{J} - \tilde{J}_c)). \end{aligned} \quad (57)$$

Here, $\hat{\chi}(x)$, $\hat{R}(x)$, and $\hat{U}(x)$ are called the scaling functions, and ν , γ and β are the critical exponents $\xi \sim |\tilde{J} - \tilde{J}_c|^{-\nu}$ where ξ is the correlation length, $\chi \sim |\tilde{J} - \tilde{J}_c|^{-\gamma}$, and $R \sim |\tilde{J} - \tilde{J}_c|^\beta$ (for $\tilde{J} > \tilde{J}_c$). The scaling functions are independent of L and converge to a finite value at the critical point (*i.e.* $\hat{R}(0)$, $\hat{\chi}(0)$ and $\hat{U}(0)$ are constants). In what follows we assume that the finite-size scaling theory holds out of equilibrium, as is often done [189]. We set $\tilde{K} = 0.1$ where numerical evidence shows that the transition is continuous (like a second-order transition).

The critical point \tilde{J}_c is found using the Binder cumulant. Away from the critical point, the value of U depends on system size, approaching $1/3$ in the disordered and $2/3$ in the ordered regime as $L \rightarrow \infty$ [190, 191]. However, at the critical point U approaches a fixed value $U(\tilde{J}_c) = U^*$ independent of L . Hence, the critical point is found from

the intersection point of all the U vs. \tilde{J} curves plotted for different system sizes. Figure 14a shows that indeed all the curves cross at a single point ($\tilde{J}_c = 1.34614 \pm 0.00001$ for $\tilde{K} = 0.1$).

In addition to U , we plot χ and R as a function of \tilde{J} , see Fig. 14a-c. The data points are interpolated using a cubic spline method with ‘not-a-knot’ boundary conditions as implemented in `scipy.interpolate.CubicSpline` [192]. For each linear system size L , we find the slope of U at the critical point, $dU/d\tilde{J}|_{\tilde{J}=\tilde{J}_c}(L)$, the maximum of χ , $\chi_{\max}(L)$, and the value of R at the critical point, $R(\tilde{J} = \tilde{J}_c, L)$. We then use the finite-size scaling relations (which can be derived from Eq. (57) [186, 187])

$$\begin{aligned} \frac{dU}{d\tilde{J}}|_{\tilde{J}=\tilde{J}_c}(L) &= aL^{1/\nu} \\ \chi_{\max}(L) &= bL^{\gamma/\nu} \\ R(\tilde{J} = \tilde{J}_c, L) &= cL^{-\beta/\nu} \end{aligned} \quad (58)$$

and perform linear fits by taking the logarithm of both sides of the equations (Fig. 14(d-f)). The procedure outlined here yields the critical exponents. To ensure good accuracy, all averages are taken using 10^6 samples. To make the samples approximately independent, they are separated by two correlation times of s (the correlation times were computed at $\tilde{J} = 1.346$). Simulation runs are initialized in a fully disordered state. The error is estimated using the bootstrap method [186, 193]: the same procedure is repeated for multiple samples where each sample is constructed by drawing 10^6 measurements of s randomly from our data while allowing duplicates. The standard deviation of the critical exponents is estimated by the standard deviation calculated from 10^5 bootstrap resamplings of the data (Fig. 14(g-i)). This estimated error is due to finite sampling but does not include other systematic errors (*e.g.* finite-size corrections to Eqs. (57–58) [187]). Our results are

$$\begin{aligned} \nu &= 0.675 \pm 0.005 \\ \gamma &= 1.328 \pm 0.009 \\ \beta &= 0.347 \pm 0.002, \end{aligned} \quad (59)$$

which are all in good agreement with 3D XY critical exponents $\nu_{XY} = 0.672$, $\gamma_{XY} = 1.318$, $\beta_{XY} = 0.349$ [194, 195], more so than with 3D Ising critical exponents $\nu_I = 0.630$, $\gamma_I = 1.237$, $\beta_I = 0.326$ [194], see graphical comparison in Fig. 15. Further evidence that the disorder-to-swap phase transition belongs to the same universality class as the disorder-to-order XY phase transition is given by the value of the Binder cumulant as the critical point, $U(\tilde{J}_c) = U^*$, which is also universal [188]. We find

$$U^* = 0.5877 \pm 0.0002, \quad (60)$$

consistent with studies on the 3D XY model reporting $U^* \approx 0.586$ [196]. In contrast, the 3D Ising model yields $U^* \approx 0.467$ [197].

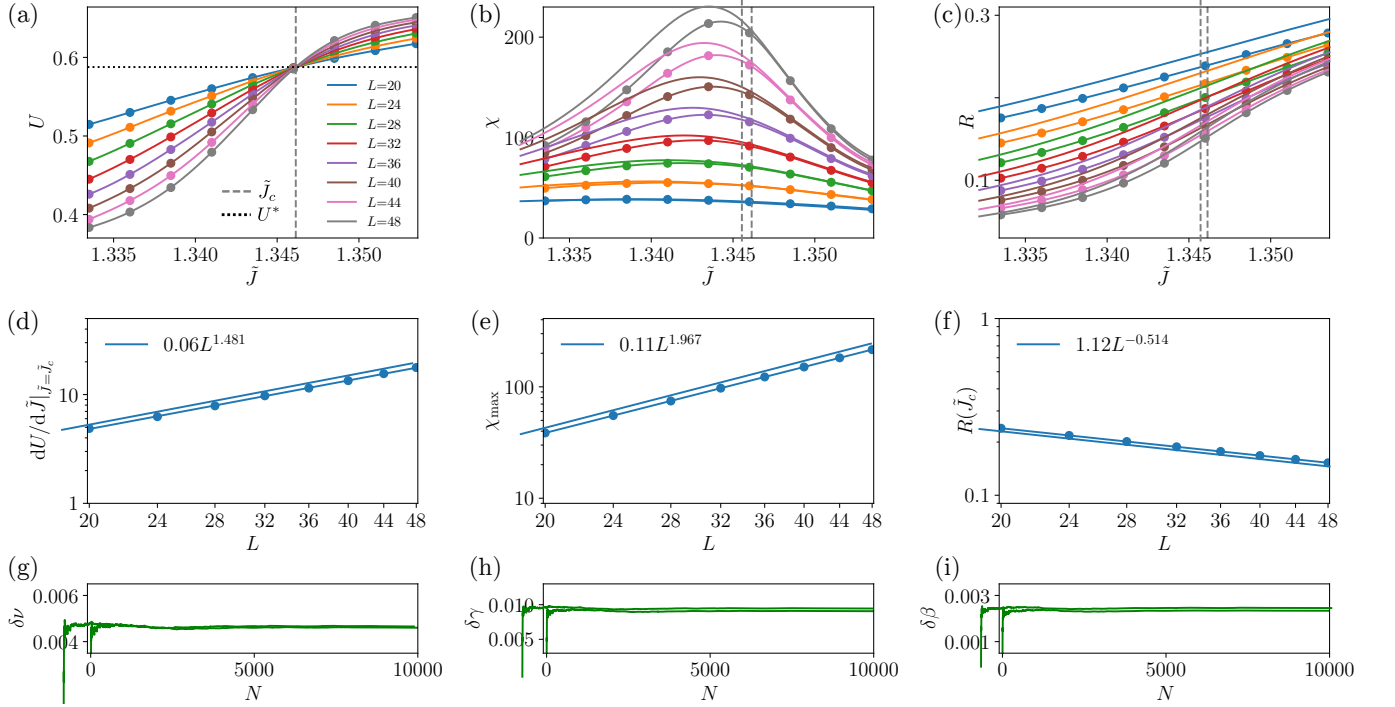


Fig. 14. Calculation of the critical exponents of the 3D NR Ising model. We set $\tilde{K} = 0.1$. (a-c) The Binder cumulant U , the susceptibility χ , and the order parameter R as a function of \tilde{J} for linear system sizes $L = 20, 24, 28, 32, 36, 40, 44, 48$. The vertical dashed grey line indicates the critical point, $\tilde{J}_c = 1.34614$ while the horizontal dotted black line indicates that value of the Binder cumulant at the critical point, $U^* = 0.5877$. Each point is calculated by averaging over 10^6 samples of s . (d-f) $dU/d\tilde{J}|_{\tilde{J}=\tilde{J}_c}$, χ_{\max} and $R(\tilde{J}_c)$ as a function of L on a log-log scale. Dots are extracted from analyzing panels a-c and full lines indicate best linear fits. (g-i) Standard error of ν , γ , and β as a function of the number of bootstrap samples (10^5 bootstrap resamplings are performed in total).

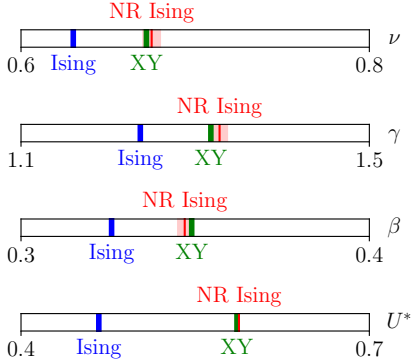


Fig. 15. Compatibility with XY universality class. The critical exponents and the Binder cumulant at the critical point of the 3D nonreciprocal Ising model (red) for $\tilde{K} = 0.1$ extracted from finite-size scaling analysis along with their standard deviation represented by a semi-transparent red rectangle, and compared with the 3D Ising model (blue) and the 3D XY model (green).

B. Time-crystal behavior

On top of being globally ordered and time-dependent, the 3D swap phase possesses another notable prop-

erty: its coherence time diverges because of its many-body nature, making it a *time crystal* [134, 135, 140–144, 146, 147].

To understand this feature, consider a single limit cycle oscillator subject to noise. This can be represented by the zero-dimensional mean-field equation of the non-reciprocal Ising model with added noise, defined as

$$\frac{dm_\alpha}{dt} = -m_\alpha + \tanh(\tilde{J}m_\alpha + \tilde{K}\varepsilon_{\alpha\beta}m_\beta) + \eta_\alpha, \quad (61)$$

where η_α is white noise satisfying $\langle \eta_\alpha(t) \rangle = 0$ and $\langle \eta_\alpha(t)\eta_\beta(t') \rangle = \zeta\delta_{\alpha\beta}\delta(t-t')$ with ζ determining the noise amplitude. Figure 16 shows a numerical solution of Eq. (61) (panel a) along with the auto-correlation function of m_A (panel d). Such auto-correlation of an observable x is defined here as

$$C_x(\tau) = \frac{\langle x(t)x(t+\tau) \rangle_t}{\langle x(t)^2 \rangle_t}. \quad (62)$$

Note that $\langle x \rangle_t = 0$. If this was not the case, one should replace $x(t)$ with $x(t) - \langle x \rangle_t$ in Eq. (62). As seen in Figure 16, even though the magnetization performs quite regular oscillations, its auto-correlation function decays, thereby indicating that this oscillator eventually forgets its initial phase [129, 130, 198–207].

In many-body systems, however, interactions can overcome noise, producing coherent oscillations over arbitrarily long periods [94, 95, 97–100, 102, 111–117, 127, 208–212]. Figure 16 shows that in the 3D nonreciprocal Ising model, for large system size, temporal correlations of individual spins σ_i^A (panel e) and of the total magnetization M_A (panel f) persist and do not decay over large times, making it a robust clock. This robust clock is an emergent feature of our model which does not rely on any periodic drive externally imposing a phase.

The different behaviors of the time correlations in the noisy clock Eq. (61) and in the 3D NR Ising can be respectively compared to spatial density correlations in a liquid (which decay with distance) and a solid (which is maintained over arbitrarily large distances). Such comparison makes Eq. (61) a “time liquid” and the 3D NR Ising a “time crystal” which has infinite coherence time.

To substantiate our claim, we find the coherence time of the swap phase in the 3D NR Ising model by determining the decay rate of the auto-correlation’s envelope, $\tilde{C}_{M_A}(\tau)$. We construct $\tilde{C}_{M_A}(\tau)$ by interpolating the peaks of $|C_{M_A}(\tau)|$. We then identify the coherence time τ_c as the time for which

$$\tilde{C}_{M_A}(\tau_c) = \exp(-1). \quad (63)$$

Figure 17 shows that τ_c increases with system size as

$$\tau_c(L) \sim L^3, \quad (64)$$

i.e. linearly with the number of spins, thereby proving the perfect time-crystal behavior of the 3D NR Ising in the thermodynamic limit. A similar scaling for τ_c has been observed in a periodically driven 2D system in Ref. [213].

This result suggests the existence of perfectly coherent oscillations in the thermodynamic limit $L \rightarrow \infty$, which can be seen as a breaking of ergodicity [214–216]. Even at arbitrarily long times, the probability distribution function $P(t) \equiv U(t)P_0$ does not necessarily converge to a constant stationary distribution P^{ss} such that $U(t)P^{\text{ss}} = P^{\text{ss}}$. Here, $U(t)$ is the evolution operator acting on probability distributions, *e.g.* defined by the master equation (13). Instead, we expect that the system evolves towards a limit-cycle P_{LC} satisfying $P_{\text{LC}}(t) = P_{\text{LC}}(t + T_{\text{osc}})$ where T_{osc} is the oscillation period [217]. As a consequence, the distance between the distributions obtained from evolving two initial conditions P_1 and P_2 does not necessarily go to zero at long times, *i.e.* one can have

$$\lim_{t \rightarrow \infty} \|U(t)P_1 - U(t)P_2\| \neq 0 \quad (65)$$

because the many-body oscillator remembers its phase (*i.e.* its position on the limit cycle), which is encoded in the probability distribution.

We can combine Eq. (64) with the conjecture of Ref. [131] to obtain a bound on the minimum rate of entropy production required to maintain the oscillations.

This conjecture bounds the average entropy per oscillation ΔS by the number of coherent oscillations $\mathcal{N} \equiv \tau_c/T_{\text{osc}}$ through the inequality $\Delta S \geq 4\pi^2\mathcal{N}$. As a consequence, the rate of entropy production per unit volume

$$\dot{s} \equiv \frac{\Delta S}{L^d T_{\text{osc}}} \quad (66)$$

must satisfy

$$\dot{s} \geq \frac{4\pi^2}{T_{\text{osc}}^2} \frac{\tau_c(L)}{L^d}. \quad (67)$$

In the stable swap phase T_{osc} does not depend on L (it converges to a constant as $L \rightarrow \infty$, see Fig. 24a in Sec. IX A). As $\tau_c(L) \sim L^d$, this bound converges to a finite value when $L \rightarrow \infty$, meaning that there is a finite minimal cost per oscillator to maintain the time-crystal state. The fit in the inset of Fig. 17b provides τ_c/L^d for the example considered in the plot. In Appendix A we calculate the entropy production explicitly from simulations under the assumption of local detailed balance, and show that \dot{s} converges to a finite value and that this value indeed exceeds the lower bound provided by Eq. (67).

Note that ordered oscillations and infinite coherence time are not decoupled properties. It is plausible that a locally coupled system can maintain spatially ordered oscillations over arbitrarily large distances only if all its parts adhere to the same prescribed phase determined by the initial conditions.

C. The phase transition from disorder to swap in the high (\tilde{J}, \tilde{K}) regime

At high \tilde{J} and \tilde{K} values, the transition from disorder to swap is different than for small \tilde{J} and \tilde{K} values. This is seen in Fig. 11 where the change in R and \mathcal{L} at the phase transition appears to become more abrupt in the upper right region, compared to the lower left region. We further analyze this transition in Fig. 18. Figure 18a shows the order parameters as a function of \tilde{K} , for fixed $\tilde{J} = 2$, and various system sizes. The plots of R and \mathcal{L} vs. \tilde{K} do not seem to converge to a second-order phase transition in which the order parameters are continuous. Instead, an abrupt change in R and \mathcal{L} emerges at high system sizes, suggesting a discontinuity as in first-order phase transitions. A clear critical point cannot be identified since convergence is not reached at $L = 320$, the largest linear system size in our simulations (see $0.8 \lesssim \tilde{K} \lesssim 1.1$ region in Fig. 18a).

The sharp decrease in synchronization is caused by the emergence of highly noisy scroll waves that destructs the order. This is seen in Fig. 18b showing a 2D-slice snapshot of θ taken from the 3D simulation. Scroll waves are the 3D analog of spiral waves, having line defects that are typically closed into rings instead of point defects [86, 142, 218, 219] (see also Movie 3 and Fig. 27 in Sec. X in which the scroll waves are more visible). They

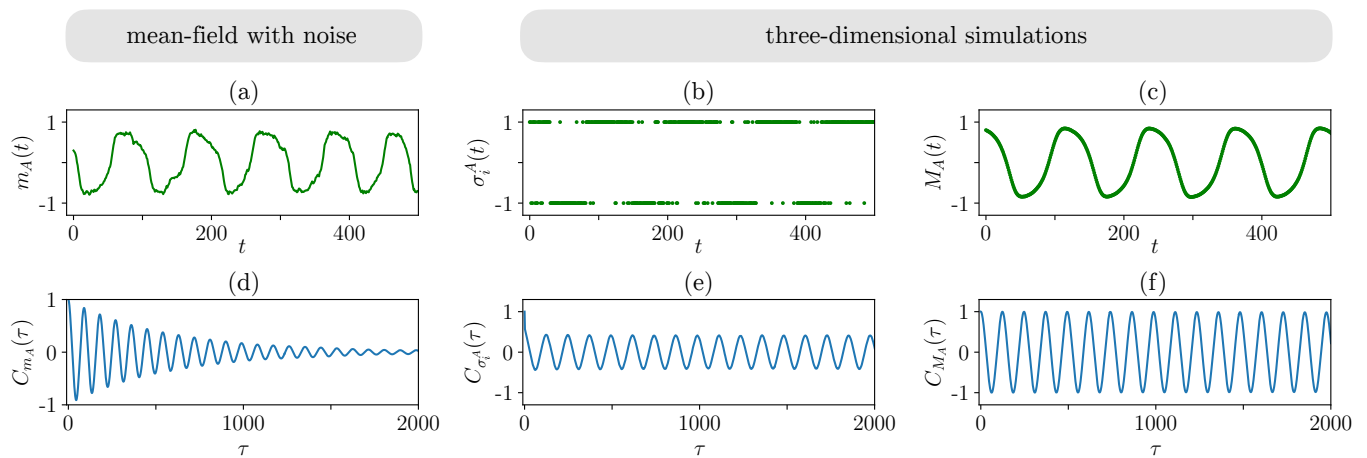


Fig. 16. Time correlations in the swap phase of the NR Ising model. (a) Time evolution of m_A in the zero-dimensional mean-field equation with added noise. (b) Time evolution of a single spin σ_i^A in the 3D NR Ising model. (c) Time evolution of the total magnetization of A -spins, M_A , in the 3D NR Ising model. (d-f) Auto-correlation function of m_A , σ_i^A , and M_A , respectively (defined in Eq. (62)). Panels a and d are obtained from numerical integration of Eq. (61) with the parameters: $\tilde{J} = 1.2$, $\tilde{K} = 0.12$, $\zeta = 0.0009$, $dt = 0.01$. Panels b-c and e-f are obtained from MC simulation with the parameters: $\tilde{J} = 1.6$, $\tilde{K} = 0.1$, $L = 80$.

also have spiral cross sections, which is seen in the 2D-cut θ snapshot in Fig. 18b and in its coarse-grained version, Fig. 18c (the latter figure makes the defects more apparent by averaging out the noise). We discuss scroll waves in more detail in Sec. X.

The destruction of the swap phase by scroll waves is slightly reminiscent of the destruction of order in 2D due to spiral defects (compare Fig. 9e-f with Fig. 18a), except that here, it appears that the destruction only occurs for a limited range of high \tilde{J} and \tilde{K} values. Due to the size limitation of our simulations we cannot determine what portion of the 3D swap phase is destroyed by the scroll waves or what kind of phase transition is associated with this destruction, although it appears to be first-order-like (in the sense that the order parameters are discontinuous).

D. Why is the swap phase stable in 3D?

Our numerical evidence points to the existence of a stable swap phase. This relates to a longstanding question: can time-periodic states of noisy many-body systems with short-range interactions be stable in the thermodynamic limit [97–100, 102, 111–117, 127, 208–212]. References [99, 100, 102] distinguished two cases, depending on whether the spontaneously broken time-translation invariance is discrete or continuous (Fig. 19a). In systems that evolve in discrete time as our Monte-Carlo simulation, this depends on the type of oscillations: commensurate vs. incommensurate. When the period of the oscillations is *commensurate*, i.e., a multiple of the discrete time-unit (a case referred to as “periodic k -cycle”), a discrete time-translation symmetry is broken. In that case, it was argued in [99] that the growth of out-of-

phase droplets [220] destabilizes long-range ordered oscillations. That is because flat domain walls are expected to have a non-vanishing velocity, unlike in equilibrium [221], suggesting that a fluctuation producing a large enough droplet, can expand rather than shrink. A similar destabilization mechanism has been observed in discrete-symmetry flocks [222].

In the *incommensurate* case, i.e. when the oscillation period is not a multiple of the discrete time-unit (e.g. the time step of the Monte-Carlo simulation), the discrete-time system is equivalent to continuous-time one (the discreteness is irrelevant). The oscillatory state then breaks a continuous time-translation symmetry, which can be seen by the fact that the oscillation’s phase at a given time can take any value between 0 and 2π . In continuous symmetry breaking, domain walls smear out (as in the XY model) and thus the destabilization-by-droplets argument does not apply [100, 102, 223].

In the nonreciprocal Ising model studied here, the oscillation period is incommensurate with the Monte-Carlo time step. This is seen both in Fig. 19b where a continuous limit cycle is formed in the infinite-time limit, and in Fig. 19c where the period of the oscillation, measured as twice the average time between two subsequent sign flips of M_A , is shown to change continuously with the interaction parameters (a continuously changing number is in general incommensurate with 1). This means that, while stable oscillations are not guaranteed, they are not ruled out by the droplet argument in Ref. [99], see also Ref. [212]. Figure 19d further exemplifies this: it shows an analysis of 3D simulations of both the Ising model and the nonreciprocal Ising model with a flat domain wall introduced at location $y = 0$ at time $t = 0$ (the domain wall separates oppositely magnetized states for Ising, and two swap states at different phases for nonreciprocal

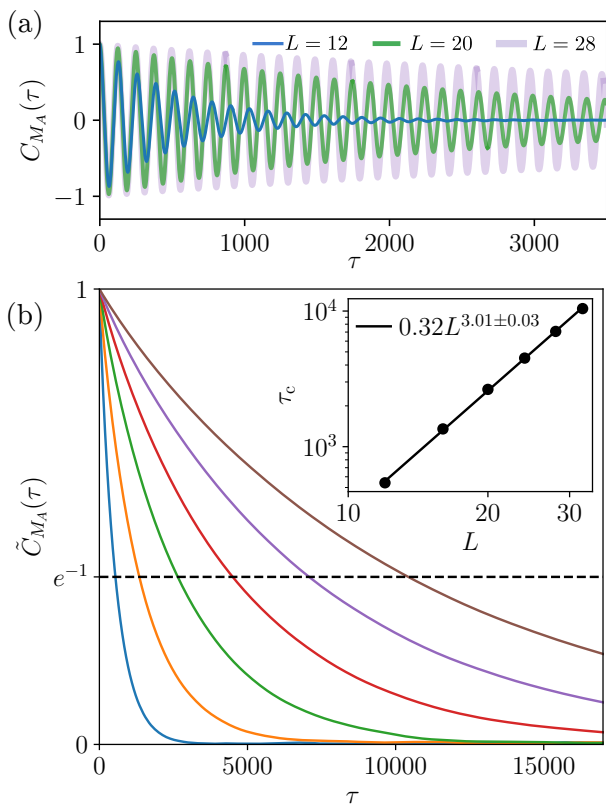


Fig. 17. Diverging coherence time of the swap phase in the 3D NR Ising model. (a) The correlation function $C_{M_A}(\tau)$ of the total magnetization of A -spins, for different system sizes. Correlations persist over longer times as system size increases. (b) The envelope of the auto-correlation function, $\tilde{C}_{M_A}(\tau)$, shown for linear system sizes $L = 12, 16, 20, 24, 28, 32$ (from bottom to top). The coherence time τ_c (Eq. (63)) is calculated from the intersection of $\tilde{C}_{M_A}(\tau)$ with e^{-1} (dashed black line). Inset: τ_c as a function of L on a log-log scale. The dots are calculated from the data in the main panel and the line is the best linear fit, which has a slope of 3.01 with a standard error of 0.03. The coherence time is proportional to L^d , supporting a time-crystal behavior. Obtained from MC simulations with the coupling parameters $\tilde{J} = 1.6$ and $\tilde{K} = 0.1$.

Ising). As time evolves, the domain wall in the nonreciprocal Ising system is shown to widen and dissipate (on top of slightly moving in the $+\hat{y}$ direction), unlike the domain wall in the Ising system which remain steady. This suggests that there are no stable domain wall between oscillating states in the swap phase of the nonreciprocal Ising model.

The existence of a broken continuous symmetry (time-translation invariance) suggests a parallel with the Mermin-Wagner theorem [82, 110] in the time domain [91, 109]: continuous changes in the oscillation phase over space may behave as generalized Goldstone modes and their fluctuations preclude order in 2D yet allow for order in 3D and beyond. Note that this discussion disregards any potential phase transition to quasi-long

range order in 2D that would resemble the Berezinskii-Kosterlitz-Thouless (BKT) transition in the XY model. While we have not proven the absence of such a phase transition in the nonreciprocal Ising model, we do not expect it to be present. The similarity with the XY model blurs when we depart from the Hopf bifurcation towards the high \tilde{J} regime (where one might have hoped to observe a phase transition to quasi-long range order), since the discrete symmetry of the spins causes a SNIC bifurcation in mean-field and droplet nucleation in simulations (Sec. IX). Even the CGL equation with additive noise, which is rotationally symmetric and hence more related to the XY model than the NR Ising model, was suggested to not have a BKT transition [106, 107, 177].

An analogy between (de)synchronization and surface roughening provides further reasons to expect the swap phase to be stable in 3D and not in 2D. If we add random noise to the mean-field equation (30), it takes the form of a noisy reaction-diffusion system

$$\frac{\partial \vec{X}}{\partial t} = F(\vec{X}) + D\nabla^2 \vec{X} + \text{noise}, \quad (68)$$

where $\vec{X} = x_1, \dots, x_n$ and D can be a matrix. Now assume that the noiseless and diffusion-less version of Eq. (68) has a limit cycle in steady state. To test whether the addition of diffusion and noise allows for synchronized oscillations, we assume that we are deep within the synchronized regime, where fluctuations from the global limit cycle are small and can be treated perturbatively. In this case, we can focus on the phase variable that describes the position of the system on the limit cycle, while neglecting other degrees of freedom. This is known as a phase reduction, see Refs. [85, 224–227]. Under certain approximations, Eq. (68) can then be mapped to the Kardar–Parisi–Zhang (KPZ) equation [103]

$$\frac{\partial \Psi}{\partial t} = \alpha \nabla^2 \Psi + \beta (\nabla \Psi)^2 + \text{noise} \quad (69)$$

where the deviation Ψ of the local phase with respect to the phase of the deterministic limit cycle plays the role of the surface height in the KPZ equation (Fig. 20), see Refs. [85, 102, 106, 107, 228]. The KPZ equation predicts that interfaces are always rough in 2D, but that there is a phase transition between rough and smooth interfaces in 3D [229]. This suggests, by analogy, that a spatially coherent oscillating phase can exist in 3D, but not in 2D. Note, however, that the variable Ψ in Eq. (69) is an angle (defined on a compact space, the circle S^1), so the results on the usual KPZ equation cannot be directly applied. In particular, the fact that the phase Ψ is compact allows for the existence of topological defects, that may change the physics. We refer to Refs. [102, 106, 107, 230–232] for further details on the compact KPZ equation. In 3D, defect rings are expected to be small (at least for certain range of \tilde{J} and \tilde{K}) and hence not to completely destroy long-range order [102].

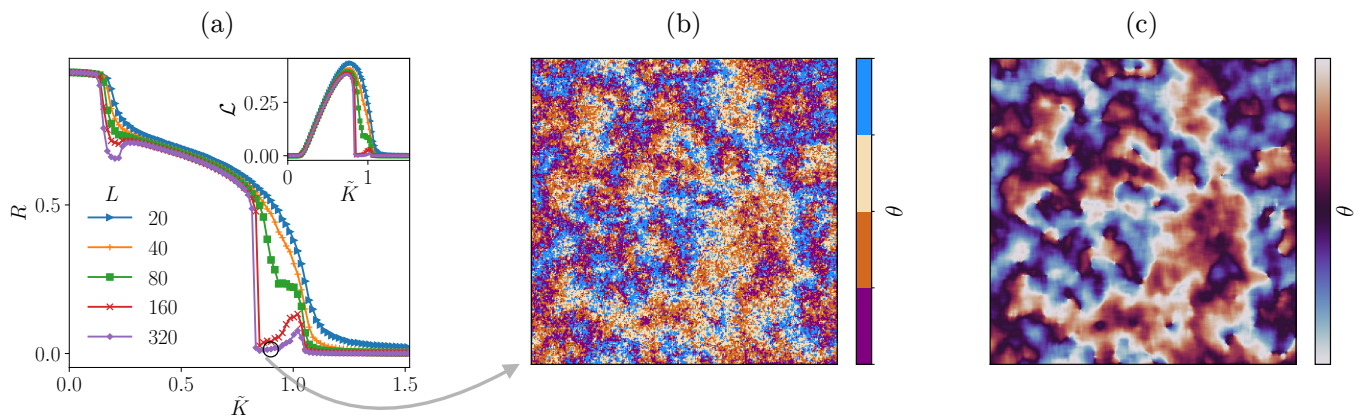


Fig. 18. Destruction of the second-order phase transition due to scroll waves in the high \tilde{K} and high \tilde{J} regime. (a) R vs. \tilde{K} for $\tilde{J} = 2$. Phase-space angular momentum is shown in the inset. (b) θ snapshot of a 2D slice from a 3D simulation with the parameters $\tilde{J} = 2$, $\tilde{K} = 0.9$, $L = 320$, corresponding to the point marked by a black hollow circle on panel a. (c) The same snapshot coarse-grained over 10×10 lattice sites. The snapshots show the destruction of order by scroll waves (appearing as spiral defects in the 2D cut). Obtained from MC simulations.

IX. DESTRUCTION OF THE STATIC-ORDER PHASE VIA DROPLETS

In finite systems, a ferromagnetic-like state with static order is observed both in 2D and 3D. As system size increases, however, our numerical simulations indicate that this static state is destabilized. This is supported by Figs. 9e-f and 12a-b (right parts) showing R and \mathcal{L} as a function of \tilde{J} (for a fixed \tilde{K}). The \tilde{J} -transition-point between static order and oscillations in finite systems (indicated by a sharp change in the slope of R and \mathcal{L} becoming zero) increases with system size in a way that does not seem to converge to a finite \tilde{J} . Figures 12c and 18a showing R and \mathcal{L} as a function of \tilde{K} (for a fixed \tilde{J}) have a very small region of static order (when \tilde{K} is close to zero) and it is hard to see what is its fate in the thermodynamic limit. However, this region seems to shrink when L increases in Fig 18a, suggesting a destabilization of the static-order phase.

The static-order phase is destabilized by nucleation of droplets that grow and flip the magnetization, in alternating order of A- and B-spins. This mechanism is demonstrated in Fig. 21, where snapshots of the spins at different times are shown for increasing system sizes, in a 2D system. The full evolution is shown in Movie 4. For $L = 10$ (Fig. 21a), both species do not flip their magnetization. There are attempts of B-spins to nucleate droplets, but those shrink and disappear. For $L = 40$ (Fig. 21b), the system is no longer static: a handful of B-spins droplets (one clearly observed in the figure) surpass a certain critical droplet size, grow and flip the magnetization. Then, the same occurs for the A-spins, and so on, leading to an oscillatory behavior of $M_A(t)$ and $M_B(t)$, but with intermediate periods in which $M_A(t)$ and $M_B(t)$ are constants. When $L = 200$ (Fig. 21c), multiple droplets ($\gg 1$) drive the magnetization flipping

of each species, making the $M_A(t)$ and $M_B(t)$ curves smooth at all times, *i.e.*, there is no finite period of time in which the magnetization is constant and the system could be called static. We note that the figure shows a 2D system but a similar behavior is observed in 3D.

To see why nonreciprocity allows droplets to grow, in contrast with the equilibrium Ising model where they tend to shrink, assume first that the system is in the static-order phase, so most spins in both lattices are up (Fig. 22a) [96]. We further assume K is very small, which is when static order is most likely to be stable. As long as the system is static, it can be mapped into two equilibrium Ising models with opposite magnetic fields, with energy

$$E = -J \sum_{\langle i,j \rangle} \sigma_i \sigma_j - H \sum_i \sigma_i \quad (70)$$

where $H \approx K$ for A-spins and $H \approx -K$ for B-spins (see Eq. (11) and Fig. 22b). While sub-system A is in a global free energy minimum in the effective equilibrium system, sub-system B is in a metastable state, as it prefers a state with opposite magnetization. Provided that the system size is large enough, sub-system B then transitions to its global minimum by nucleating droplets larger than a critical size ρ_c above which the effective magnetic field, which acts on the volume of the droplet, overcomes the nearest neighbor attraction, imposing surface tension, which makes the droplet grow [96, 99, 233, 234] (Fig. 22c). After a droplet has expanded beyond ρ_c , the stable sub-system becomes metastable and nucleates droplets, and so on (Fig. 22d). Crucially, due to the symmetry between A and B spins, both droplet types expand with the same speed. Therefore, a nested droplet remains much smaller than its “mother-droplet” until the latter reaches the system size or collides with other droplets (see Sec. XII in which this symmetry is absent). A simplified view of this

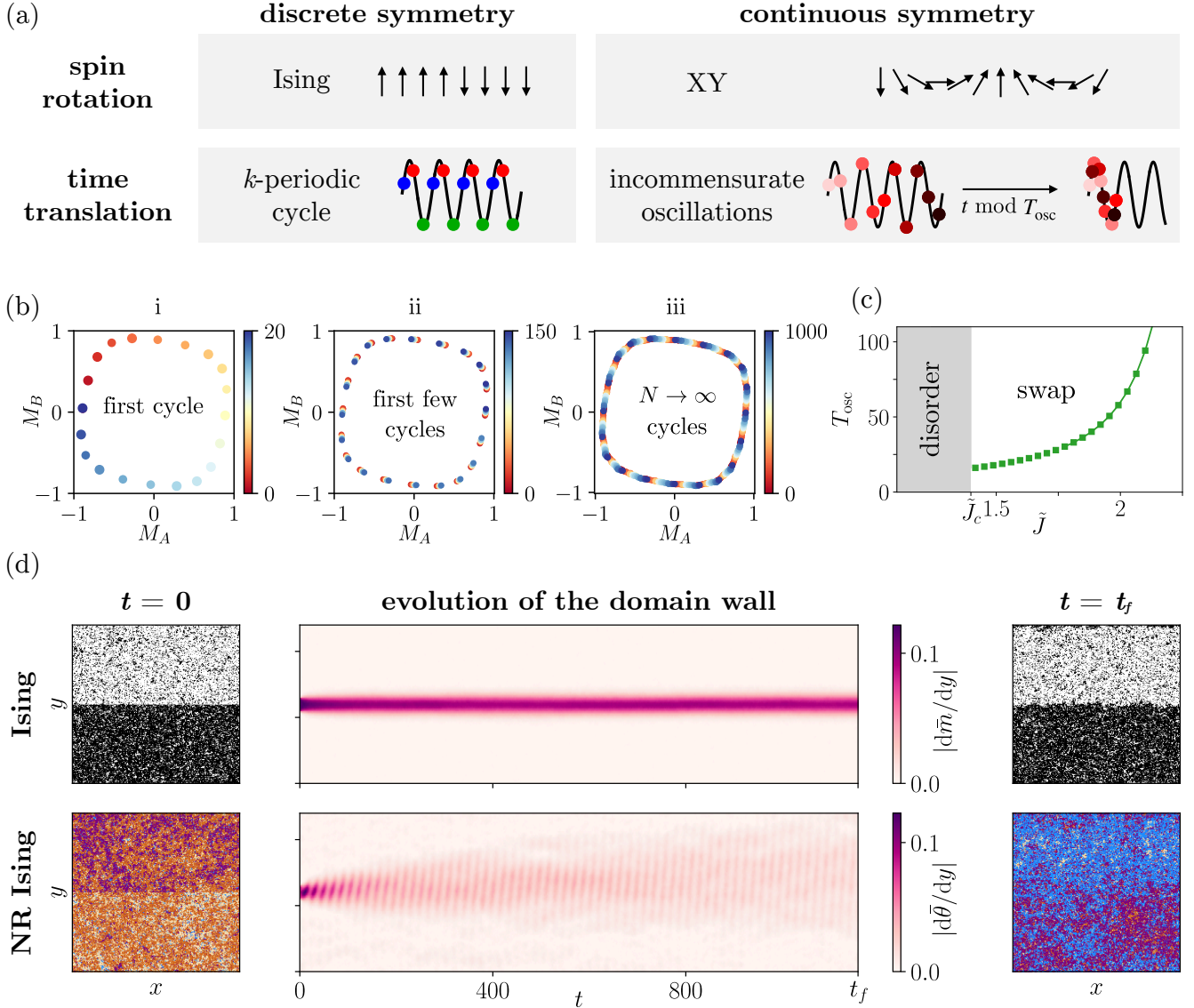


Fig. 19. Continuous symmetry breaking of the swap phase. (a) Comparison of discrete and continuous symmetry breaking in equilibrium and out-of-equilibrium models. (b) M_B vs. M_A for $\tilde{K} = 0.5$, $\tilde{J} = 2$, and $L = 80$. i,ii, and iii show increasing numbers of MC sweeps. Each point is colored according to the sweep it corresponds to. Since the oscillation period is incommensurate, a continuous limit cycle is sampled in the infinite time limit. Hence, a continuous symmetry is broken. (c) Oscillation period of the magnetizations, T_{osc} , in the 3D system as a function of \tilde{J} for $\tilde{K} = 0.3$ and $L = 80$. T_{osc} is measured as twice the average time between two subsequent sign flips of M_A . The continuous dependence of T_{osc} on the coupling parameter indicates incommensurate oscillations. (d) comparison between domain walls in 3D the Ising model (first row) and in the 3D NR Ising model (second row). At $t = 0$, the two systems were in steady state and then perturbed by a domain wall. The domain wall is created by flipping the magnetization (Ising) and shifting the oscillation phase (NR Ising) for all spins located at $y > L/2$. System parameters are: $\tilde{J} = 1.4$ (Ising) and $\tilde{J} = 1.5$, $\tilde{K} = 0.1$ (NR Ising), and $L = 320$. i and iii are Snapshots of σ (Ising) and θ (NR Ising, see color code in Fig. 2) in a 2D slice taken from a 3D simulation at $t = 0$ and $t = 1157$, respectively. ii Kymograph of $|d\tilde{m}/dy|$ (Ising) and $|d\tilde{\theta}/dy|$ (NR Ising), defined by the discrete symmetric derivative $df/dy \equiv |(f_{y+5} - f_{y-5})/10|$, where \tilde{m} is the magnetization and $\tilde{\theta}$ is the phase, both averaged over the xz plane. The smearing out of the dark pink region indicates the dissipation of the domain wall. Panels b-d are obtained from MC simulations.

mechanism can be found in defining a “selfish free energy” for the zero-dimensional mean-field equation, see Appendix E.

The argument sketched above relies on ρ_c being finite,

which is the case in any finite dimension (and finite couplings \tilde{J} and \tilde{K}) because the volume term ultimately dominates at sufficiently large droplet sizes. Hence, we conjecture that in the fully anti-symmetric nonrecipro-

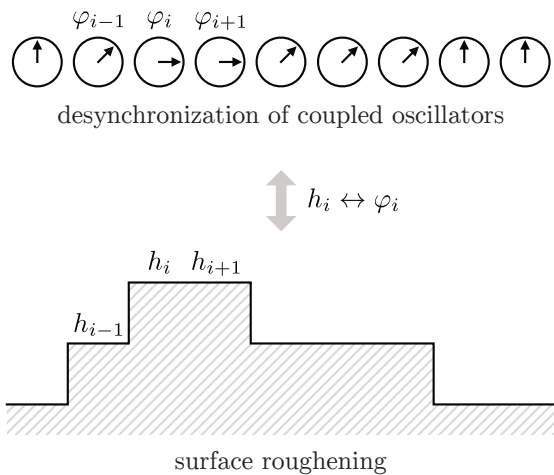


Fig. 20. Mapping between surface roughening and desynchronisation. Schematic drawing of the mapping between coupled limit cycle oscillators (top) and surface roughening described by the KPZ equation (bottom). The phase φ_i of the oscillator at position i is mapped to a height h_i .

cal Ising model, the static-order phase is unstable in the thermodynamic limit in any finite dimension.

A. Between static order and swap: the droplet regime

The droplet mechanism explained above means that as system size increases, a regime of droplet-induced swap develops instead of the static-order phase. In 2D, this regime separates static-order from disorder, while in 3D, it separates static-order from the noisy homogeneous swap regime.

In the droplet-induced swap regime, the critical droplet size increases as \tilde{J} increases (and as \tilde{K} decreases). As a result, the droplets become more sparse and the distance they travel before colliding with each other increases. Eventually, \tilde{J} becomes large enough (or \tilde{K} small enough) that the critical droplet size becomes larger than the system size. In that case, the magnetization can flip when fluctuations are of the order of the system size, in the same way as in the usual equilibrium Ising model.

This is demonstrated in Fig. 23 where 2D-slice snapshots of the θ field, as well as the magnetizations of the two species as a function of time, are shown for a 3D system with linear size $L = 80$ at increasing values of \tilde{J} (and decreasing values of \tilde{K}). For small \tilde{J} (high \tilde{K}), the 3D system is in a noisy homogeneous swap phase. There are no apparent droplets but rather noisy patterns without a well-defined shape (Fig. 23a,e). Put differently, independent fluctuations do not have time to expand significantly before colliding. For larger \tilde{J} (smaller \tilde{K}) values we observe droplets that drive the magnetization flips (Fig. 23b-c,f-g). For an even larger \tilde{J} (smaller \tilde{K}), no droplets are observed and the magnetizations do

not change over a long period of time (Fig. 23d,h).

The droplet regime is characterized by a distinct behavior of the oscillation period, T_{osc} , as a function of system size. In Fig. 24a, the oscillation period in 3D is shown as a function of \tilde{J} with a fixed \tilde{K} , for increasing L values. In the non-droplet regime, *i.e.* small \tilde{J} , T_{osc} is independent of system size (note that the period is finite at the critical point \tilde{J}_c , supporting a Hopf-like behavior), while in the droplet-induced swap regime (large \tilde{J}) T_{osc} decreases with system size at intermediate L but converges in the $L \rightarrow \infty$ limit to a finite value, independent of L (see overlap of orange and green lines in Fig. 24a up to $\tilde{J} \approx 2.3$). At larger \tilde{J} values, in a finite system, droplets are so rare that each magnetization flip is driven by a single droplet (here we assume that \tilde{J} is not *too* large, such that the critical droplet size is still smaller than the system size). In this regime, the single droplet can emerge in any lattice position at a given time step, thus T_{osc} scales with L^{-3} [96, 233], see Fig. 24b.

The different oscillation regimes share similarities with the relaxation of the magnetization in an Ising model from an initial state magnetized opposite to the applied field H . Reference [233] identifies four regimes, depending on the field strength and system size. The “strong-field” regime in which “the droplet picture is inappropriate”, and three other regimes which are classified using droplet theory by the relation between three length scales: the critical droplet radius ρ_c , the mean droplet separation ρ_0 , and the linear system size L . These are the multi-droplet regime $L \gg \rho_0 \gg \rho_c$, the single-droplet regime $\rho_0 \gg L \gg \rho_c$, and the “coexistence region” $\rho_0 \gg \rho_c \gg L$ where the system behaves as if there is no applied field. The average metastable lifetime calculated in Ref. [233] is shown to be independent of system size in strong field and multi-droplet regime yet highly dependent on system size in the single-droplet and coexistence regime, in a way reminiscent of Fig. 24a. We note that the analogy drawn here is not perfect because non-reciprocal interactions are different from an externally applied field in that they change once the magnetization flips.

B. The fate of the droplet regime

We now discuss the fate of the droplet-induced swap regime in the thermodynamic limit. In 2D, this regime is destabilized by spiral defects making it disordered, as was shown in Sec. VII.

In 3D, the scenario is more complex. While droplets persist at large system size, distant regions become less synchronized and the system loses its global order. This is illustrated in Fig. 25 which shows snapshots of the θ field, taken from simulations in the droplet-induced swap regime, with different system sizes. In Fig. 25, we see that at system sizes $L = (80, 160, 320)$ there are regions with $n = (2, 3, 4)$ distinct θ -valued (*i.e.* n different colors in the plot), respectively. This decreases the synchroniza-

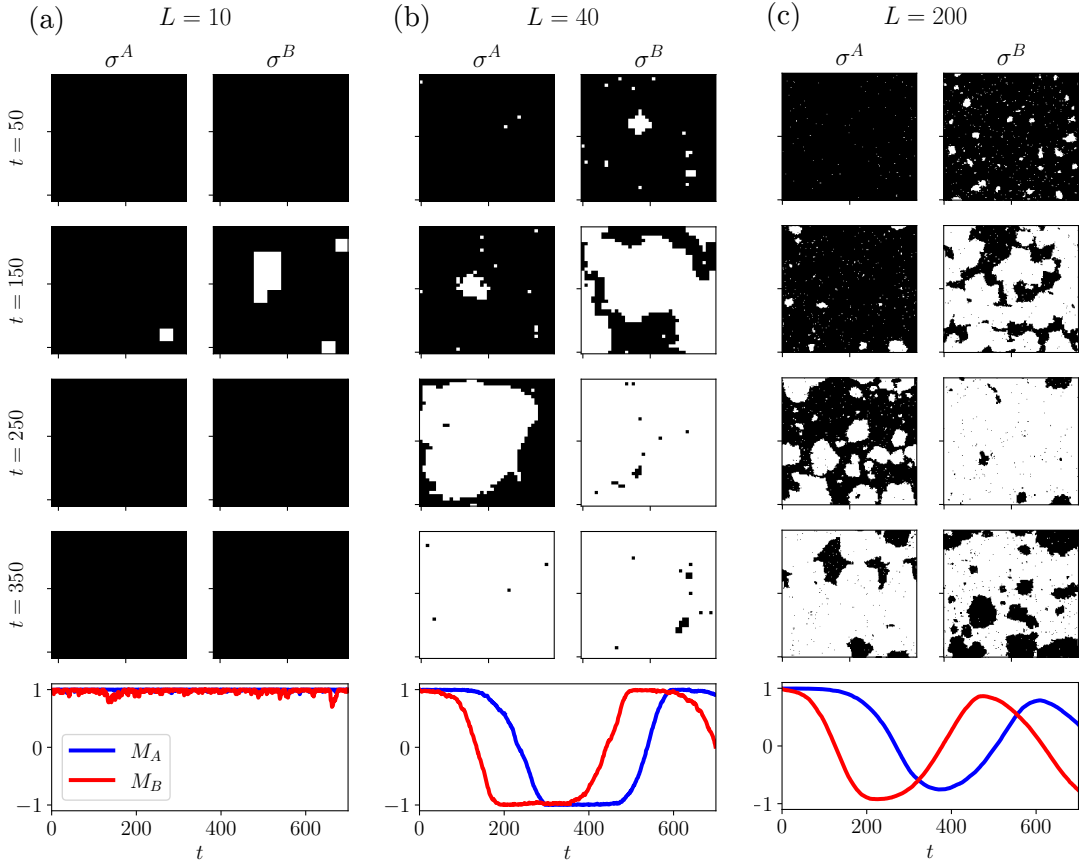


Fig. 21. Instability of the static-order phase in the thermodynamic limit due to droplet nucleation. Top four rows: Snapshots of σ^A and σ^B in a 2D system with linear system size (a) $L = 10$, (b) $L = 40$, (c) $L = 200$. Time evolves from top to bottom. See Movie 4 for the full evolution. Fifth row: the corresponding total magnetizations, M_A and M_B , as a function of time. Obtained from MC simulations with parameters $\tilde{J} = 2.8$ and $\tilde{K} = 0.3$, and with initialization at $t = 0$ with all spins up.

tion. Indeed, the synchronization order parameter, R , is shown to decrease with L , in the right part of Fig. 12a, corresponding to the droplet-induced swap region. While R decreases with system size, it does not converge. Thus, it is unclear to what extent order is lost in the thermodynamic limit, and whether it remains finite or is ultimately deemed disordered ($R = 0$). If the latter is correct, it remains an open question what is the type of phase transition that occurs and where lies the critical line between swap and disorder in this droplet regime.

The decrease in order in the droplet-induced-swap regime causes an intriguing behavior, observed only for large system size, ($L \geq 160$): synchronization is non-monotonic as a function of \tilde{J} (or \tilde{K}). See $L = 320$ line in Fig. 12a, where R increases monotonically with \tilde{J} beyond the Hopf bifurcation until $\tilde{J} \sim 2.05$, and then starts decreasing. It then reaches a local minimum at $\tilde{J} \sim 2.25$ and increases again until saturation at $\tilde{J} \sim 2.55$. A similar behavior is observed in the left part Fig. 18a, for $L = 320$, where R is non-monotonic as a function of \tilde{K} . In both cases the anomalous decrease starts when the swap phase transitions from noisy homogeneous swap to

droplet-induced swap.

The mechanism under which global synchronization decreases with increased \tilde{J} (or decreased \tilde{K}) in the droplet regime is shown in Fig. 26, which compares two simulations with the same $\tilde{K} = 0.3$ value: one at the onset of droplet-induced swap ($\tilde{J} = 2.04$), and the other well within the droplet-induced swap ($\tilde{J} = 2.24$). Simulation snapshots (Figure 26a) reveal that while the system is more correlated over short distances at larger \tilde{J} values, it loses *global order* due to large regions that are out-of-phase with the rest of the system. This can be quantified by a size-dependent synchronization parameter,

$$R(l) \equiv \langle s(l) \rangle \quad \text{with} \quad s(l) \equiv \frac{1}{l^d} \left| \sum_j e^{i\theta_j} \right| \quad (71)$$

where the sum is over all sites inside a box of linear size $l \leq L$, and the average is taken with respect to different boxes and time. The size dependent synchronization parameter is shown in Fig. 26b, for squares instead of cubes to match with the 2D snapshots. For small l , $R(l)$ is larger for the system with the higher \tilde{J} , whereas for

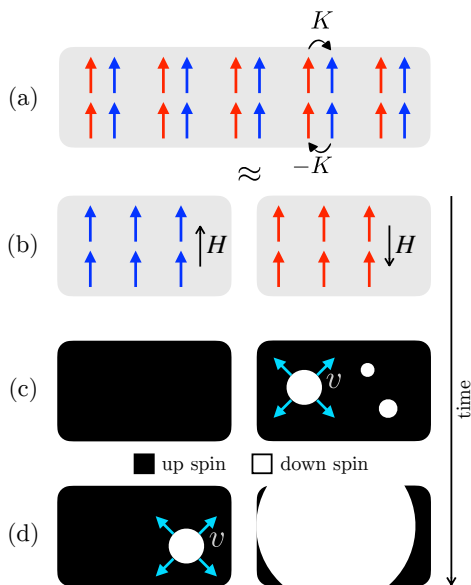


Fig. 22. Droplet argument for the instability of the static-order phase. (a) A system in the static-order phase can be reduced into (b) two equilibrium Ising models subject to magnetic fields, where one system is in a stable equilibrium while the other is in a metastable state. (c) The metastable system nucleates droplets that expand and flip the magnetization. (d) The stable system becomes metastable and nucleates droplets that expand with the same velocity, and so on.

large l , $R(l)$ is larger for the system with the lower \tilde{J} . Moreover, while $R(l)$ at low \tilde{J} decays exponentially with l , in the high \tilde{J} regime it does not and the second derivative of $R(l)$ changes signs. This means that within the droplet-induced swap regime, the system cannot be described by a single correlation length, and instead has multiple length scales related to the droplet parameters such as the critical droplet size, the typical distance between droplets, and the correlation length inside a single droplet.

X. COARSENING DYNAMICS: SCROLL WAVES AND PLANAR WAVES

We now qualitatively discuss the way in which the system coarsens into an ordered state in 3D. In the simulations used to calculate the order parameters R and \mathcal{L} (Figs. 11, 12 and 18), the spins were initialized in an ordered initial condition (all spins up), making the transition to steady state in the swap and static-order phases relatively fast. When fully disordered initial conditions are used (each spin is set to $+1$ or -1 randomly), however, the system can coarsen into long-lived metastable states, before reaching steady state. To show this, we present in Fig. 27a the same plot as Fig. 12a (R vs. \tilde{J} in 3D) but with random initial conditions, and average taken over a single simulation running for a very long

time. In both the swap phase ($1.4 \lesssim \tilde{J} \lesssim 2.3$) and static-order phase ($\tilde{J} \gtrsim 2.3$) we see that for some of the realizations the system reaches the same steady state as with ordered initialization (shown in semi-transparent lines). However, sometimes the measured R is much lower than the one obtained with ordered initialization, suggesting that the system got trapped in a metastable state.

The states in which the system gets trapped in are scroll waves and planar waves, shown in Fig. 27b-d and Movie 3 in both 3D snapshots and 2D-slice snapshots. Here the scroll waves are much less noisy than those discussed in Sec. VIII C.

The planar waves in the nonreciprocal Ising model are analogous to what happens in the equilibrium Ising model, in which the system often reaches stripes or minimal surfaces in the final stages of the coarsening dynamics [234, 235]. Here, however, the stripes move in a particular direction that guarantees, for each site, the $\uparrow\uparrow \rightarrow \uparrow\downarrow \rightarrow \downarrow\downarrow \rightarrow \downarrow\uparrow \rightarrow \uparrow\uparrow$ cycle on average. A planar wave state breaks both time translation symmetry and space translation symmetry (in one direction).

The coarsening dynamics is most easily understood by following the defect filaments of the scroll waves (Fig. 27e). The defects are found using the size-dependent synchronization parameter, $s(l)$, defined in Eq. (71). Note that $s(l)$ is 1 if all the sites in the box are identical, and it is close to zero if the box has a mixture of sites in all four possible states. Thus, we classify defects as sites on the coarse-grained grid in which $s(l)$ is smaller than a threshold s_{\max} . The box size l and the s -threshold are fine-tuned to detect the defect filaments while filtering out noise ($l = 3$ and $s_{\max} = 0.2$ in Fig. 27e).

In the example shown in Fig. 27e, the system coarsens into a complex mixture of defect lines shortly after initialization with disordered initial conditions. After a while, only two defect lines survive. The lines are connected onto themselves by virtue of the periodic boundary conditions, having the topology of rings on a 3-dimensional torus with opposite winding numbers (1 and -1). Thus, they cannot shrink by themselves to a point. Finally, the two filaments collide, forming a new ring with zero winding number that shrinks and disappears. The system then stays in a planar waves state for a very long time. Movie 3 shows another example of the filament dynamics that ends in a defect-free swap phase.

The occurrences in which the system escapes scroll-waves state into swap or static order, without any observation of transitions from the swap or static-order phase into scroll waves, suggest that these are metastable states. This is not the case, however, in the high \tilde{K} limit, where the scroll waves appear to be stable, as explained in Sec. VIII C.

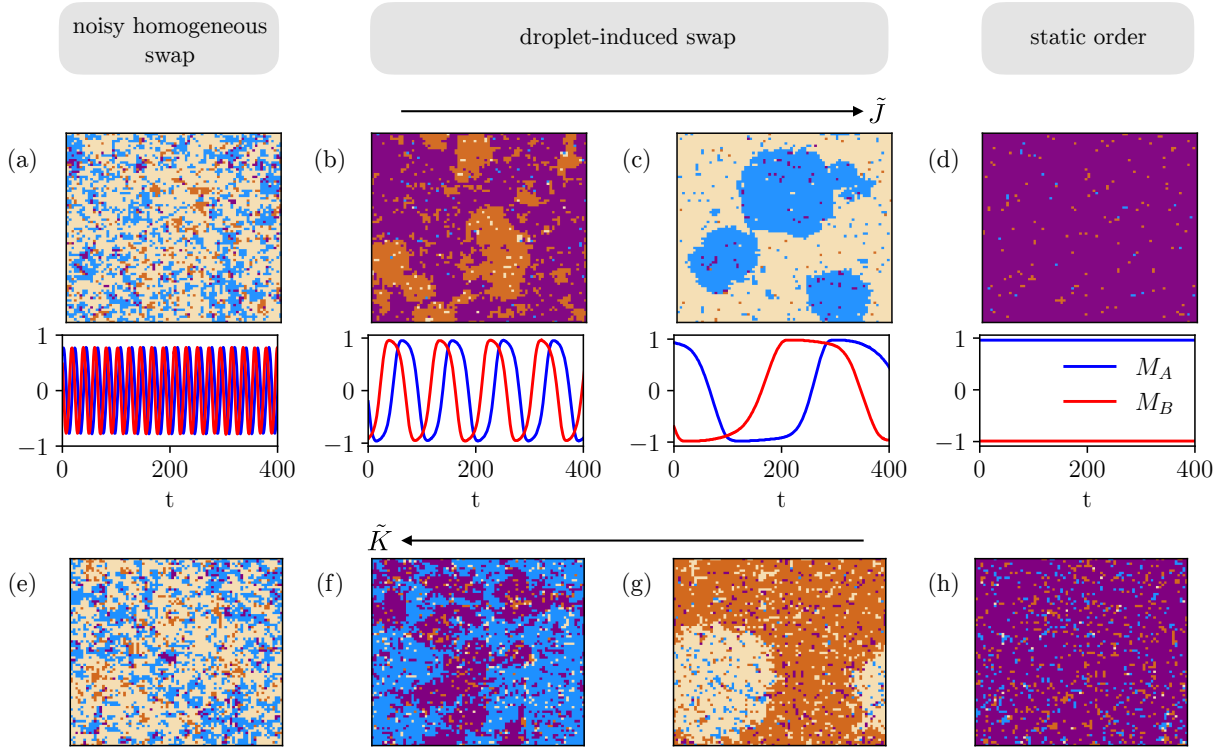


Fig. 23. Transition from swap to static order in a finite 3D system, as a function of \tilde{J} and \tilde{K} . (a-d) Top: 2D-slice snapshots of the θ field, obtained from MC simulations with increasing values of \tilde{J} . Bottom: The corresponding total magnetizations M_A (blue) and M_B (red) as a function of time measured in simulation sweeps. (a) $\tilde{J} = 1.6$. (b) $\tilde{J} = 2.2$. (c) $\tilde{J} = 2.3$. (d) $\tilde{J} = 2.5$, all with $\tilde{K} = 0.3$ and $L = 80$. As \tilde{J} increases, a noisy homogeneous swap phase is replaced by droplet-induced swap and then becomes static and ordered. (e-f) The same as panels a-d (top) but with $\tilde{J} = 1.6$ and decreasing values of \tilde{K} . (e) $\tilde{K} = 0.3$. (f) $\tilde{K} = 0.08$. (g) $\tilde{K} = 0.05$. (h) $\tilde{K} = 0.02$.

XI. SCHEMATIC PHASE DIAGRAM IN THE FULLY ANTI-SYMMETRIC CASE

The results from Secs. VII, VIII, and IX enable us to construct a schematic phase diagram in both 2D and 3D for the fully anti-symmetric case.

In 2D, our numerical results suggest that both the swap phase and the static-order phase are unstable, as long as $K \neq 0$. This leads to the conclusion that there is a single stable phase in the thermodynamic limit: disorder (see Fig. 28a). The same conclusion applies to the 1D case, as is shown in Appendix B.

In 3D (see Fig. 28b), our numerical results suggest that static order is unstable but that the swap phase is stable, with a second-order-like phase transition from disorder to swap featuring 3D XY critical exponents. Regions with high \tilde{J} or \tilde{K} have not been revealed in full: in the large \tilde{J} limit, synchronization decreases, possibly to zero, due to the difficulty of droplet-induced swap to synchronize. In the high \tilde{K} regime, scroll waves completely destabilize the long-range order. Both mechanisms are capable of destroying a large portion of the stable swap phase regime, and there is also a possibility that they would meet in the high \tilde{J} and high \tilde{K} regime, leading to a com-

pact swap phase in (\tilde{J}, \tilde{K}) space rather than an infinite one. Due to the limitations of our simulations, these interesting possibilities lie beyond the scope of this work, which has focused mostly on the low \tilde{J} and \tilde{K} regime, where the swap phase appears to be stable and critical exponents can be calculated.

XII. GENERAL ASYMMETRIC COUPLINGS

In the previous sections, we have focused on the fully anti-symmetric case where $K_+ = 0$ in Eq. (12), for which our model has a C_4 symmetry. In this section, we test whether our results rely on this additional symmetry by considering $K_+ \neq 0$, for which the symmetry is reduced to the diagonal \mathbb{Z}_2 described in Eq. (24).

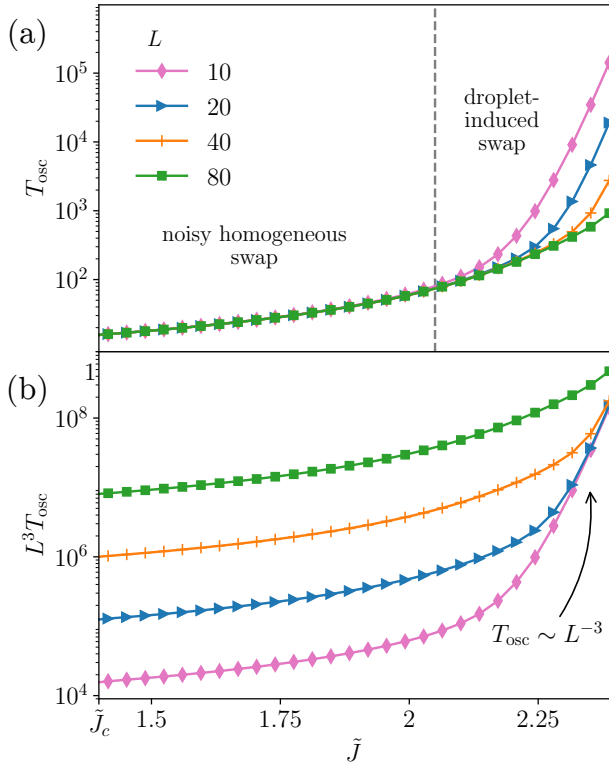


Fig. 24. Behavior of the oscillation period in the 3D swap phase. (a) The oscillation period of the total magnetizations T_{osc} , on a logarithmic scale, as a function of \tilde{J} for fixed $\tilde{K} = 0.3$ and different system sizes. (b) The same with a rescaled oscillation period, $L^3 T_{\text{osc}}$. Dashed grey line in panel a separates a regime in which the oscillations are driven by well-defined droplets (right) from a regime in which they do not (left). \tilde{J}_c marked on the x-axis is the critical point for the disorder-to-swap phase transition. The period is finite at \tilde{J}_c , supporting a Hopf-like behavior. Obtained from MC simulations.

A. Mean-field analysis

Expanding Eq. (23) as was done for the fully anti-symmetric case (Sec. VB), we obtain,

$$\partial_t m_\alpha = -(1 - \tilde{J})m_\alpha + \tilde{K}_{\alpha\beta} m_\beta + D\nabla^2 m_\alpha - \frac{1}{3} (\tilde{J} m_\alpha + \tilde{K}_{\alpha\beta} m_\beta)^3 \quad (72)$$

where $\tilde{K}_{\alpha\beta} \equiv K_{\alpha\beta}/(k_B T)$ and $K_{\alpha\beta}$ is given by Eq. (12). Assuming a spatially homogeneous state, the eigenvalues λ_1 and λ_2 of the Jacobian matrix \mathcal{J} at $m_A = m_B = 0$ are

$$\lambda_{1,2} = -1 + \tilde{J} \pm \sqrt{\tilde{K}_+^2 - \tilde{K}_-^2}. \quad (73)$$

Thus, upon changing \tilde{J} , the possible phases and bifurcations depend on the value of $\tilde{K}_+^2 - \tilde{K}_-^2$. This is demonstrated in Fig. 29, which shows phase portraits of the

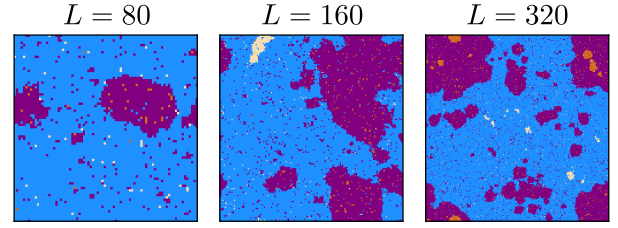


Fig. 25. Loss of synchronization in the droplet regime with increased system size. Snapshots of the θ field (color code in Fig. 2) in 2D slices taken from a 3D MC simulation with $L = 80, 160$, and 320 . Other system parameters are $\tilde{K} = 0.3$ and $\tilde{J} = 2.25$. We see $n = (2, 3, 4)$ distinct θ -valued regions for $L = (80, 160, 320)$, respectively.

spatially homogeneous full mean-field equation, Eq. (23), for different $\tilde{K}_+^2 - \tilde{K}_-^2$ values.

For $\tilde{K}_+^2 - \tilde{K}_-^2 < 0$ (which is equivalent to $\tilde{K}_+ < \tilde{K}_-$ when both \tilde{K}_+ and \tilde{K}_- are assumed to be positive), Fig. 29a, the system is disordered when $\tilde{J} < 1$, and undergoes a Hopf bifurcation at $\tilde{J} = 1$, transitioning from disorder to a limit cycle. Unlike the $K_+ = 0$ case studied throughout most of the paper, here the limit cycle is not rotationally-symmetric even in the $\tilde{J} - 1 \ll 1$ limit. This is seen when writing the spatially homogeneous mean-field equation in polar coordinates,

$$\begin{aligned} \partial_t r &= -\left(1 - \tilde{J} - \tilde{K}_+ \sin(2\theta)\right) r + \mathcal{O}(r^3) \\ \partial_t \theta &= -\tilde{K}_- + \tilde{K}_+ \cos(2\theta) + \mathcal{O}(r^2). \end{aligned} \quad (74)$$

The leading order term in r is θ -dependent, and does not simply scale with $\tilde{J} - 1$. Hence, a separation between the time scales of r and θ cannot be invoked as in Sec. VB. Instead, the limit cycle is elliptical near the Hopf bifurcation [85].

Increasing \tilde{J} leads to additional bifurcations. First, a (\mathbb{Z}_2 -symmetric) SNIC bifurcation where the limit cycle is destroyed by the emergence of two (rather than four for the $K_+ = 0$ case) pairs of stable and saddle points. The stable points that emerge lie in the first and third quadrants of the (m_A, m_B) plane, corresponding to states where the two species are aligned. Then, for even larger values of \tilde{J} , a saddle-node bifurcation occurs where two additional pairs of stable and saddle points emerge, yet static order is maintained. The new stable points lie in the second and fourth quadrants, representing anti-aligned states. This behavior is observed for \tilde{K}_+ and \tilde{K}_- much smaller than 1 (0.1 and 0.2 respectively in the Fig. 29). For larger values, a saddle-node bifurcation can occur such that the ferromagnetic phase coexists with the limit cycle (this scenario is explored in Ref. [151]).

For $0 \leq \tilde{K}_+^2 - \tilde{K}_-^2 < 1$ (Fig. 29b), the system is disordered when $\tilde{J} < 1 - \sqrt{\tilde{K}_+^2 - \tilde{K}_-^2}$ and undergoes a pitchfork bifurcation at $\tilde{J} = 1 - \sqrt{\tilde{K}_+^2 - \tilde{K}_-^2}$ transitioning from disorder to static order with two stable fixed points

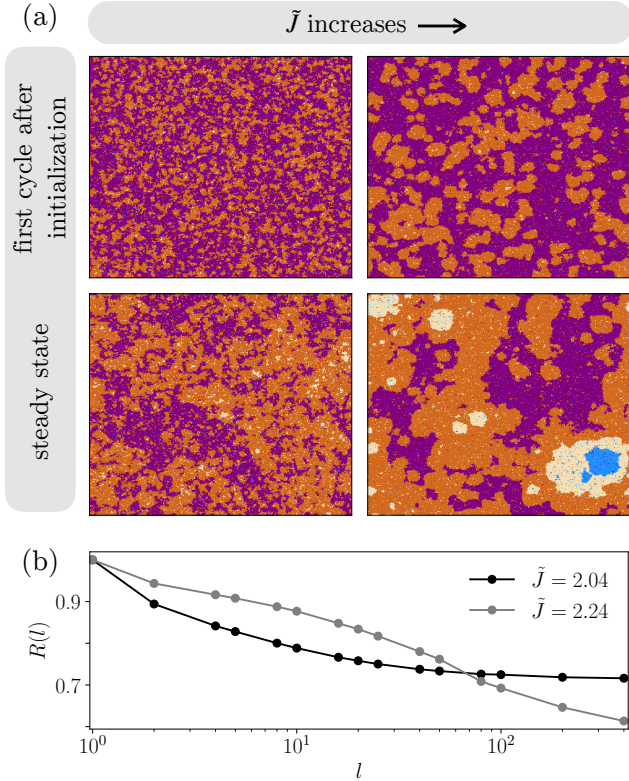


Fig. 26. Decrease in global order in the droplet regime as a function of \tilde{J} . (a) Snapshots of 2D slices taken from a 3D simulation with $\tilde{K} = 0.3$ and $L = 400$, comparing two different \tilde{J} values, $\tilde{J} = 2.04$ (left) and $\tilde{J} = 2.24$ (right). The top snapshots are taken shortly after initialization while the bottom snapshots are taken after 10000 MC sweeps. (b) The synchronization parameter $R(l)$ defined in Eq. (71), measured in steady state as a function of l , for the two \tilde{J} values in panel a. Averages are taken over $(L/l)^2$ squares and 1000 MC sweeps.

of aligned states. In that case, there is no oscillatory phase. When $\tilde{J} = 1 + \sqrt{\tilde{K}_+^2 - \tilde{K}_-^2}$, an additional pitchfork bifurcation occurs where two saddle points emerge from the origin $(0,0)$, which transitions from a saddle to an unstable point. As \tilde{J} increases further, a saddle-node bifurcation occurs where two pairs of anti-aligned stable and saddle points appear. These two additional bifurcations maintain the system in a static-order phase. In the $\tilde{K}_+^2 - \tilde{K}_-^2 > 1$ case (Fig. 29c), the bifurcations are the same as in the $0 \leq \tilde{K}_+^2 - \tilde{K}_-^2 < 1$ case, except that there are already two stable fixed points at $\tilde{J} = 0$. As a result, the system remains in the static-order phase for any value of \tilde{J} (although \tilde{J} must be greater than zero for coarse-graining to take place). The absence of oscillations for $\tilde{K}_+ > \tilde{K}_-$ arises because, despite having nonreciprocal interactions, the two species “agree” on whether they prefer to align or anti-align. This makes a magnetization flip unfavorable for either species.

Figure 30 shows a slice through the three-dimensional

phase diagram (which depends on \tilde{J} , \tilde{K}_+ , and \tilde{K}_-), with \tilde{K}_+ fixed at 0.3. The main difference between this phase diagram and the one in Fig. 4 (which shows the $\tilde{K}_+ = 0$ case) is the pitchfork bifurcation line separating the paramagnetic and ferromagnetic phases in the $\tilde{K}_- \leq \tilde{K}_+$ region, which is just a point in Fig. 4.

B. Swap phase

We perform Monte-Carlo simulations in both 2D and 3D for the general asymmetric case, *i.e.* with the inclusion of reciprocal inter-species interactions. In 2D, we find that the swap phase is unstable, as in the case of fully anti-symmetric interactions (Sec. VII). This is shown in Fig. 31 in which R and \mathcal{L} are plotted as a function of \tilde{J} with fixed \tilde{K}_+ and \tilde{K}_- (a-b) and as a function of \tilde{K}_+ with fixed \tilde{J} and \tilde{K}_- (c-d). In the region in which $\mathcal{L} \neq 0$ (indicating the swap phase), both R and \mathcal{L} decrease with system size. Furthermore, in appendix F we show color maps of R and \mathcal{L} as a function of \tilde{J} and \tilde{K}_- with a fixed non-zero value of \tilde{K}_+ . These color maps show that, similarly to the $\tilde{K}_+ = 0$ case shown in Fig. 9a-d, R and \mathcal{L} diminish as system size increases in the swap regime.

The destabilized phase is shown to be contaminated with defects (inset in Fig. 31), but it does not seem to support spiral waves. This seems to result from the lack of symmetry between the four two-spin states, which is required for the stability of a spiral wave: since A -spins want to align with B -spins more than B -spins wish to anti-align with A spins, $\uparrow\uparrow$ and $\downarrow\downarrow$ states are more favorable than $\uparrow\downarrow$ and $\downarrow\uparrow$, and thus the four “arms” surrounding a defect move at different velocities, destroying the potential spiral configuration. Instead of spirals we observe a complex behavior in which large homogeneous regions of either $\uparrow\uparrow$ or $\downarrow\downarrow$ state continuously move and deform, while defects are rapidly created and annihilated at the boundaries between them.

In 3D, Monte-Carlo simulations suggest that a stable swap phase still exists, even when reciprocal interactions are added. Figure 32 shows color maps of R and \mathcal{L} for a fixed \tilde{K}_+ and $L = 80$. A region with non-zero R and \mathcal{L} , corresponding to a swap phase, is observed. Figure 33 then analyzes a line cut through the color maps for a fixed value of \tilde{K}_- . As \tilde{J} is varied, a continuous phase transition from disorder to swap is observed (at $\tilde{J} \approx 1.45$) and becomes more sharp as L increases. The swap phase is stable for $\tilde{J} \lesssim 1.7$ but destabilizes at higher values, as is discussed next.

To conclude, the instability of the swap phase in 2D and its stability in 3D are not limited to the case of fully anti-symmetric interactions in which $\tilde{K}_+ = 0$, but extends to the general asymmetric case.

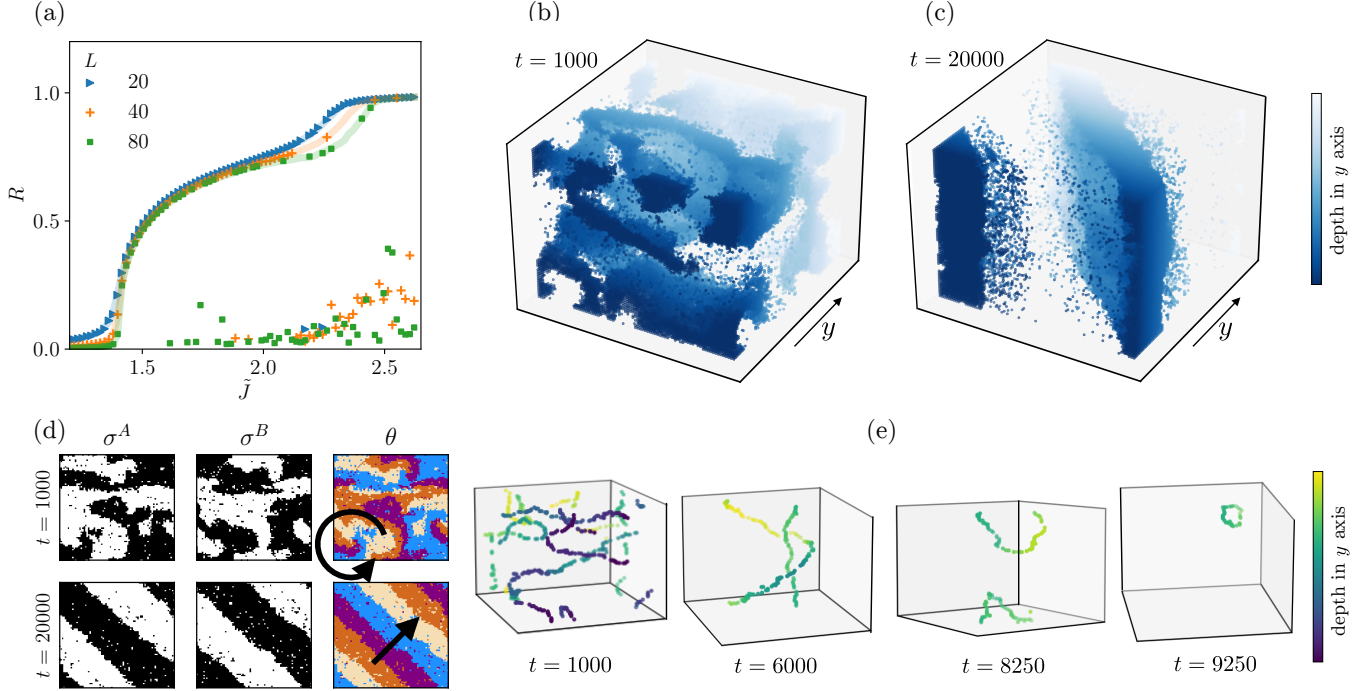


Fig. 27. Random initial conditions lead to long-lived scroll waves and planar waves in 3D. (a) R as a function of \tilde{J} shown for different linear system size L , and for $\tilde{K} = 0.3$. Scattered symbols are measured by averaging over the last 10^5 MC sweeps in a single 10^6 sweeps long simulation, with random initial conditions for the spins. Semi-transparent lines are the results from Fig. 12a in which ordered initial conditions were used and an average was taken over many simulations. (b-e) Analysis of a simulation with random initial conditions and system parameters: $\tilde{J} = 2.28$, $\tilde{K} = 0.3$ and $L = 80$, with an update scheme in which spins are chosen at random. (b-c) 3D images at different times in the evolution, showing scroll waves and planar wave, respectively. Sites in $\uparrow\uparrow$ state are marked in blue while the rest of the sites are not shown. (d) 2D-slice snapshots of the magnetization of A - and B -spins, and of θ , at two different times, showing 2D cuts of the scroll waves (top) and the planar wave (bottom). Black arrows indicate the direction in which the stripes and spiral patterns move over time. (e) Evolution of the defect filaments. As time evolves, the filaments merge, forming rings that shrink and disappear. Note the periodic boundary conditions. Defects are found using the condition $s(l) < s_{\max}$ (Eq. (71)) with $l = 3$ and $s_{\max} = 0.2$.

C. Stability of the static-order phase: a droplet-capture mechanism

While the fate of the swap phase is robust to the addition of reciprocal inter-species interactions, our Monte-Carlo simulations suggest this is not the case for the static-order phase.

First, let us examine the right part of each panel of Fig. 31, showing the transition to static order ($R \neq 0$ and $\mathcal{L} \approx 0$) for a finite-size system in 2D. Figure 31a-b shows that the \tilde{J} -transition-point between the unstable swap regime and static order increases with system size and it is hard to conclude whether static order is stable in the thermodynamic limit. In Fig. 31c-d, where \tilde{K}_+ is varied, R seems to converge to finite non-zero values (while \mathcal{L} approaches zero) for $\tilde{K}_+ \gtrsim 0.24$, which might indicate a stable phase transition from disorder to static order. Surprisingly, the supposed phase transition occurs even though \tilde{K}_+ is lower than \tilde{K}_- ($\tilde{K}_- = 0.3$), which is the case where one species favors alignment while the other favors anti-alignment. In 3D, Fig. 33 gives an even stronger indication that there is a well-defined phase

transition from disorder to static order: for linear system sizes $L = 40, 80, 160$, there is an abrupt transition from a region in which R and \mathcal{L} approach zero (see $1.8 \lesssim \tilde{J} \lesssim 2.2$ in Fig. 33) to a regime in which R is finite and $\mathcal{L} \rightarrow 0$ ($\tilde{J} \gtrsim 2.2$ in Fig. 33), and the transition seems to converge at $\tilde{J} \approx 2.2$. Again, the transition occurs when $\tilde{K}_+ < \tilde{K}_-$ ($\tilde{K}_+ = 0.1$ while $\tilde{K}_- = 0.3$). These indications raise the question: does the droplet destabilization argument sketched in Sec. IX for the fully anti-symmetric case apply here?

Let us assume again a static-order scenario in which both spin species are up on average. The species favoring anti-alignment (B) prefers a state in which all of its spins are flipped. As a result, it will nucleate droplets with opposite magnetization. As in the fully anti-symmetric case, we expect that once these droplets will surpass a critical size, they will expand instead of shrinking. After certain amount of time, the same event will repeat itself for the A species: a critical droplet will nucleate and expand.

However, because of the asymmetry between the two species imposed by K_+ , the critical droplet size ρ_c and

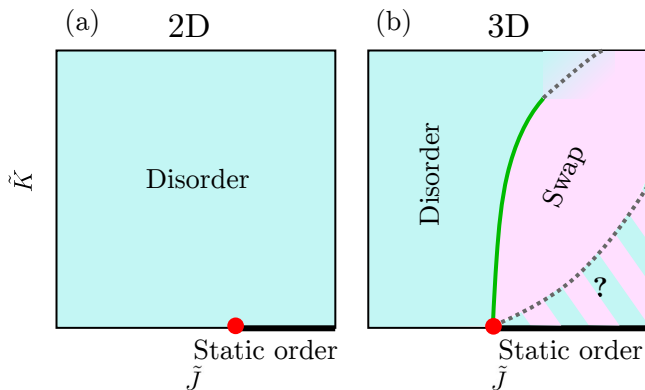


Fig. 28. Schematic phase diagram of the fully anti-symmetric case. (a) Schematic 2D phase diagram and (b) schematic 3D phase diagram. To be compared with the mean-field prediction, Fig. 4. The green line is the second-order-like phase transition with critical exponents compatible with those of the 3D XY model. Grey dashed lines are phase transitions that have not been revealed in full and are possibly first-order-like. In the striped area, it is not clear from numerical simulations whether the system is in the swap or disordered phase.

more importantly the velocity in which droplets expand $v(\rho)$, is different for A -droplets and B -droplets. Here, A -spins interact more strongly with B -spins than the other way around, leading to smaller ρ_c and larger $v(\rho)$ for A -droplets [233]. As a result, a nested A -droplet inside a B -droplet will expand more quickly and may eventually reach the boundaries of the B -droplet. Once this happens, our simulations show that the B -droplet can disintegrate, and the magnetization flip it prevented. Movie 5 shows a 2D simulation in which this mechanism takes place. Snapshots from the simulation are shown in Fig. 34. Note that the simulation parameters were chosen to enhance the visibility of the mechanism, allowing the B -droplet to persist for an extended period, but the mechanism is expected to be more efficient in suppressing droplet growth as the asymmetry between the species increases (larger K_+).

To summarize, when inter-species interactions have opposite signs (the $\tilde{K}_+ < \tilde{K}_-$ case) but are not fully anti-symmetric, there is a competing mechanism that prevents droplets from growing. This suggests a restabilization of the static-order phase in the general asymmetric case, for $d \geq 2$.

D. Absence of infinite-period phase transition

In the fully anti-symmetric case ($K_+ = 0$), there is an oscillating (swap) phase in 3D, but there is no static-order phase. As a consequence, there is no infinite-period phase transition that would correspond to the SNIC bifurcation observed in the mean-field dynamics. A similar situation has been described in Ref. [96]. In the general asym-

metric case, however, both the swap phase and static-order phase exist in 3D. Nevertheless, we did not observe any direct phase transition between the two. Figures 32 and 33 show that the transition between them, when \tilde{K}_+ is fixed and \tilde{J} and \tilde{K} are varied, is mediated by an intermediate disordered region. Unlike the 3D droplet regime with fully anti-symmetric interactions whose fate is left undetermined (Sec. IX B), here the intermediate regime shows convergence to a state with $R = 0$, *i.e.*, disorder. A snapshot of θ of a 2D slice in the intermediate disordered regime is shown in the inset in Fig. 33a. Large regions of aligned spins, either in $\uparrow\uparrow$ or $\downarrow\downarrow$ state, coexist with some defects on the boundaries between them, similar to the 2D disorder discussed in Sec. XII B. In Appendix G, the order parameters on additional cuts through the phase diagram are shown (one with a fixed value of \tilde{J} and another with a fixed value of \tilde{K}_-). These cuts support the same conclusion: the transition between swap to static order we observed is mediated by disorder.

E. Schematic phase diagram in the general asymmetric case

A schematic drawing of the 2D and 3D phase diagram with a fixed non-zero \tilde{K}_+ is shown in Fig. 35. In 2D, our numerical results suggest that there are stable disorder and static-order phases (but no swap), while in 3D, our numerical results suggest that all the phases predicted by mean-field: disorder, swap, and static order, are stable. We expect the disorder-to-swap phase transition to be characterized by the same critical exponents as in Sec. VIII A (compatible with 3D XY), at least throughout a portion of the phase transition line. Other portions may be described by first-order-like phase transitions. Similarly, we hypothesize that the phase transition from disorder to static order in both 2D and 3D has Ising critical exponents in the regime where $K_+ > K_-$, but might be first-order-like in the opposite $K_+ < K_-$ regime (see Fig. 32a in which the $K_+ < K_-$ phase transition seems more abrupt than the $K_+ > K_-$ phase transition). Finally, we cannot exclude that the three phases in 3D meet at a tricritical point (or line in the three-dimensional phase diagram).

XIII. CONCLUSIONS

We introduced a nonreciprocal Ising model as a minimal model for nonreciprocal many-body dynamics, and studied the stability of its static and time-dependent phases along with the transitions between them. Our main result is the stability of a time-dependent (swap) phase in 3D, which behaves as a time-crystal with infinite coherence time in the thermodynamic limit. The phase transition from disorder to swap is characterized by critical exponents compatible with the 3D XY model, which can be rationalized by the breaking of a continu-

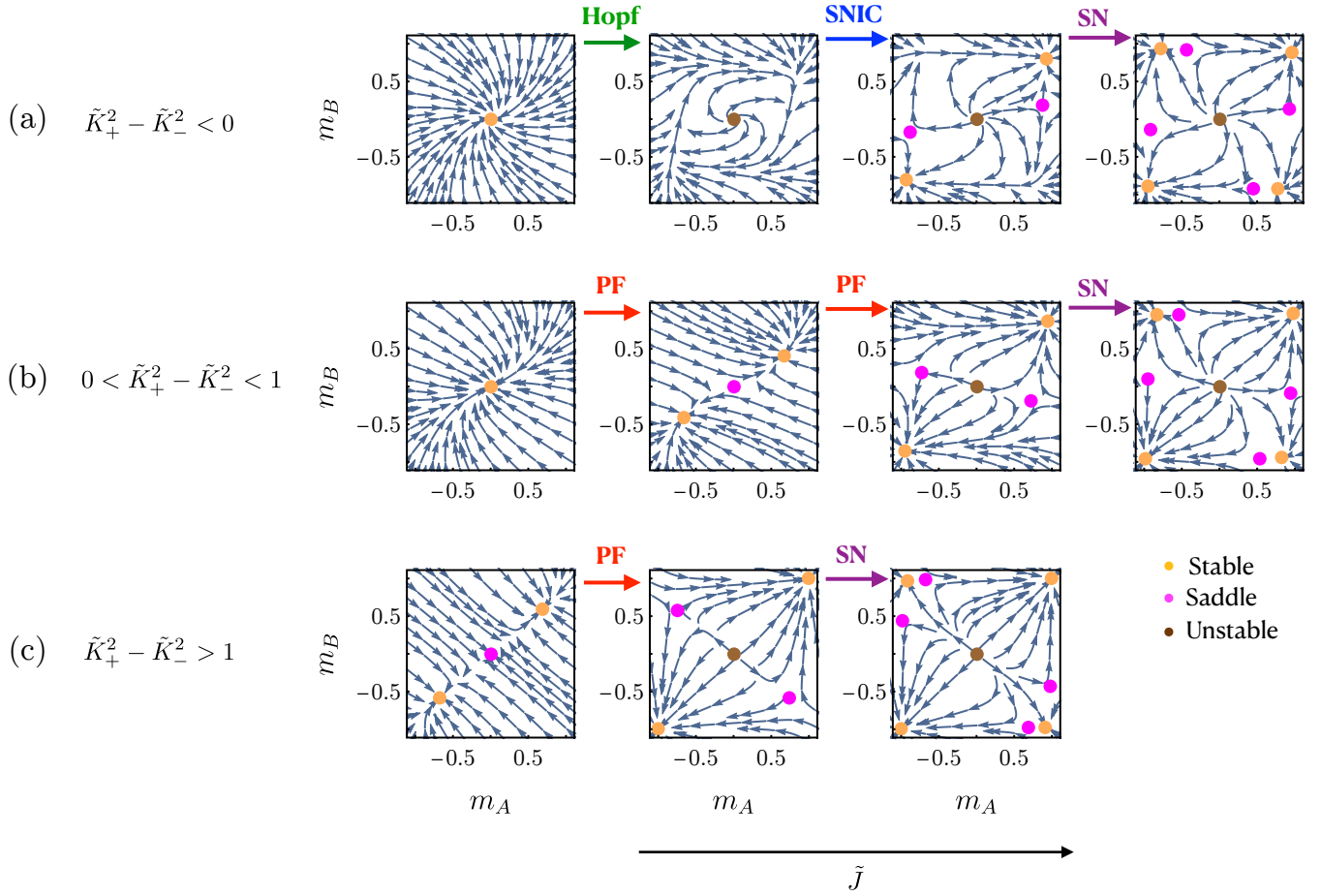


Fig. 29. Bifurcations in the general asymmetric case. Flow in (m_A, m_B) space calculated from the spatially homogeneous full mean-field equation, Eq. (23), for $\tilde{K}_- = 0.2$, and (a) $\tilde{K}_+ = 0.1$, (b) $\tilde{K}_+ = 0.3$, and (c) $\tilde{K}_+ = 1.1$. In each panel, \tilde{J} is increased from left to right to capture the different phase portraits. In (a) $\tilde{J} = 0.4, 1.2, 1.5, 1.7$, in (b) $\tilde{J} = 0.4, 0.9, 1.4, 2$ and in (c) $\tilde{J} = 0.1, 2.3, 3.1$. The arrows mark the bifurcations that connect every two configurations: Hopf, saddle-node on an invariant circle (SNIC), saddle-node (SN) or pitchfork (PF).

ous symmetry (time translation) in the swap phase. The existence of a swap phase in 3D is robust and holds for fully anti-symmetric interactions between the species as well as the more general asymmetric interactions case.

Based on simulations and theoretical arguments, we predict that the static-order (ferromagnetic) phase is unstable in any finite dimension for fully anti-symmetric interactions. The instability is caused by the expansion of droplets of opposite magnetization occurring in the metastable species. When the inter-species interaction is not fully anti-symmetric, a competing mechanism of droplet-capture by the other species can re-stabilize the static-order phase. A direct phase transition between a time-dependent phase and a static-ordered phase, however, was not observed.

Code availability — The code used for performing the Monte-Carlo simulations, computing the critical exponents, and plotting the mean-field phase portrait is available under the 2-clause BSD license at <https://doi.org/10.5281/zenodo.14816551>

ACKNOWLEDGMENTS

We thank G. Biroli, S. Diehl, O. Granek, M. Han, T. Khain, P. Littlewood, R. Mandal, D. Mukamel, S. Sethi, S. Sondhi, G. A. Weiderpass, C. Weiss, and T. Witten for helpful discussions. Y.A., D.S. and M.F. acknowledge support from a MRSEC-funded Kadanoff–Rice fellowship and the University of Chicago Materials Research Science and Engineering Center, which is funded by the National Science Foundation under award no. DMR-2011854. Y.A. acknowledges support from the Zuckerman STEM Leadership Program. D.M., M.F., and V.V. acknowledge support from the France Chicago center through a FACCTS grant. M.F. acknowledges support from the National Science Foundation under grant no. DMR-2118415 and the Simons Foundation. V.V. acknowledges partial support from the Army Research Office under grant nos. W911NF-22-2-0109 and W911NF-23-1-0212 and the Theory in Biology program of the Chan Zuckerberg Initiative. This research was partly

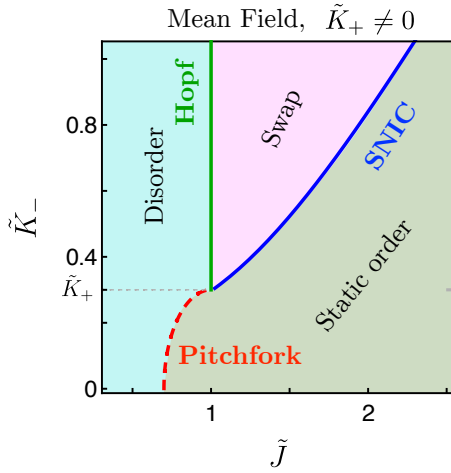


Fig. 30. Mean-field phase diagram of the general asymmetric case. The diagram is shown as a function of \tilde{J} and \tilde{K}_- , with the reciprocal inter-species interaction coupling set to $\tilde{K}_+ = 0.3$. The saddle-node bifurcations illustrated in Fig. 29 are not drawn in this plot. Obtained from numerical analysis of the spatially homogeneous Eq. (23).

supported by the National Science Foundation through the Center for Living Systems (grant no. 2317138) and the National Institute for Theory and Mathematics in Biology (NITMB). All the authors acknowledge the support of the UChicago Research Computing Center which provided the computing resources for this work.

Appendix A: Measurements of time-reversal symmetry breaking

As shown in Sec. IV B, nonreciprocal coupling breaks detailed balance, and therefore time-reversal symmetry. This is a statement about the dynamics of our system. The dynamics can be related to thermodynamic observables – such as heat, work, and entropy – under the *local detailed balance* condition [156–158, 236–238]. As we don’t explicitly model the environment of our system, the local detailed balance condition is a hypothesis. Specifically, local detailed balance relates the entropy produced by a state transition (here, a spin flip) to the transition rates $w(F_i^\alpha \vec{\sigma} | \vec{\sigma})$ via

$$\Delta S_{\text{single flip}} = \ln \frac{w(F_i^\alpha \vec{\sigma} | \vec{\sigma})}{w(\vec{\sigma} | F_i^\alpha \vec{\sigma})}. \quad (\text{A1})$$

Here entropy is given in units of k_B . By summing over a series of transitions in a specified trajectory, the above expression gives the total entropy produced by that trajectory. For example, Eq. (17) gives the entropy produced by a specific cycle of spin states.

To characterize the steady states of the system, it is more convenient to measure the average entropy production rate. This is given by (see §6.2.2 of [156] for deriva-

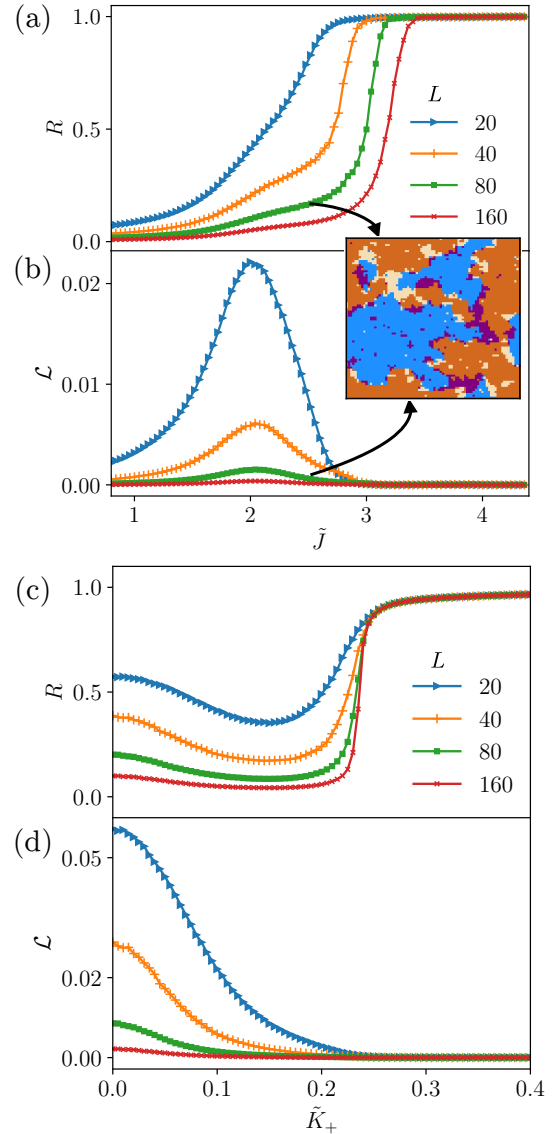


Fig. 31. No stable swap phase in 2D in the general asymmetric case. (a) R and (b) \mathcal{L} as a function of \tilde{J} for $\tilde{K}_+ = 0.1$ and $\tilde{K}_- = 0.3$ shown for different linear system size L . Inset: Snapshot of the θ field (taken after steady state is reached) in a simulation with $\tilde{J} = 2.5$ and $L = 80$, and the same \tilde{K}_+ and \tilde{K}_- as the main plots. The snapshot reveals defects with blue and brown regions ($\uparrow\uparrow$ and $\downarrow\downarrow$, respectively), being more abundant than yellow and purple regions ($\downarrow\uparrow$ and $\uparrow\downarrow$, respectively). (c) R and (d) \mathcal{L} as a function of \tilde{K}_+ for $\tilde{J} = 2$ and $\tilde{K}_- = 0.3$ and for different system sizes. Obtained from MC simulations.

tion)

$$\dot{S} = \sum_{i,\alpha} \left\langle w(F_i^\alpha \vec{\sigma} | \vec{\sigma}) \ln \frac{w(F_i^\alpha \vec{\sigma} | \vec{\sigma})}{w(\vec{\sigma} | F_i^\alpha \vec{\sigma})} \right\rangle_{t,\Omega}, \quad (\text{A2})$$

where $\langle \dots \rangle_{t,\Omega}$ is an average over time and realizations. Using the Glauber transition rate, Eq. (8), we obtain

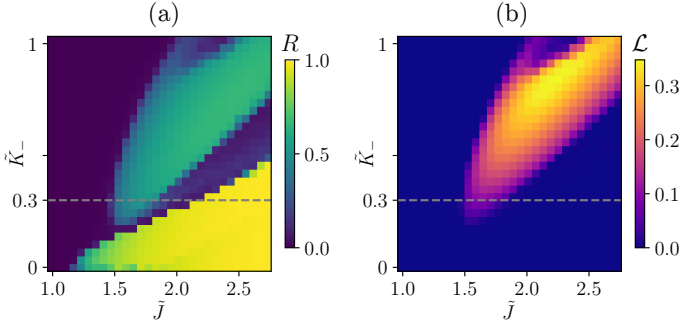


Fig. 32. Order parameters in 3D in the general asymmetric case. (a) R and (b) \mathcal{L} color map as a function of \tilde{J} and \tilde{K}_- with $\tilde{K}_+ = 0.1$ and $L = 80$. Dashed grey lines show the fixed \tilde{K}_- cut analyzed in Fig. 33. Obtained from MC simulations.

that the entropy production rate per spin is

$$\dot{s} = -\frac{1}{L^d} \sum_{i,\alpha} \left\langle \left[1 - \tanh \left(\frac{\Delta E_i^\alpha}{2k_B T} \right) \right] \frac{\Delta E_i^\alpha}{2k_B T} \right\rangle_{t,\Omega}. \quad (\text{A3})$$

where τ was taken as 1 in simulation time.

The entropy production rate in Eq. (A3) is a microscopic measurement of time-reversal symmetry breaking. By contrast, the phase space angular momentum $\mathcal{L} = \langle M_B \partial_t M_A - M_A \partial_t M_B \rangle_{t,\Omega}$ introduced in Eq. (51) of the main text is a *macroscopic* measurement of time-reversal symmetry breaking. Coarse-graining from micro- to macroscopic variables is known to give a lower bound to the true entropy production rate [156], below we will show that \mathcal{L} is proportional to the coarse-grained (mesoscopic) entropy production rate, denoted by $\dot{\mathcal{S}}$, only for cases where the fluctuations in magnetization are negligible compared with the average magnetization and if one considers the dynamics of the mean-field equation with added noise in the $m_\alpha \ll 1$ limit.

To see this, we work with the mean-field equation of the fully anti-symmetric case expanded around $m_\alpha \ll 1$, Eq. (30), as a stochastic PDE with white noise,

$$\begin{aligned} \partial_t m_\alpha &= - (1 - \tilde{J}) m_\alpha + \tilde{K} \varepsilon_{\alpha\beta} m_\beta + D \nabla^2 m_\alpha \\ &\quad - \frac{1}{3} \left(\tilde{J} m_\alpha + \tilde{K} \varepsilon_{\alpha\beta} m_\beta \right)^3 + \eta_\alpha. \end{aligned} \quad (\text{A4})$$

where the white noise field satisfies $\langle \eta_\alpha(\vec{r}, t) \rangle = 0$ and $\langle \eta_\alpha(\vec{r}, t) \eta_\beta(\vec{r}', t') \rangle = \zeta \delta_{\alpha\beta} \delta(\vec{r} - \vec{r}') \delta(t - t')$. This can be rewritten as

$$\partial_t m_\alpha = -\frac{\delta \mathcal{F}}{\delta m_\alpha} + A_\alpha + \eta_\alpha, \quad (\text{A5})$$

where $-\delta \mathcal{F} / \delta m_\alpha$ are conservative forces derived by the variation of a free energy

$$\begin{aligned} \mathcal{F} &= \int d\vec{r} \left[\frac{(1 - \tilde{J})}{2} (m_A^2 + m_B^2) + \frac{\tilde{J}^3}{12} (m_A^4 + m_B^4) \right. \\ &\quad \left. + \frac{1}{2} \tilde{J} \tilde{K}^2 m_A^2 m_B^2 + \frac{D}{2} (|\nabla m_A|^2 + |\nabla m_B|^2) \right], \end{aligned}$$

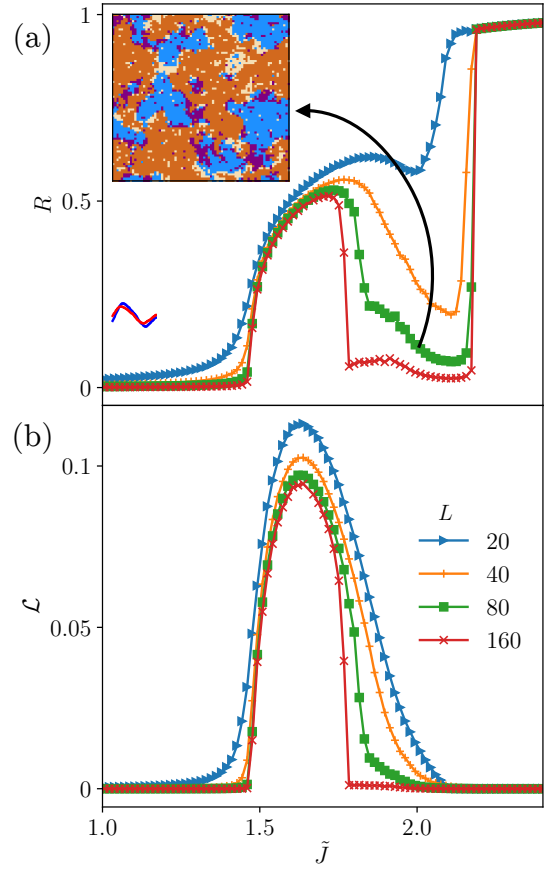


Fig. 33. Phase transition from disorder to swap in 3D in the general asymmetric case. (a) R and (b) \mathcal{L} as a function of \tilde{J} with $\tilde{K}_+ = 0.1$ and $\tilde{K}_- = 0.3$, for different system sizes. The inset in panel (a) shows a snapshot of θ in a 2D slice of the 3D system (taken after steady state is reached), with $\tilde{J} = 2$, $L = 80$, and the same \tilde{K}_+ and \tilde{K}_- values as in the main panel. Obtained from MC simulations.

and A_α are the non-conservative forces on the right-hand side of Eq. (A4),

$$A_\alpha = \sum_\beta \varepsilon_{\alpha\beta} a_{\alpha\beta} \quad (\text{A6})$$

$$a_{\alpha\beta} = \tilde{K} m_\beta - \tilde{J}^2 \tilde{K} m_\alpha^2 m_\beta - \frac{1}{3} \tilde{K}^3 m_\beta^3. \quad (\text{A7})$$

Finally, we introduce the path probability functional of observing a trajectory $\mathbf{m}(\vec{r}, t)$ as

$$\mathcal{P}[\mathbf{m}(\vec{r}, t)] = \frac{\exp(-\mathcal{A}[\mathbf{m}(\vec{r}, t)])}{\mathcal{Z}}, \quad (\text{A8})$$

where $\mathbf{m} \equiv (m_A, m_B)$, \mathcal{Z} is a normalization constant, and $\mathcal{A}[\mathbf{m}(\vec{r}, t)]$ is the action, which can be found using path-integral techniques [229, 239–242] to be

$$\mathcal{A}[\mathbf{m}(\vec{r}, t)] = \frac{1}{\zeta} \int d\vec{r} dt \sum_\alpha \left(\partial_t m_\alpha + \frac{\delta \mathcal{F}}{\delta m_\alpha} - A_\alpha \right)^2. \quad (\text{A9})$$

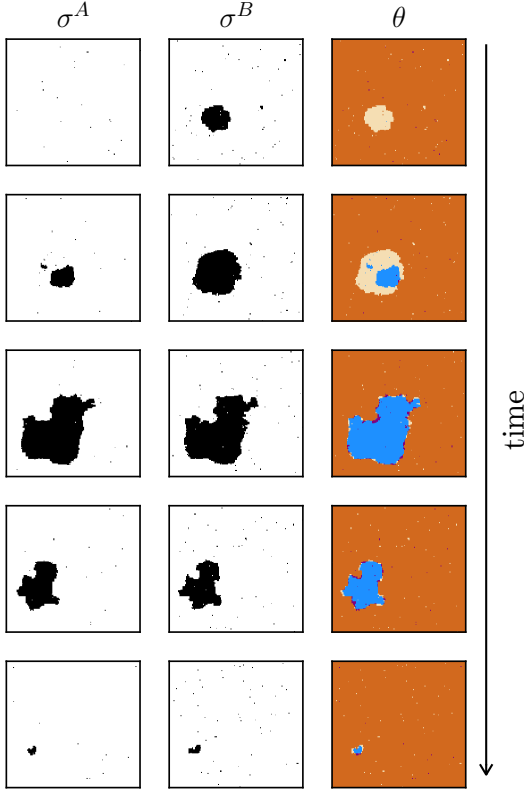


Fig. 34. Droplet capture mechanism. MC simulation snapshots of a 2D system with $\tilde{J} = 3.3$, $\tilde{K}_+ = 0.1$, $\tilde{K}_- = 0.3$, and $L = 150$. See Movie 5 for the full evolution. Each row displays a distinct time step, with time ascending from top to bottom. Species B nucleates a droplet, but before it reaches system size, a nested droplet of A -spins nucleates and expands at faster speed, eventually catching up with the boundaries of the B -droplet, making it shrink and disappear. This mechanism can stabilize the static-order phase when $\tilde{K}_+ < \tilde{K}_-$.

The average entropy production rate for a trajectory is written in terms of \mathcal{P} and of the probability $\tilde{\mathcal{P}}$ of observing the trajectory under time-reversal as [243]

$$\dot{S} = \lim_{T \rightarrow \infty} \frac{1}{T} \left\langle \ln \frac{\mathcal{P}}{\tilde{\mathcal{P}}} \right\rangle_{\Omega} = \lim_{T \rightarrow \infty} \frac{\langle \tilde{\mathcal{A}} - \mathcal{A} \rangle_{\Omega}}{T} \quad (\text{A10})$$

where T here is the trajectory duration and the average is over noise realizations [244]. As we do not have magnetic forces, finding $\tilde{\mathcal{A}}$ amounts to taking $t \rightarrow -t$, which only affects the time derivative terms in Eq. (A9), giving

$$\tilde{\mathcal{A}}[\mathbf{m}(\vec{r}, t)] = \frac{1}{\zeta} \int d\vec{r} dt \sum_{\alpha} \left(-\partial_t m_{\alpha} + \frac{\delta \mathcal{F}}{\delta m_{\alpha}} - A_{\alpha} \right)^2. \quad (\text{A11})$$

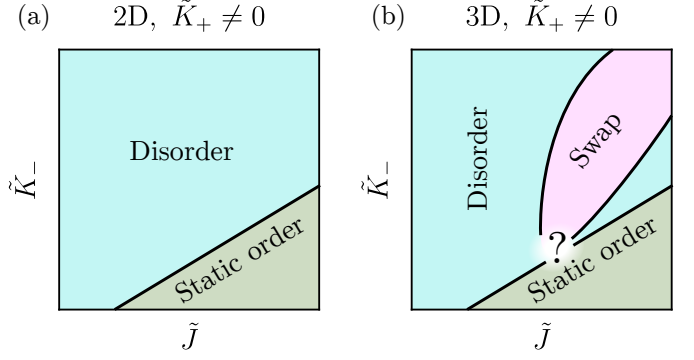


Fig. 35. Schematic phase diagram of the general asymmetric case in (a) 2D and (b) 3D, shown as a function of \tilde{J} and \tilde{K}_- , with fixed (non-zero) \tilde{K}_+ . The nature of the phase transition lines are left unspecified, see discussion in Sec. XIII E. The question mark represents the uncertainty regarding whether the swap and static-order phases meet at a point or are strictly separated by disorder.

Plugging Eqs. (A9) and (A11) into Eq. (A10), we find

$$\begin{aligned} \dot{S} &= \lim_{T \rightarrow \infty} \frac{4}{\zeta T} \left\langle \int d\vec{r} dt \sum_{\alpha} \left(A_{\alpha} - \frac{\delta \mathcal{F}}{\delta m_{\alpha}} \right) \partial_t m_{\alpha} \right\rangle_{\Omega} \\ &= \lim_{T \rightarrow \infty} \frac{4}{\zeta T} \left\langle \int d\vec{r} dt \sum_{\alpha} (A_{\alpha} \partial_t m_{\alpha}) - \Delta \mathcal{F} \right\rangle_{\Omega} \\ &= \lim_{T \rightarrow \infty} \frac{4}{\zeta T} \left\langle \int d\vec{r} dt \sum_{\alpha} A_{\alpha} \partial_t m_{\alpha} \right\rangle_{\Omega} \\ &= \lim_{t \rightarrow \infty} \frac{4}{\zeta T} \left\langle \int d\vec{r} dt (a_{AB} \partial_t m_A - a_{BA} \partial_t m_B) \right\rangle_{\Omega} \\ &= \frac{4}{\zeta} \int d\vec{r} \langle a_{AB} \partial_t m_A - a_{BA} \partial_t m_B \rangle_{t, \Omega}. \end{aligned} \quad (\text{A12})$$

To go from the first to second line, we identified the total time derivative of the free energy, $d\mathcal{F}/dt = \int d\vec{r} \sum_{\alpha} \partial_t m_{\alpha} (\delta \mathcal{F} / \delta m_{\alpha})$. To go from the second to the third line, we used the fact that the $\Delta \mathcal{F}$ is a constant, which will contribute zero to \dot{S} when the limit $T \rightarrow \infty$ is taken. In the last equality we replaced $\frac{1}{T} \int dt \dots$ with a time average $\langle \dots \rangle_t$. For small m_{α} , non-linear terms can be dropped and $a_{\alpha\beta} \simeq \tilde{K} m_{\beta}$, leading to

$$\dot{S} = \frac{4\tilde{K}}{\zeta} \int d\vec{r} \langle m_B \partial_t m_A - m_A \partial_t m_B \rangle_{t, \Omega}. \quad (\text{A13})$$

Finally, we assume small fluctuations around the mean magnetization, *i.e.* $m_{\alpha}(\vec{r}) = M_{\alpha} + \delta m_{\alpha}(\vec{r})$, $\delta m_{\alpha}(\vec{r}) \ll M_{\alpha}$, and obtain to leading order,

$$\dot{S} = \frac{4\tilde{K}L^d}{\zeta} \langle M_B \partial_t M_A - M_A \partial_t M_B \rangle_{t, \Omega} = \frac{4\tilde{K}L^d}{\zeta} \mathcal{L}. \quad (\text{A14})$$

In conclusion, $\mathcal{L} \propto \dot{S}$ for a mesoscale system obeying Eq. (A4) if (i) $|m_{\alpha}| \ll 1$ and (ii) $\delta m_{\alpha}(\vec{r}) \ll M_{\alpha}$. Under these two approximations, and in the vicinity of the

Hopf bifurcation, Eq. (A4) can be reduced into the noisy Stuart-Landau equation [85]

$$\frac{d\mathcal{M}}{dt} = (a - b|\mathcal{M}|^2)\mathcal{M} + H \quad (\text{A15})$$

where $\mathcal{M} = M_A + iM_B$, $H = \eta_A + i\eta_B$, and a and b are complex coefficients. Writing the Stuart-Landau equation in polar coordinates and eliminating the radial equation yields a drift-diffusion equation that saturates the bound on the entropy production per oscillation $\Delta S \geq 4\pi^2\mathcal{N}$ of Ref. [131] mentioned in Sec. VIII B (here, $\mathcal{N} \equiv \tau_c/T_{\text{osc}}$ where τ_c is the coherence time and T_{osc} is the period of oscillation). Indeed, it is shown in Ref. [245, SM § III] that in this case, the rate of entropy production is $\dot{S} = f^2\tau_c$ in which $f = 2\pi/T_{\text{osc}}$, and $\Delta S = T_{\text{osc}}\dot{S}$ saturates the bound. We refer to Ref. [245] for more details.

While \mathcal{L} can be measured in any state, in general one will have $\mathcal{L} \neq \dot{S}$, and no conclusion about entropy production in terms of phase space angular momentum can be made.

We calculate the entropy production rate per spin in the 3D NR Ising model using MC simulations. Figure 36 shows \dot{s} for $L = 40$ and $L = 80$, as a function of the coupling \tilde{J} . The curves overlap, which shows that \dot{s} is independent of system size for large systems. \dot{s} decreases monotonically with \tilde{J} , as stronger nearest-neighbor coupling slows down the cycle rate of individual spin-pairs. By contrast, \mathcal{L} is non-zero only in the swap phase. For $\tilde{J} = 1.6$ and $\tilde{K} = 0.1$, we compare \dot{s} to the lower-bound given by the temporal autocorrelation function in Eq. (67), where T_{osc} is found by measuring the average oscillation time and τ_c is given by the fit in Fig. 17. Indeed, \dot{s} exceeds the lower bound by a factor of about 10.

Appendix B: 1D NR Ising model

We simulate the one-dimensional NR Ising model, with fully anti-symmetric interactions, using random picking Glauber dynamics as in the 2D simulations (see Sec. VI). The order parameters R and \mathcal{L} as a function of \tilde{J} and for fixed \tilde{K} are shown in Fig. 37a and Fig. 37b, respectively, while kymographs of θ with different \tilde{J} and \tilde{K} values are shown in Fig. 37c.

The 1D NR Ising model does not have a phase transition to an ordered state (either static or time dependent), as is evident from the decrease of R and \mathcal{L} as system size increases. Similarly to the 1D Ising model, as L increases, domains of opposite magnetization emerge and the system becomes disordered. However, unlike the Ising model, the boundaries between the domains do not diffuse but move with non-zero velocity (see Fig. 37c where the kymograph slope indicates the velocity). Domains expand in a way that can be viewed as the 1D version of droplet growth discussed in Sec. IX.

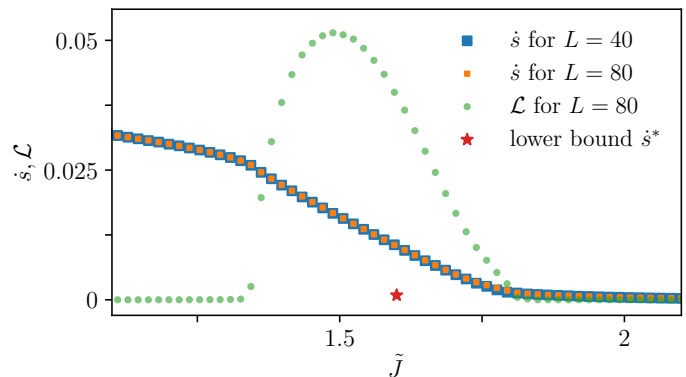


Fig. 36. Measurements of time-reversal symmetry breaking in the 3D NR Ising model. Entropy production rate per spin, \dot{s} (blue and orange squares, calculated from Eq. (A3)), and phase space angular momentum, \mathcal{L} (green dots), as a function of \tilde{J} for fixed $\tilde{K} = 0.1$. Theoretical lower bound for \dot{s} , $\dot{s}^* = \frac{4\pi^2}{T_{\text{osc}}^2} \frac{\tau_c(L)}{L^d}$ (Eq. (67)), at $\tilde{J} = 1.6$, is shown as a red star, where T_{osc} was measured to be $T_{\text{osc}} = 120$ and τ_c/L^3 was taken as 0.32 in accordance with the fit in Fig. 17. $\dot{s}^* = 9 \times 10^{-4}$ while $\dot{s} = 0.01$ at $\tilde{J} = 1.6$.

Appendix C: The effect of different update rules

Out of equilibrium, different update rules may change the steady state of the system. To study this effect in the NR Ising model, we performed simulations with random sequential updates, checkerboard updates [173], and synchronous updates (in which all the spins are updated at the same time) [246]. Additionally, we used the Metropolis algorithm [186] and compared it to the Glauber which was used throughout the paper.

For fixed coupling parameters (\tilde{J} and \tilde{K}), the different update rules changed the dynamics in steady state. However, they did not lead to qualitative changes in the phase diagram. That way, the critical point \tilde{J}_c , for some fixed \tilde{K} , is altered, but not the existence / destabilization of a phase transition. As an example, we show in Fig. 38 that the phase transition from disorder to swap in 3D, as characterized by the variation of the order parameter R as a function of \tilde{J} , is qualitatively the same when using random sequential updates (standard Glauber algorithm), as it is with the checkerboard algorithm, which was used to produce Fig. 12a.

We did not find any qualitative difference related to phase transitions. The only notable difference is that with synchronous updates, fluctuations were considerably larger due to “checkerboard patterns” (small regions in which each spin is anti-aligned with its same-species neighbors) that frequently appeared and then disappeared.

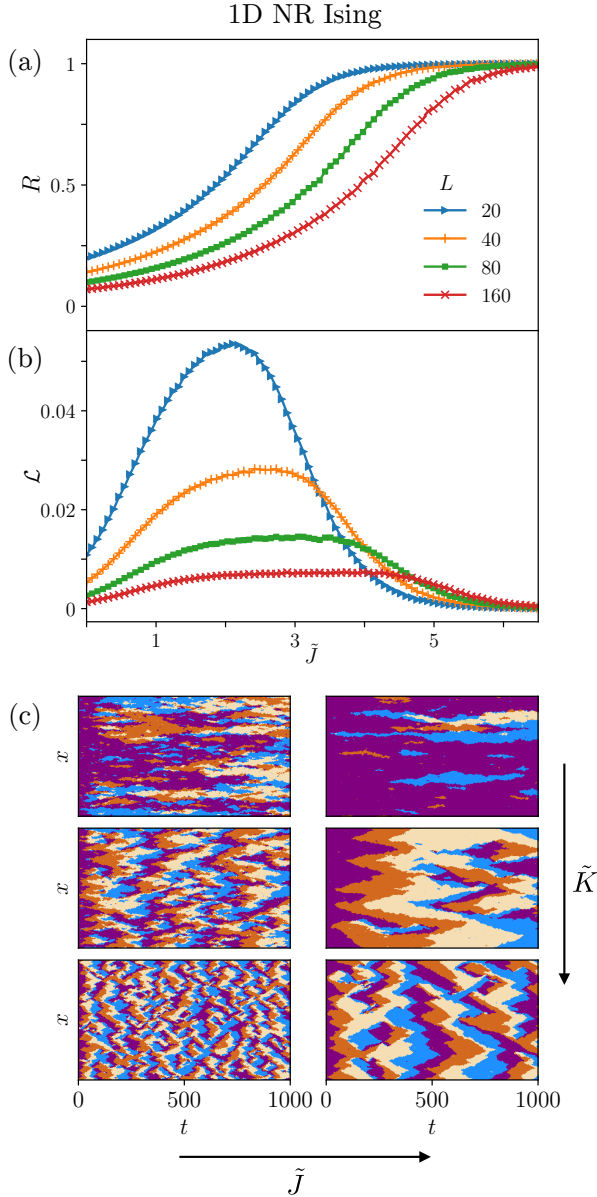


Fig. 37. 1D NR Ising model. (a) R and (b) \mathcal{L} as a function of \tilde{J} for $\tilde{K} = 0.3$ and different linear system size L . (c) Kymographs of θ for $\tilde{J} = 3$ (left) and $\tilde{J} = 4$ (right), comparing the Ising model ($\tilde{K} = 0$, top) with the NR Ising model ($\tilde{K} = 0.2$, middle and $\tilde{K} = 0.5$, bottom). System size is $L = 500$. Obtained from MC simulations.

Appendix D: Simulations of the mean-field equation in 2D

We simulate the full mean-field equation on a grid (Eq. (21)) in 2D in the fully anti-symmetric case and in the regime corresponding to a stable swap phase (see Fig. 4). Results are shown in Fig. 39. Depending on initial conditions, the system can end up in different states. An initially ordered state leads to a stable swap phase

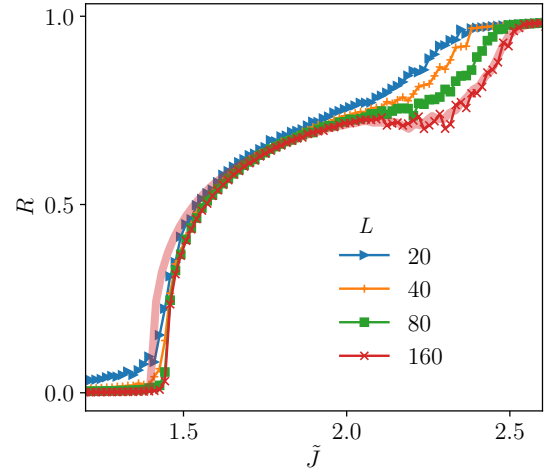


Fig. 38. Qualitative agreement between two Monte-Carlo update rules. R as a function of \tilde{J} for $\tilde{K} = 0.3$ and different linear system size L , calculated from MC simulations with random spin update rule instead of the checkerboard update which is used in Fig. 12a. Red semi-transparent line shows the checkerboard update results for $L = 160$. Results are qualitatively the same as in Fig. 12a although exact \tilde{J}_c value varies. Averages are taken over a smaller number of realizations than in Fig. 12a, making the high \tilde{J} data noisy.

where the θ field changes periodically and homogeneously (Fig. 39, first row), while an initially fully disordered state (m_A and m_B are chosen randomly at each point to be either $+0.1$ or -0.1) reaches a stable state with spiral defects, whose cores barely move over time (Fig. 39, second row).

We test the effect of adding noise to the mean-field equation by writing,

$$\frac{dm_i^\alpha}{dt} = -\frac{m_i^\alpha}{\tau} + \frac{1}{\tau} \tanh \left(\frac{J \sum_{j \text{ nn of } i} m_j^\alpha + K \varepsilon_{\alpha\beta} m_i^\beta}{k_B T} \right) + \eta_i^\alpha. \quad (\text{D1})$$

where η_i^α is white noise satisfying $\langle \eta_i^\alpha \rangle = 0$ and $\langle \eta_i^\alpha(t) \eta_j^\beta(t') \rangle = \zeta \delta_{\alpha\beta} \delta_{ij} \delta(t - t')$. Above some critical ζ , and for fixed system size, we observed that even when the system is initialized in an ordered state, spiral defects eventually form over time. (see Fig. 39, third row). Moreover, they are qualitatively similar to those observed when random initial conditions are implemented (Fig. 39, fourth row). In that sense, the mean-field equation with noise exhibits the same qualitative behavior as the Monte-Carlo simulations, where the swap phase is unstable in 2D.

Appendix E: Selfish free energy

The dynamics of non-conserved fields $m_\alpha(\vec{r}, t)$ with $\alpha = 1, \dots, N$ (model A) in equilibrium can be written

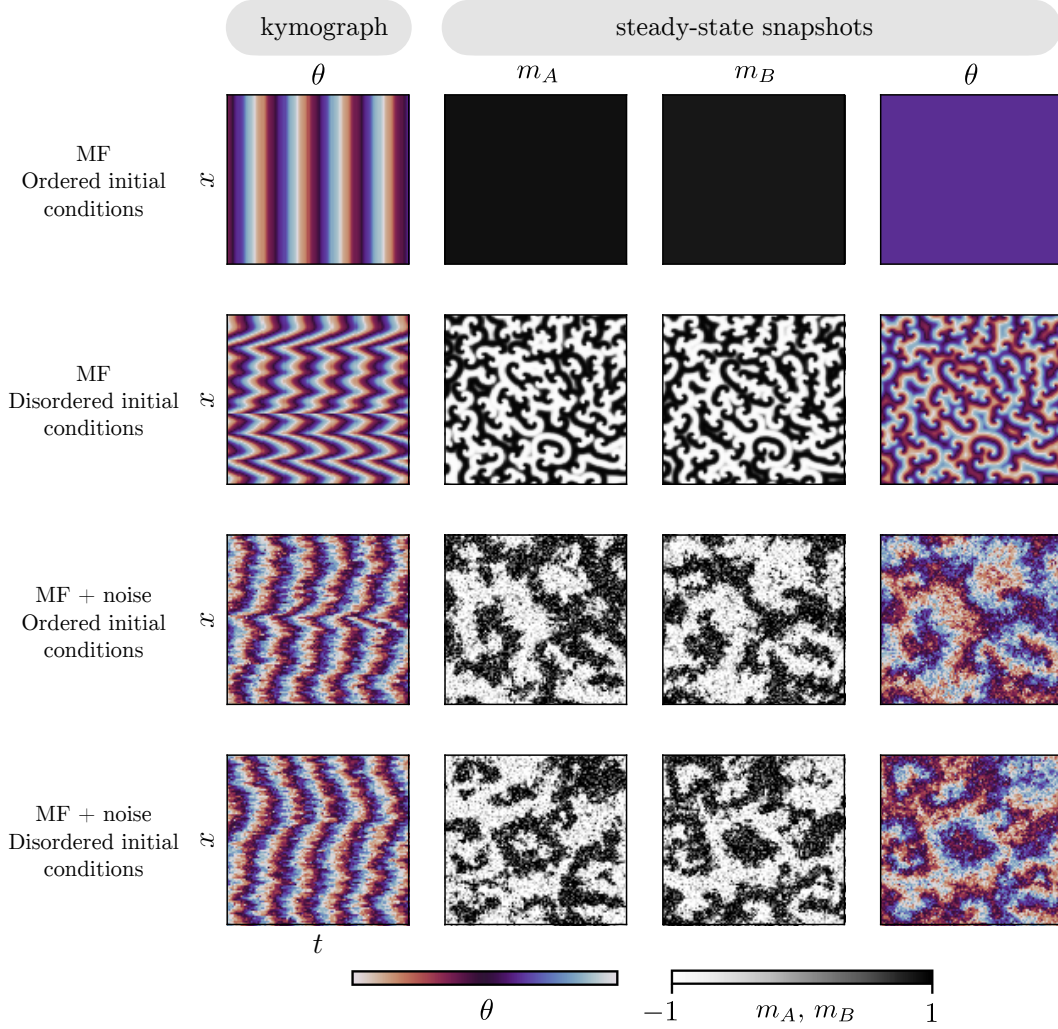


Fig. 39. The effect of added noise on the mean-field equation in 2D. Simulations of Eq. (D1) in 2D comparing the cases of no added noise with added noise and ordered vs. disordered initial conditions. First column is kymographs of the θ field for a single row on the 2D system. Second, third, and fourth columns are snapshots of the m_A , m_B , and θ fields, respectively, taken after the system has reached steady state. Without added noise, the steady state is a homogeneous swap phase for disordered initial conditions and an inhomogeneous spiral phase for ordered initial conditions. With enough added noise, the swap phase is unstable even with ordered initial conditions and spiral defects are formed for both initialization types. Simulations were performed using the Euler–Maruyama method with a time step $\Delta t = 0.05$. Noise amplitude for the case of added noise is $\zeta = 0.36$, and other system parameters are: $\bar{J} = 2$, $\bar{K} = 0.8$, $L = 200$, and $\tau = 1$. At $t = 0$, we set $m_A, m_B = 1 \pm 0.1$ for ordered initial conditions and $m_A, m_B = \pm 0.1$ for disordered initial conditions, where the plus/minus sign is chosen at random for each spin. Kymographs show evolution between $t = 9900$ and $t = 10000$.

as [27, 223, 247]

$$\partial_t m_\alpha(\vec{r}, t) = -\mu \frac{\delta \mathcal{F}[m_1, \dots, m_N]}{\delta m_\alpha(\vec{r}, t)} + \eta_\alpha(\vec{r}, t) \quad (\text{E1})$$

where \mathcal{F} is the effective free energy functional, μ is a generalized mobility, and η_α is a white noise field satisfying $\langle \eta_\alpha(\vec{r}, t) \rangle = 0$ and $\langle \eta_\alpha(\vec{r}, t) \eta_\beta(\vec{r}', t') \rangle = \zeta \delta_{\alpha\beta} \delta(\vec{r} - \vec{r}') \delta(t - t')$ where $\zeta = 2\mu k_B T$.

For nonreciprocal systems, there is no global \mathcal{F} generating the dynamics. However, we extend the notion of a free energy by writing the dynamics of the two magneti-

zation fields m_A and m_B as

$$\partial_t m_\alpha(\vec{r}, t) = -\mu \frac{\delta \mathcal{F}_\alpha[m_A, m_B]}{\delta m_\alpha(\vec{r}, t)} + \eta_\alpha(\vec{r}, t) \quad (\text{E2})$$

where \mathcal{F}_α is the *selfish free energy* of the α -species. We set $\mu = 1$ and use Eq. (30) (interpreted as the mean-field version of Eq. (E2)) to obtain the selfish free energies of the nonreciprocal Ising model in the fully anti-symmetric

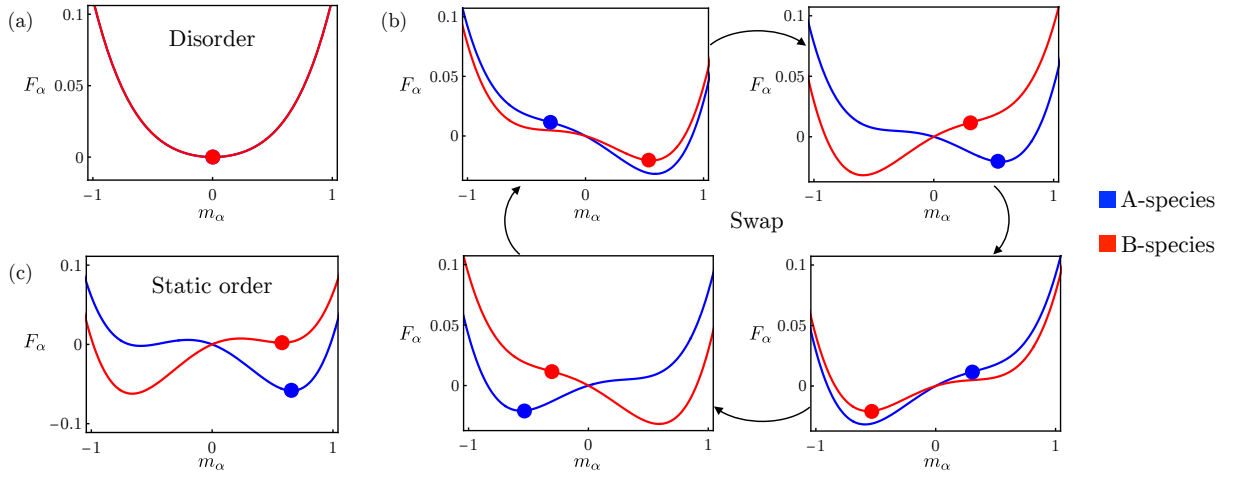


Fig. 40. Selfish free-energy landscape. F_A as a function of m_A (blue) and F_B as a function of m_B (red) in zero-dimension NR Ising model. Obtained by solving numerically the spatially homogeneous Eq. (30) in steady state, and substituting $m_A(t)$ and $m_B(t)$ into F_A and F_B defined in Eq. (E4), respectively. Actual m_A and m_B values are shown as disks. (a) Disorder, $\tilde{J} = 0.9$, (b) swap, $\tilde{J} = 1.11$, and (c) static order, $\tilde{J} = 1.3$; in all plots $\tilde{K} = 0.1$. In panel a, A and B lines as well as disks are identical and therefore only B is shown.

case,

$$\begin{aligned} \mathcal{F}_A &= \int d\vec{r} \left[\frac{1}{2} (1 - \tilde{J}) m_A^2 - \tilde{K} m_A m_B + \frac{D}{2} |\nabla m_A|^2 \right. \\ &\quad \left. + \frac{1}{12\tilde{J}} (\tilde{J} m_A + \tilde{K} m_B)^4 \right] \quad (\text{E3}) \\ \mathcal{F}_B &= \int d\vec{r} \left[\frac{1}{2} (1 - \tilde{J}) m_B^2 + \tilde{K} m_A m_B + \frac{D}{2} |\nabla m_B|^2 \right. \\ &\quad \left. + \frac{1}{12\tilde{J}} (\tilde{J} m_B - \tilde{K} m_A)^4 \right]. \end{aligned}$$

Equation (E3) can be viewed as the free-energy landscape that each species “sees”, where the free-energy landscape of A changes with m_B and vice versa.

We now restrict ourselves to the zero-dimensional case, where the selfish free energies become the functions

$$\begin{aligned} F_A &= \frac{1}{2} (1 - \tilde{J}) m_A^2 - \tilde{K} m_A m_B + \frac{1}{12\tilde{J}} (\tilde{J} m_A + \tilde{K} m_B)^4 \quad (\text{E4}) \\ F_B &= \frac{1}{2} (1 - \tilde{J}) m_B^2 + \tilde{K} m_A m_B + \frac{1}{12\tilde{J}} (\tilde{J} m_B - \tilde{K} m_A)^4. \end{aligned}$$

In order to visualize the free-energy landscape of each species at a given state, we solve the spatially homogeneous mean-field equation (Eq. (30)) and substitute the $m_B(t)$ solution into F_A and the $m_A(t)$ solution into F_B . Snapshots of the steady-state free-energy landscape are shown in Fig. 40, for the disordered, swap, and static-order phases. The actual values of m_A and m_B in steady state are shown as disks moving on the free-energy landscape.

In the disordered phase (Fig. 40a), both m_A and m_B are in the global minimum of their respective free energies. In the swap phase (Fig. 40b), the free-energy

landscape of each species changes continuously. While one species is momentarily in a global minimum, the other species is descending along the free-energy landscape which changes the free-energy landscape of the first species and so on. In the static-order phase (Fig. 40c), one of the species is at its global minimum while the second is in a local minimum, that is not the global one. This configuration is stable in mean-field, but once noise is introduced, it becomes metastable: the second species will “jump” over the barrier and reach global minimum, making the first species metastable and the cycle repeats itself. In a spatially extended system, this transition happens via droplet nucleation and growth as depicted in Sec. IX.

Appendix F: Color maps of the order parameters in 2D in the general asymmetric case

Figure 41 shows color maps of R and \mathcal{L} as a function of \tilde{J} and \tilde{K}_- with a fixed non-zero value of \tilde{K}_+ , for a 2D system with $L = 20$ (panels a-b) and $L = 80$ (panels c-d). For $L = 20$ the phase diagram resembles the mean-field prediction (Fig. 30), which includes a swap phase. However, for $L = 80$ both R and \mathcal{L} diminish and there is no apparent swap phase, supporting the conclusions of Sec. XII B.

Appendix G: Color maps of the order parameters in 3D in the general asymmetric case

In the general asymmetric case, the phase diagram is three-dimensional as it depends on \tilde{J} , \tilde{K}_+ , and \tilde{K}_- . In the main text the order parameters of the 3D system

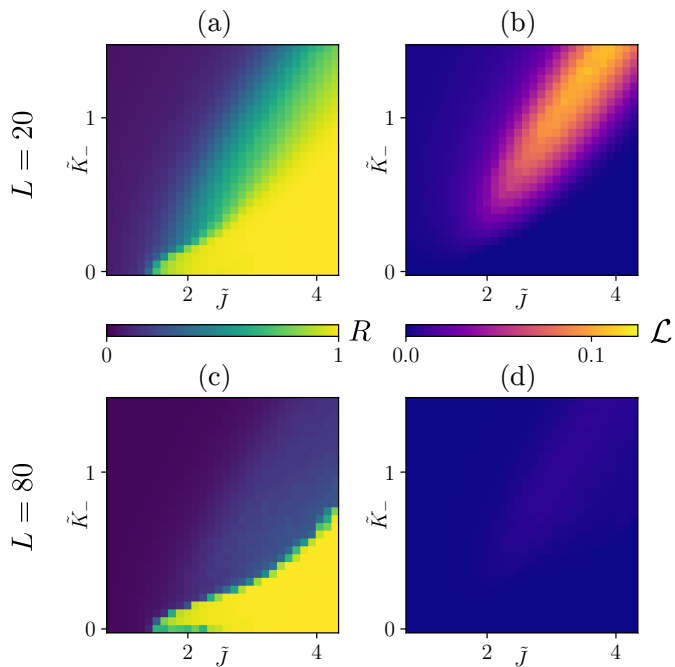


Fig. 41. Color maps of the order parameters in 2D in the general asymmetric case with fixed (non-zero) \tilde{K}_+ . (a) R and (b) \mathcal{L} color maps as a function of \tilde{J} and \tilde{K}_- , with $\tilde{K}_+ = 0.1$ and $L = 20$. (c-d) The same with $L = 80$. Obtained from MC simulations.

were calculated from MC simulations as a function of \tilde{J} and \tilde{K}_- for a fixed value of \tilde{K}_+ (Fig. 32). Figure 42 shows the order parameters on additional cuts through the three-dimensional phase diagram, both for a fixed value of \tilde{J} and for a fixed value of \tilde{K}_- , for a 3D system of linear size $L = 80$. In both cuts, the three phases of

disorder ($R = 0$ and $\mathcal{L} = 0$), swap ($R \neq 0$ and $\mathcal{L} \neq 0$) and static-order ($R \neq 0$ and $\mathcal{L} = 0$) are visible. However, the transition between the swap phase and the static-order phase is mediated by a disordered phase, as was also pointed out in Sec. XII D. The only region where a direct transition appears to occur is in the $\tilde{K}_+ \rightarrow 0$ limit, see the bottom-left part of Fig. 42a-b and the upper-left part of Fig. 42c-d. However, in this case, the static-order phase is predicted to be unstable due to droplet growth as discussed in Sec. IX, and therefore this direct transition is only observed in finite systems.

Appendix H: Supplementary movies

Movie 1: Evolution in 2D from droplet-induced oscillations to disorder caused by spiral defects. Obtained from MC simulations with parameters: $L = 150$, $\tilde{J} = 2.8$, and $\tilde{K} = 0.3$.

Movie 2: 3D stable swap phase in steady state. Obtained from MC simulations with parameters: $L = 80$, $\tilde{J} = 1.5$, and $\tilde{K} = 0.1$.

Movie 3: 3D system coarsening from a fully disordered state to scroll waves, and finally to global oscillations. Obtained from MC simulations with parameters: $L = 80$, $\tilde{J} = 2.1$, and $\tilde{K} = 0.3$. Line defects of scroll waves are found by coarse-graining the microscopic system as explained in Sec. X with $l = 3$ and $s_{\max} = 0.2$.

Movie 4: Destruction of the static-order phase in 2D by droplet growth, shown as a function of system size. Obtained from MC simulations with parameters: $\tilde{J} = 2.8$ and $\tilde{K} = 0.3$.

Movie 5: Droplet-capture mechanism in a 2D system when inter-species interactions are not fully anti-symmetric. Obtained from MC simulations with parameters: $L = 150$, $\tilde{J} = 3.3$, $\tilde{K}_+ = 0.1$, and $\tilde{K}_- = 0.3$.

-
- [1] H. Sompolinsky and I. Kanter, Temporal association in asymmetric neural networks, *Physical review letters* **57**, 2861 (1986).
 - [2] B. Derrida, E. Gardner, and A. Zippelius, An exactly solvable asymmetric neural network model, *Europhysics Letters (EPL)* **4**, 167–173 (1987).
 - [3] G. Parisi, *Journal of Physics A: Mathematical and General* **19**, L675–L680 (1986).
 - [4] H. Hong and S. H. Strogatz, Kuramoto model of coupled oscillators with positive and negative coupling parameters: An example of conformist and contrarian oscillators, *Physical Review Letters* **106**, 054102 (2011).
 - [5] H. Hong and S. H. Strogatz, Conformists and contrarians in a kuramoto model with identical natural frequencies, *Physical Review E* **84**, 046202 (2011).
 - [6] J. Garnier-Brun, M. Benzaquen, and J.-P. Bouchaud, Unlearnable games and “satisficing” decisions: A simple model for a complex world, *Physical Review X* **14**, 021039 (2024).
 - [7] V. Ros, F. Roy, G. Biroli, G. Bunin, and A. M. Turner, Generalized lotka-volterra equations with random, non-reciprocal interactions: The typical number of equilibria, *Physical Review Letters* **130**, 257401 (2023).
 - [8] J. Bascompte, P. Jordano, and J. M. Olesen, Asymmetric coevolutionary networks facilitate biodiversity maintenance, *Science* **312**, 431–433 (2006).
 - [9] M. Loreau and C. de Mazancourt, Biodiversity and ecosystem stability: a synthesis of underlying mechanisms, *Ecology Letters* **16**, 106–115 (2013).
 - [10] R. May and A. McLean, *Theoretical Ecology: Principles and Applications*, Theoretical Ecology: Principles and Applications (OUP Oxford, 2007).
 - [11] E. I. R. Chiacchio, A. Nunnenkamp, and M. Brunelli, Nonreciprocal dicke model, *Physical Review Letters* **131**, 113602 (2023).
 - [12] A. Metelmann and A. A. Clerk, Nonreciprocal photon transmission and amplification via reservoir engineering, *Physical Review X* **5**, 021025 (2015).
 - [13] A. Clerk, Introduction to quantum non-reciprocal interactions: from non-hermitian hamiltonians to

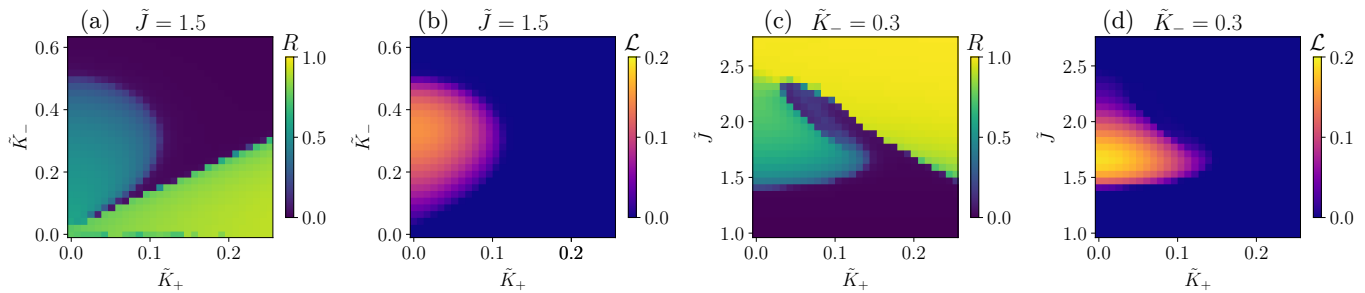


Fig. 42. Color maps of the order parameters in 3D in the general asymmetric case for a fixed value of \tilde{J} and for a fixed value of \tilde{K}_- . (a) R and (b) \mathcal{L} color maps as a function of \tilde{K}_+ and \tilde{K}_- with $\tilde{J} = 1.5$ and $L = 80$. (c) R and (d) \mathcal{L} color maps as a function \tilde{K}_+ and \tilde{J} with $\tilde{K}_- = 0.3$ and $L = 80$. Obtained from MC simulations.

- quantum master equations and quantum feedforward schemes, *SciPost Physics Lecture Notes* [10.21468/sci-postphyslectnotes.44](https://doi.org/10.21468/sci-postphyslectnotes.44) (2022).
- [14] S. Saha, J. Agudo-Canalejo, and R. Golestanian, Scalar active mixtures: The nonreciprocal cahn-hilliard model, *Physical Review X* **10**, 041009 (2020).
- [15] Z. You, A. Baskaran, and M. C. Marchetti, Nonreciprocity as a generic route to traveling states, *Proceedings of the National Academy of Sciences* **117**, 19767 (2020).
- [16] M. Fruchart, R. Hanai, P. B. Littlewood, and V. Vitelli, Non-reciprocal phase transitions, *Nature* **592**, 363 (2021).
- [17] T. Frohoff-Hülsmann and U. Thiele, Nonreciprocal cahn-hilliard model emerges as a universal amplitude equation, *Physical Review Letters* **131**, 107201 (2023).
- [18] N. Rana and R. Golestanian, Defect solutions of the nonreciprocal cahn-hilliard model: Spirals and targets, *Physical Review Letters* **133**, 078301 (2024).
- [19] F. Brauns and M. C. Marchetti, Nonreciprocal pattern formation of conserved fields, *Physical Review X* **14**, 021014 (2024).
- [20] M. Liu, Z. Hou, H. Kitahata, L. He, and S. Komura, Non-reciprocal phase separations with non-conserved order parameters, *Journal of the Physical Society of Japan* **92**, 093001 (2023).
- [21] K. L. Kreienkamp and S. H. L. Klapp, Clustering and flocking of repulsive chiral active particles with non-reciprocal couplings, *New Journal of Physics* **24**, 123009 (2022).
- [22] Y. Avni, M. Fruchart, D. Martin, D. Seara, and V. Vitelli, (to be published).
- [23] G. Ódor, Universality classes in nonequilibrium lattice systems, *Reviews of modern physics* **76**, 663 (2004).
- [24] D. Mukamel, Phase transitions in nonequilibrium systems, *Soft and fragile matter*, 237 (2000).
- [25] M. Henkel, *Non-equilibrium phase transitions* (Springer, 2008).
- [26] C. Godrèche and A. J. Bray, Nonequilibrium stationary states and phase transitions in directed ising models, *Journal of Statistical Mechanics: Theory and Experiment* **2009**, P12016 (2009).
- [27] U. C. Täuber, *Critical dynamics: a field theory approach to equilibrium and non-equilibrium scaling behavior* (Cambridge University Press, 2014).
- [28] T. Honjo, T. Sonobe, K. Inaba, T. Inagaki, T. Ikuta, Y. Yamada, T. Kazama, K. Enbutsu, T. Umeki, R. Kasahara, K.-i. Kawarabayashi, and H. Takesue, 100,000-spin coherent ising machine, *Science Advances* **7**, [10.1126/sciadv.abh0952](https://doi.org/10.1126/sciadv.abh0952) (2021).
- [29] N. Mohseni, P. L. McMahon, and T. Byrnes, Ising machines as hardware solvers of combinatorial optimization problems, *Nature Reviews Physics* **4**, 363–379 (2022).
- [30] H. Goto, K. Tatsumura, and A. R. Dixon, Combinatorial optimization by simulating adiabatic bifurcations in nonlinear hamiltonian systems, *Science Advances* **5**, [10.1126/sciadv.aav2372](https://doi.org/10.1126/sciadv.aav2372) (2019).
- [31] T. Inagaki, Y. Haribara, K. Igarashi, T. Sonobe, S. Tamate, T. Honjo, A. Marandi, P. L. McMahon, T. Umeki, K. Enbutsu, O. Tadanaga, H. Takenouchi, K. Aihara, K.-i. Kawarabayashi, K. Inoue, S. Utsunomiya, and H. Takesue, A coherent ising machine for 2000-node optimization problems, *Science* **354**, 603–606 (2016).
- [32] A. Lucas, Ising formulations of many np problems, *Frontiers in Physics* **2**, [10.3389/fphy.2014.00005](https://doi.org/10.3389/fphy.2014.00005) (2014).
- [33] H. Goto, Bifurcation-based adiabatic quantum computation with a nonlinear oscillator network, *Scientific Reports* **6**, [10.1038/srep21686](https://doi.org/10.1038/srep21686) (2016).
- [34] P. Álvarez, D. Pittilini, F. Miserocchi, S. Raamamurthy, G. Margiani, O. Ameye, J. del Pino, O. Zilberberg, and A. Eichler, Biased ising model using two coupled kerr parametric oscillators with external force, *Physical Review Letters* **132**, 207401 (2024).
- [35] C. Han, M. Wang, B. Zhang, M. I. Dykman, and H. B. Chan, Coupled parametric oscillators: From disorder-induced current to asymmetric ising model, *Physical Review Research* **6**, 023162 (2024).
- [36] D. Amit and D. Amit, *Modeling Brain Function: The World of Attractor Neural Networks* (Cambridge University Press, 1989).
- [37] M. Mézard and J. Sakellariou, Exact mean-field inference in asymmetric kinetic ising systems, *Journal of Statistical Mechanics: Theory and Experiment* **2011**, L07001 (2011).
- [38] M. Aguilera, S. A. Moosavi, and H. Shimazaki, A unifying framework for mean-field theories of asymmetric kinetic ising systems, *Nature Communications* **12**, [10.1038/s41467-021-20890-5](https://doi.org/10.1038/s41467-021-20890-5) (2021).
- [39] O. Pourret, P. Najm, and B. Marcot, *Bayesian Networks: A Practical Guide to Applications*, *Statistics in Practice* (Wiley, 2008).
- [40] R. Engelken, F. Wolf, and L. F. Abbott, Lyapunov spectra of chaotic recurrent neural networks, *Physical Review Research* **5**, 043044 (2023).
- [41] J. Fernández-Gracia, K. Suchecki, J. J. Ramasco,

- M. San Miguel, and V. M. Eguíluz, Is the voter model a model for voters?, *Physical Review Letters* **112**, 158701 (2014).
- [42] C. Castellano, S. Fortunato, and V. Loreto, Statistical physics of social dynamics, *Reviews of modern physics* **81**, 591 (2009).
- [43] M. Jusup, P. Holme, K. Kanazawa, M. Takayasu, I. Romić, Z. Wang, S. Geček, T. Lipić, B. Podobnik, L. Wang, W. Luo, T. Klanjšček, J. Fan, S. Boccaletti, and M. Perc, Social physics, *Physics Reports* **948**, 1–148 (2022).
- [44] N. Masuda, Voter models with contrarian agents, *Physical Review E—Statistical, Nonlinear, and Soft Matter Physics* **88**, 052803 (2013).
- [45] J. D. Touboul, The hipster effect: When anti-conformists all look the same, *Discrete and Continuous Dynamical Systems - B* **24**, 4379–4415 (2019).
- [46] S. D. Yi, S. K. Baek, C.-P. Zhu, and B. J. Kim, Phase transition in a coevolving network of conformist and contrarian voters, *Physical Review E* **87**, 012806 (2013).
- [47] H. Hong and S. H. Strogatz, Kuramoto model of coupled oscillators with positive and negative coupling parameters: An example of conformist and contrarian oscillators, *Physical Review Letters* **106**, 054102 (2011).
- [48] F. Bagnoli and R. Rechtman, Bifurcations in models of a society of reasonable contrarians and conformists, *Physical Review E* **92**, 042913 (2015).
- [49] J. P. Caulkins, R. F. Hartl, P. M. Kort, and G. Feichtinger, Explaining fashion cycles: Imitators chasing innovators in product space, *Journal of Economic Dynamics and Control* **31**, 1535–1556 (2007).
- [50] Y. Shi and T. Duke, Cooperative model of bacterial sensing, *Physical Review E* **58**, 6399–6406 (1998).
- [51] T. A. J. Duke and D. Bray, Heightened sensitivity of a lattice of membrane receptors, *Proceedings of the National Academy of Sciences* **96**, 10104–10108 (1999).
- [52] B. A. Mello and Y. Tu, Quantitative modeling of sensitivity in bacterial chemotaxis: The role of coupling among different chemoreceptor species, *Proceedings of the National Academy of Sciences* **100**, 8223–8228 (2003).
- [53] B. Hu, W. Chen, W.-J. Rappel, and H. Levine, Physical limits on cellular sensing of spatial gradients, *Physical Review Letters* **105**, 048104 (2010).
- [54] Y. Tu, Quantitative modeling of bacterial chemotaxis: Signal amplification and accurate adaptation, *Annual Review of Biophysics* **42**, 337–359 (2013).
- [55] D. Hathcock, Q. Yu, and Y. Tu, Time-reversal symmetry breaking in the chemosensory array reveals a general mechanism for dissipation-enhanced cooperative sensing, *Nature Communications* **15**, 8892 (2024).
- [56] D. Hathcock, Q. Yu, B. A. Mello, D. N. Amin, G. L. Hazelbauer, and Y. Tu, A nonequilibrium allosteric model for receptor-kinase complexes: The role of energy dissipation in chemotaxis signaling, *Proceedings of the National Academy of Sciences* **120**, 10.1073/pnas.2303115120 (2023).
- [57] D. M. Sherry, I. R. Graf, S. J. Bryant, T. Emonet, and B. B. Machta, *Lattice ultrasensitivity produces large gain in colicemosensing* (2024).
- [58] J. J. Hopfield, Neural networks and physical systems with emergent collective computational abilities., *Proceedings of the National Academy of Sciences* **79**, 2554–2558 (1982).
- [59] D. Krotov and J. J. Hopfield, Unsupervised learning by competing hidden units, *Proceedings of the National Academy of Sciences* **116**, 7723–7731 (2019).
- [60] Z.-B. Xu, G.-Q. Hu, and C.-P. Kwong, Asymmetric hopfield-type networks: Theory and applications, *Neural Networks* **9**, 483–501 (1996).
- [61] H. Sompolinsky, The theory of neural networks: The hebb rule and beyond, in *Heidelberg Colloquium on Glassy Dynamics* (Springer Berlin Heidelberg, 1987) p. 485–527.
- [62] A. Crisanti and H. Sompolinsky, Dynamics of spin systems with randomly asymmetric bonds: Langevin dynamics and a spherical model, *Physical Review A* **36**, 4922–4939 (1987).
- [63] T. Chen and S. Amari, Stability of asymmetric hopfield networks, *IEEE Transactions on Neural Networks* **12**, 159–163 (2001).
- [64] E. M. Izhikevich, *Dynamical Systems In Neuroscience* (MIT Press, 2007).
- [65] C. W. Lynn, E. J. Cornblath, L. Papadopoulos, M. A. Bertolero, and D. S. Bassett, Broken detailed balance and entropy production in the human brain, *Proceedings of the National Academy of Sciences* **118**, e2109889118 (2021).
- [66] B. Buča and D. Jaksch, Dissipation induced nonstationarity in a quantum gas, *Physical Review Letters* **123**, 260401 (2019).
- [67] E. I. R. Chiacchio and A. Nunnenkamp, Dissipation-induced instabilities of a spinor bose-einstein condensate inside an optical cavity, *Physical Review Letters* **122**, 193605 (2019).
- [68] N. Dogra, M. Landini, K. Kroeger, L. Hruby, T. Donner, and T. Esslinger, Dissipation-induced structural instability and chiral dynamics in a quantum gas, *Science* **366**, 1496–1499 (2019).
- [69] H. C. Nguyen, R. Zecchina, and J. Berg, Inverse statistical problems: from the inverse ising problem to data science, *Advances in Physics* **66**, 197–261 (2017).
- [70] L. Zdeborová and F. Krzakala, Statistical physics of inference: thresholds and algorithms, *Advances in Physics* **65**, 453–552 (2016).
- [71] S. L. Dettmer, H. C. Nguyen, and J. Berg, Network inference in the nonequilibrium steady state, *Physical Review E* **94**, 052116 (2016).
- [72] S. Cocco, S. Leibler, and R. Monasson, Neuronal couplings between retinal ganglion cells inferred by efficient inverse statistical physics methods, *Proceedings of the National Academy of Sciences* **106**, 14058–14062 (2009).
- [73] T. Mora and W. Bialek, Are biological systems poised at criticality?, *Journal of Statistical Physics* **144**, 268–302 (2011).
- [74] M. A. Muñoz, Colloquium: Criticality and dynamical scaling in living systems, *Reviews of Modern Physics* **90**, 031001 (2018).
- [75] J. M. Beggs and N. Timme, Being critical of criticality in the brain, *Frontiers in Physiology* **3**, 10.3389/fphys.2012.00163 (2012).
- [76] M. A. Buice and J. D. Cowan, Field-theoretic approach to fluctuation effects in neural networks, *Physical Review E* **75**, 051919 (2007).
- [77] J. D. Cowan, J. Neuman, B. Kiewiet, and W. van Dronghen, Self-organized criticality in a network of interacting neurons, *Journal of Statistical Mechanics: Theory and Experiment* **2013**, P04030 (2013).

- [78] J. D. Cowan, J. Neuman, and W. van Drongelen, Wilson–cowan equations for neocortical dynamics, *The Journal of Mathematical Neuroscience* **6**, 10.1186/s13408-015-0034-5 (2016).
- [79] C. Borile, A. Maritan, and M. A. Muñoz, The effect of quenched disorder in neutral theories, *Journal of Statistical Mechanics: Theory and Experiment* **2013**, P04032 (2013).
- [80] D. J. Watts and S. H. Strogatz, Collective dynamics of ‘small-world’ networks, *Nature* **393**, 440–442 (1998).
- [81] M. Barthélemy, Spatial networks, *Physics Reports* **499**, 1–101 (2011).
- [82] P. C. Hohenberg, Existence of long-range order in one and two dimensions, *Physical Review* **158**, 383–386 (1967).
- [83] S. H. Strogatz, *Nonlinear Dynamics and Chaos* (CRC Press, 2018) p. 532.
- [84] Y. A. Kuznetsov, *Elements of Applied Bifurcation Theory* (Springer International Publishing, 2023).
- [85] Y. Kuramoto, *Chemical Oscillations, Waves, and Turbulence* (Springer, 1984).
- [86] I. S. Aranson and L. Kramer, The world of the complex ginzburg-landau equation, *Reviews of modern physics* **74**, 99 (2002).
- [87] S. Camalet, T. Duke, F. Jülicher, and J. Prost, Auditory sensitivity provided by self-tuned critical oscillations of hair cells, *Proceedings of the national academy of sciences* **97**, 3183 (2000).
- [88] A. Hudspeth, F. Jülicher, and P. Martin, A critique of the critical cochlea: Hopf—a bifurcation—is better than none, *Journal of neurophysiology* **104**, 1219 (2010).
- [89] T. Risler, J. Prost, and F. Jülicher, Universal critical behavior of noisy coupled oscillators, *Physical review letters* **93**, 175702 (2004).
- [90] T. Risler, J. Prost, and F. Jülicher, Universal critical behavior of noisy coupled oscillators: A renormalization group study, *Physical Review E* **72**, 016130 (2005).
- [91] R. Daviet, C. P. Zelle, A. Rosch, and S. Diehl, Nonequilibrium criticality at the onset of time-crystalline order, *Physical Review Letters* **132**, 167102 (2024).
- [92] C. P. Zelle, R. Daviet, A. Rosch, and S. Diehl, Universal Phenomenology at Critical Exceptional Points of Nonequilibrium $O(N)$ Models, *Physical Review X* **14**, 021052 (2024).
- [93] References [89, 90] conjecture that quasi-long-range may be present at $d = 2$, but more recent studies based on a mapping to a version of the Kardar-Parisi-Zhang (KPZ) equation with compact variables suggest that the phase with algebraic order does not persist in the limit of large systems (nor an equivalent of the Berezinskii-Kosterlitz-Thouless (BKT) transition) but are replaced with a stretched exponential decay of correlations corresponding to the rough phase of the KPZ equation [106, 107]. In addition, Refs. [177] argue that the modified effective interaction between spiral defects (compared to that between XY vortices) allows for a finite density of defects at any temperature, potentially suppressing the algebraic order.
- [94] K. Wood, C. Van den Broeck, R. Kawai, and K. Lindenberg, Critical behavior and synchronization of discrete stochastic phase-coupled oscillators, *Physical Review E* **74**, 031113 (2006).
- [95] K. Wood, C. Van den Broeck, R. Kawai, and K. Lindenberg, Universality of synchrony: critical behavior in a discrete model of stochastic phase-coupled oscillators, *Physical review letters* **96**, 145701 (2006).
- [96] V. R. Assis, M. Copelli, and R. Dickman, An infinite-period phase transition versus nucleation in a stochastic model of collective oscillations, *Journal of Statistical Mechanics: Theory and Experiment* **2011**, P09023 (2011).
- [97] T. Bohr, G. Grinstein, Y. He, and C. Jayaprakash, Coherence, chaos, and broken symmetry in classical, many-body dynamical systems, *Physical Review Letters* **58**, 2155–2158 (1987).
- [98] G. Grinstein, Stability of nonstationary states of classical, many-body dynamical systems, *Journal of Statistical Physics* **51**, 803–815 (1988).
- [99] C. H. Bennett, G. Grinstein, Y. He, C. Jayaprakash, and D. Mukamel, Stability of temporally periodic states of classical many-body systems, *Physical Review A* **41**, 1932 (1990).
- [100] G. Grinstein, C. Jayaprakash, and C. H. Bennett, Comment on “second-order dynamics in the collective temporal evolution of complex systems”, *Physical Review Letters* **73**, 3038–3038 (1994).
- [101] Note that these arguments require that the system is isotropic and that the noise is unbounded so that it can create arbitrarily large droplets [99, 100].
- [102] G. Grinstein, D. Mukamel, R. Seidin, and C. H. Bennett, Temporally periodic phases and kinetic roughening, *Physical review letters* **70**, 3607 (1993).
- [103] M. Kardar, G. Parisi, and Y.-C. Zhang, Dynamic scaling of growing interfaces, *Physical Review Letters* **56**, 889–892 (1986).
- [104] R. Livi and P. Politi, *Nonequilibrium Statistical Physics: A Modern Perspective* (Cambridge University Press, 2017).
- [105] L. Chen and J. Toner, Universality for moving stripes: A hydrodynamic theory of polar active smectics, *Physical Review Letters* **111**, 088701 (2013).
- [106] E. Altman, L. M. Sieberer, L. Chen, S. Diehl, and J. Toner, Two-dimensional superfluidity of exciton polaritons requires strong anisotropy, *Physical Review X* **5**, 011017 (2015).
- [107] G. Wachtel, L. Sieberer, S. Diehl, and E. Altman, Electrodynamical duality and vortex unbinding in driven-dissipative condensates, *Physical Review B* **94**, 104520 (2016).
- [108] I. S. Aranson, S. Scheidl, and V. M. Vinokur, Nonequilibrium dislocation dynamics and instability of driven vortex lattices in two dimensions, *Physical Review B* **58**, 14541–14547 (1998).
- [109] C.-K. Chan, T. E. Lee, and S. Gopalakrishnan, Limit-cycle phase in driven-dissipative spin systems, *Physical Review A* **91**, 051601 (2015).
- [110] N. D. Mermin and H. Wagner, Absence of ferromagnetism or antiferromagnetism in one- or two-dimensional isotropic heisenberg models, *Physical Review Letters* **17**, 1133–1136 (1966).
- [111] H. Chaté and P. Manneville, Evidence of collective behaviour in cellular automata, *Europhysics Letters (EPL)* **14**, 409–413 (1991).
- [112] H. Chaté and P. Manneville, Collective behaviors in spatially extended systems with local interactions and synchronous updating, *Progress of Theoretical Physics* **87**, 1–60 (1992).
- [113] H. Chaté, G. Grinstein, and L.-H. Tang, Long-range cor-

- relations in systems with coherent (quasi)periodic oscillations, *Physical Review Letters* **74**, 912–915 (1995).
- [114] H. Chaté and J. Losson, Non-trivial collective behavior in coupled map lattices: A transfer operator perspective, *Physica D: Nonlinear Phenomena* **103**, 51–72 (1997).
- [115] J. Gallas, P. Grassberger, H. Herrmann, and P. Ueberholz, Noisy collective behaviour in deterministic cellular automata, *Physica A: Statistical Mechanics and its Applications* **180**, 19–41 (1992).
- [116] P.-M. Binder and V. Privman, Second-order dynamics in the collective temporal evolution of complex systems, *Physical Review Letters* **68**, 3830–3833 (1992).
- [117] J. Hemmingsson and H. J. Herrmann, On oscillations in cellular automata, *Europhysics Letters (EPL)* **23**, 15–19 (1993).
- [118] J. Losson and M. C. Mackey, Evolution of probability densities in stochastic coupled map lattices, *Physical Review E* **52**, 1403–1417 (1995).
- [119] Y. Pomeau, Periodic behavior of cellular automata, *Journal of Statistical Physics* **70**, 1379–1382 (1993).
- [120] H. Chaté, A. Lemaître, P. Marcq, and P. Manneville, Non-trivial collective behavior in extensively-chaotic dynamical systems: an update, *Physica A: Statistical Mechanics and its Applications* **224**, 447–457 (1996).
- [121] A. Lipowski, Oscillatory behavior in a lattice prey-predator system, *Physical Review E* **60**, 5179–5184 (1999).
- [122] A. Lipowski and D. Lipowska, Nonequilibrium phase transition in a lattice prey–predator system, *Physica A: Statistical Mechanics and its Applications* **276**, 456–464 (2000).
- [123] M. Mobilia, I. T. Georgiev, and U. C. Täuber, Phase transitions and spatio-temporal fluctuations in stochastic lattice lotka–volterra models, *Journal of Statistical Physics* **128**, 447–483 (2006).
- [124] T. Antal, M. Droz, A. Lipowski, and G. Ódor, Critical behavior of a lattice prey-predator model, *Physical Review E* **64**, 036118 (2001).
- [125] T. Antal and M. Droz, Phase transitions and oscillations in a lattice prey-predator model, *Physical Review E* **63**, 056119 (2001).
- [126] U. C. Täuber, Stochastic spatial lotka-volterra predator-prey models (2024), [arXiv:2405.05006](https://arxiv.org/abs/2405.05006).
- [127] J. A. Acebrón, L. L. Bonilla, C. J. P. Vicente, F. Ritort, and R. Spigler, The kuramoto model: A simple paradigm for synchronization phenomena, *Reviews of modern physics* **77**, 137 (2005).
- [128] This can be seen by integrating $d\phi_t = \omega dt + \sqrt{2D_\phi} dW_t$ where W_t is a standard Wiener process, leading to $\phi(t) - \phi(0) = \omega t + \sqrt{2D_\phi} W_t$. We find $C(t) = e^{i\omega t} \langle e^{i\sqrt{2D_\phi} W_t} \rangle$. As W_t follows a normal distribution $\mathcal{N}(\mu = 0, \sigma^2 = t)$, its moment generating function is $M_{W_t}(x) \equiv \mathbb{E}(e^{xW_t}) = e^{\mu x + \sigma^2 x^2/2}$ from which the result is found.
- [129] P. Gaspard, The correlation time of mesoscopic chemical clocks, *The Journal of Chemical Physics* **117**, 8905–8916 (2002).
- [130] Y. Cao, H. Wang, Q. Ouyang, and Y. Tu, The free-energy cost of accurate biochemical oscillations, *Nature Physics* **11**, 772–778 (2015).
- [131] L. Oberreiter, U. Seifert, and A. C. Barato, Universal minimal cost of coherent biochemical oscillations, *Physical Review E* **106**, 014106 (2022).
- [132] N. Shiraishi, Entropy production limits all fluctuation oscillations, *Physical Review E* **108**, 042103 (2023).
- [133] N. Ohga, S. Ito, and A. Kolchinsky, Thermodynamic bound on the asymmetry of cross-correlations, *Physical Review Letters* **131**, 077101 (2023).
- [134] V. Khemani, R. Moessner, and S. L. Sondhi, A brief history of time crystals (2019), [arXiv:1910.10745](https://arxiv.org/abs/1910.10745).
- [135] K. Sacha and J. Zakrzewski, Time crystals: a review, *Reports on Progress in Physics* **81**, 016401 (2017).
- [136] F. Iemini, A. Russomanno, J. Keeling, M. Schirò, M. Dalmonte, and R. Fazio, Boundary time crystals, *Physical Review Letters* **121**, 035301 (2018).
- [137] B. Buča, J. Tindall, and D. Jaksch, Non-stationary coherent quantum many-body dynamics through dissipation, *Nature Communications* **10**, 10.1038/s41467-019-09757-y (2019).
- [138] H. Keßler, J. G. Cosme, M. Hemmerling, L. Mathey, and A. Hemmerich, Emergent limit cycles and time crystal dynamics in an atom-cavity system, *Physical Review A* **99**, 053605 (2019).
- [139] P. Kongkhambut, J. Skulte, L. Mathey, J. G. Cosme, A. Hemmerich, and H. Keßler, Observation of a continuous time crystal, *Science* **377**, 670–673 (2022).
- [140] N. Y. Yao, C. Nayak, L. Balents, and M. P. Zaletel, Classical discrete time crystals, *Nature Physics* **16**, 438–447 (2020).
- [141] M. P. Zaletel, M. Lukin, C. Monroe, C. Nayak, F. Wilczek, and N. Y. Yao, Colloquium : Quantum and classical discrete time crystals, *Reviews of Modern Physics* **95**, 031001 (2023).
- [142] A. T. Winfree, *The geometry of biological time*, Vol. 2 (Springer, 1980).
- [143] F. Wilczek, Quantum time crystals, *Physical Review Letters* **109**, 160401 (2012).
- [144] A. Shapere and F. Wilczek, Classical time crystals, *Physical Review Letters* **109**, 160402 (2012).
- [145] N. Y. Yao and C. Nayak, Time crystals in periodically driven systems, *Physics Today* **71**, 40–47 (2018).
- [146] P. Kongkhambut, J. Skulte, L. Mathey, J. G. Cosme, A. Hemmerich, and H. Keßler, Observation of a continuous time crystal, *Science* **377**, 670 (2022).
- [147] X. Wu, Z. Wang, F. Yang, R. Gao, C. Liang, M. K. Tey, X. Li, T. Pohl, and L. You, Dissipative time crystal in a strongly interacting rydberg gas, *Nature Physics* **20**, 1389 (2024).
- [148] R. J. Glauber, Time-dependent statistics of the ising model, *Journal of mathematical physics* **4**, 294 (1963).
- [149] S. A. M. Loos, S. H. L. Klapp, and T. Martynek, Long-range order and directional defect propagation in the nonreciprocal xy model with vision cone interactions, *Physical Review Letters* **130**, 198301 (2023).
- [150] L. Guislain and E. Bertin, Nonequilibrium phase transition to temporal oscillations in mean-field spin models, *Physical Review Letters* **130**, 207102 (2023).
- [151] L. Guislain and E. Bertin, Discontinuous phase transition from ferromagnetic to oscillating states in a nonequilibrium mean-field spin model, *Physical Review E* **109**, 034131 (2024).
- [152] F. Lima and D. Stauffer, Ising model simulation in directed lattices and networks, *Physica A: Statistical Mechanics and its Applications* **359**, 423 (2006).
- [153] A. Sánchez, J. López, and M. Rodríguez, Nonequilibrium phase transitions in directed small-world networks, *Physical Review Letters* **88**, 048701 (2002).

- [154] A. Lipowski, A. L. Ferreira, D. Lipowska, and K. Gontarek, Phase transitions in ising models on directed networks, *Physical Review E* **92**, 052811 (2015).
- [155] S. L. Kalpazidou, *Cycle representations of Markov processes*, Vol. 28 (Springer Science & Business Media, 2007).
- [156] U. Seifert, Stochastic thermodynamics, fluctuation theorems and molecular machines, *Reports on Progress in Physics* **75**, 126001 (2012).
- [157] J. M. Horowitz and T. R. Gingrich, Thermodynamic uncertainty relations constrain non-equilibrium fluctuations, *Nature Physics* **16**, 15 (2019).
- [158] C. Maes, Local detailed balance, SciPost Physics Lecture Notes **10.21468/scipostphyslectnotes.32** (2021).
- [159] T. Martynek, S. H. L. Klapp, and S. A. M. Loos, Entropy production at criticality in a nonequilibrium potts model, *New Journal of Physics* **22**, 093069 (2020).
- [160] H. Alston, L. Cocconi, and T. Bertrand, Irreversibility across a nonreciprocal pt-symmetry-breaking phase transition, *Physical Review Letters* **131**, 258301 (2023).
- [161] T. Suchanek, K. Kroy, and S. A. M. Loos, Time-reversal and parity-time symmetry breaking in non-hermitian field theories, *Physical Review E* **108**, 064123 (2023).
- [162] C. Nardini, É. Fodor, E. Tjhung, F. van Wijland, J. Tailleur, and M. E. Cates, Entropy production in field theories without time-reversal symmetry: Quantifying the non-equilibrium character of active matter, *Physical Review X* **7**, 021007 (2017).
- [163] D. S. Seara, B. B. Machta, and M. P. Murrell, Irreversibility in dynamical phases and transitions, *Nature Communications* **12**, 10.1038/s41467-020-20281-2 (2021).
- [164] M. Suzuki and R. Kubo, Dynamics of the ising model near the critical point. i, *Journal of the Physical Society of Japan* **24**, 51–60 (1968).
- [165] G. Forgacs, D. Mukamel, and R. A. Pelcovits, Glauber dynamics for one-dimensional spin models with random fields, *Physical Review B* **30**, 205–208 (1984).
- [166] K.-t. Leung, Heuristic derivation of continuum kinetic equations from microscopic dynamics, *Physical Review E* **63**, 016102 (2000).
- [167] M. Suzuki, Solution of potts model for phase transition, *Progress of Theoretical Physics* **37**, 770 (1967).
- [168] J. Tobochnik, Properties of the q-state clock model for $q=4, 5$, and 6 , *Physical Review B* **26**, 6201 (1982).
- [169] V. García-Morales and K. Krischer, The complex ginzburg–landau equation: an introduction, *Contemporary Physics* **53**, 79 (2012).
- [170] J. D. Crawford and E. Knobloch, Symmetry and symmetry-breaking bifurcations in fluid dynamics, *Annual Review of Fluid Mechanics* **23**, 341–387 (1991).
- [171] M. Golubitsky, I. Stewart, and D. G. Schaeffer, *Singularities and Groups in Bifurcation Theory*, Vol. II (Springer New York, 1988).
- [172] P. Chossat and R. Lauterbach, *Methods in Equivariant Bifurcations and Dynamical Systems* (World Scientific, 2000).
- [173] K. Yang, Y.-F. Chen, G. Roumpos, C. Colby, and J. Anderson, High performance monte carlo simulation of ising model on tpu clusters, in *Proceedings of the International Conference for High Performance Computing, Networking, Storage and Analysis* (2019) pp. 1–15.
- [174] D. S. Seara, B. B. Machta, and M. P. Murrell, Irreversibility in dynamical phases and transitions, *Nature communications* **12**, 392 (2021).
- [175] K. J. Burns, G. M. Vasil, J. S. Oishi, D. Lecoanet, and B. P. Brown, Dedalus: A flexible framework for numerical simulations with spectral methods, *Physical Review Research* **2**, 023068 (2020).
- [176] U. M. Ascher, S. J. Ruuth, and R. J. Spiteri, Implicit-explicit runge-kutta methods for time-dependent partial differential equations, *Applied Numerical Mathematics* **25**, 151–167 (1997).
- [177] I. S. Aranson, H. Chaté, and L.-H. Tang, Spiral motion in a noisy complex ginzburg-landau equation, *Physical review letters* **80**, 2646 (1998).
- [178] I. S. Aranson, L. Kramer, and A. Weber, Theory of interaction and bound states of spiral waves in oscillatory media, *Physical Review E* **47**, 3231–3241 (1993).
- [179] H. Chaté and P. Manneville, Phase diagram of the two-dimensional complex ginzburg-landau equation, *Physica A: Statistical Mechanics and its Applications* **224**, 348 (1996).
- [180] T. H. Tan, J. Liu, P. W. Miller, M. Tekant, J. Dunkel, and N. Fakhri, Topological turbulence in the membrane of a living cell, *Nature Physics* **16**, 657 (2020).
- [181] J. Liu, J. F. Totz, P. W. Miller, A. D. Hastewell, Y.-C. Chao, J. Dunkel, and N. Fakhri, Topological braiding and virtual particles on the cell membrane, *Proceedings of the National Academy of Sciences* **118**, e2104191118 (2021).
- [182] A. Michaud, M. Leda, Z. T. Swider, S. Kim, J. He, J. Landino, J. R. Valley, J. Huisken, A. B. Goryachev, G. von Dassow, and W. M. Bement, A versatile cortical pattern-forming circuit based on rho, f-actin, ect2, and rga-3/4, *Journal of Cell Biology* **221**, 10.1083/jcb.202203017 (2022).
- [183] F. Brauns, G. Pawlik, J. Halatek, J. Kerssemakers, E. Frey, and C. Dekker, Bulk-surface coupling identifies the mechanistic connection between min-protein patterns in vivo and in vitro, *Nature Communications* **12**, 10.1038/s41467-021-23412-5 (2021).
- [184] Y. Zhang and É. Fodor, Pulsating active matter, *Physical Review Letters* **131**, 238302 (2023).
- [185] A. Manacorda and É. Fodor, Pulsating with discrete symmetry, arXiv preprint [arXiv:2310.14370](https://arxiv.org/abs/2310.14370) (2023).
- [186] M. E. Newman and G. T. Barkema, *Monte Carlo methods in statistical physics* (Clarendon Press, 1999).
- [187] K. Binder, Monte carlo simulation in statistical physics (1992).
- [188] K. Binder, Finite size scaling analysis of ising model block distribution functions, *Zeitschrift für Physik B Condensed Matter* **43**, 119 (1981).
- [189] H. Hong, H. Chaté, L.-H. Tang, and H. Park, Finite-size scaling, dynamic fluctuations, and hyperscaling relation in the kuramoto model, *Physical Review E* **92**, 022122 (2015).
- [190] H. Hong, Finite-size scaling in the system of coupled oscillators with heterogeneity in coupling strength, *Physical Review E* **96**, 012213 (2017).
- [191] M. Sarkar, Synchronization transition in the two-dimensional kuramoto model with dichotomous noise, *Chaos: An Interdisciplinary Journal of Nonlinear Science* **31** (2021).
- [192] P. Virtanen, R. Gommers, T. E. Oliphant, M. Haberland, T. Reddy, D. Cournapeau, E. Burovski, P. Peterson, W. Weckesser, J. Bright, S. J. van der Walt, M. Brett, J. Wilson, K. J. Millman, N. Mayorov, A. R. J.

- Nelson, E. Jones, R. Kern, E. Larson, C. J. Carey, Í. Polat, Y. Feng, E. W. Moore, J. VanderPlas, D. Laxalde, J. Perktold, R. Cimrman, I. Henriksen, E. A. Quintero, C. R. Harris, A. M. Archibald, A. H. Ribeiro, F. Pedregosa, P. van Mulbregt, and SciPy 1.0 Contributors, SciPy 1.0: Fundamental Algorithms for Scientific Computing in Python, *Nature Methods* **17**, 261 (2020).
- [193] D. S. Moore and S. Kirkland, *The basic practice of statistics*, Vol. 2 (WH Freeman New York, 2007).
- [194] A. Pelissetto and E. Vicari, Critical phenomena and renormalization-group theory, *Physics Reports* **368**, 549 (2002).
- [195] M. Campostrini, M. Hasenbusch, A. Pelissetto, P. Rossi, and E. Vicari, Critical behavior of the three-dimensional xy universality class, *Physical Review B* **63**, 214503 (2001).
- [196] M. Hasenbusch and T. Török, High-precision monte carlo study of the 3d xy-universality class, *Journal of Physics A: Mathematical and General* **32**, 6361 (1999).
- [197] K. Binder and E. Luijten, Monte carlo tests of renormalization-group predictions for critical phenomena in ising models, *Physics Reports* **344**, 179 (2001).
- [198] P. Gaspard, *Journal of Statistical Physics* **106**, 57–96 (2002).
- [199] L. G. Morelli and F. Jülicher, Precision of genetic oscillators and clocks, *Physical Review Letters* **98**, 228101 (2007).
- [200] S. Bagheri, Effects of weak noise on oscillating flows: Linking quality factor, floquet modes, and koopman spectrum, *Physics of Fluids* **26**, 10.1063/1.4895898 (2014).
- [201] C. del Junco and S. Vaikuntanathan, Robust oscillations in multi-cyclic markov state models of biochemical clocks, *The Journal of Chemical Physics* **152**, 10.1063/1.5143259 (2020).
- [202] C. del Junco and S. Vaikuntanathan, High chemical affinity increases the robustness of biochemical oscillations, *Physical Review E* **101**, 012410 (2020).
- [203] A. C. Barato and U. Seifert, Coherence of biochemical oscillations is bounded by driving force and network topology, *Physical Review E* **95**, 062409 (2017).
- [204] C. Fei, Y. Cao, Q. Ouyang, and Y. Tu, Design principles for enhancing phase sensitivity and suppressing phase fluctuations simultaneously in biochemical oscillatory systems, *Nature Communications* **9**, 10.1038/s41467-018-03826-4 (2018).
- [205] H. Wierenga, P. R. ten Wolde, and N. B. Becker, Quantifying fluctuations in reversible enzymatic cycles and clocks, *Physical Review E* **97**, 042404 (2018).
- [206] B. Nguyen, U. Seifert, and A. C. Barato, Phase transition in thermodynamically consistent biochemical oscillators, *The Journal of Chemical Physics* **149**, 10.1063/1.5032104 (2018).
- [207] R. Marsland, W. Cui, and J. M. Horowitz, The thermodynamic uncertainty relation in biochemical oscillations, *Journal of The Royal Society Interface* **16**, 20190098 (2019).
- [208] L. Brunnet, H. Chaté, and P. Manneville, Long-range order with local chaos in lattices of diffusively coupled odes, *Physica D: Nonlinear Phenomena* **78**, 141–154 (1994).
- [209] A. Lemaitre, H. Chaté, and P. Manneville, Cluster expansion for collective behavior in discrete-space dynamical systems, *Physical Review Letters* **77**, 486–489 (1996).
- [210] J. Losson and M. C. Mackey, Statistical cycling in coupled map lattices, *Physical Review E* **50**, 843–856 (1994).
- [211] J. Wendykier, A. Lipowski, and A. L. Ferreira, Coexistence and critical behavior in a lattice model of competing species, *Physical Review E* **83**, 031904 (2011).
- [212] P.-M. Binder and J. F. Jaramillo, Stabilization of coherent oscillations in spatially extended dynamical systems, *Physical Review E* **56**, 2276–2278 (1997).
- [213] L. Oberreiter, U. Seifert, and A. C. Barato, Stochastic discrete time crystals: Entropy production and subharmonic synchronization, *Physical Review Letters* **126**, 020603 (2021).
- [214] M.-F. Chen, *Eigenvalues, inequalities, and ergodic theory*, 2005th ed., Probability and Its Applications (Springer, 2004).
- [215] T. Liggett, *Interacting Particle Systems*, Grundlehren der mathematischen Wissenschaften (Springer New York, 2012).
- [216] F. Martinelli, Lectures on glaufer dynamics for discrete spin models, in *Lectures on Probability Theory and Statistics* (Springer Berlin Heidelberg, 1999) p. 93–191.
- [217] F. Carollo and I. Lesanovsky, Exact solution of a boundary time-crystal phase transition: Time-translation symmetry breaking and non-markovian dynamics of correlations, *Physical Review A* **105**, 1040202 (2022).
- [218] F. Siegert and C. J. Weijer, Three-dimensional scroll waves organize dictyostelium slugs., *Proceedings of the National Academy of Sciences* **89**, 6433 (1992).
- [219] M. Gabbay, E. Ott, and P. N. Guzdar, Motion of scroll wave filaments in the complex ginzburg-landau equation, *Physical review letters* **78**, 2012 (1997).
- [220] Note that these potential droplets are *not* the droplets that destabilize the static-order phase (as in Fig. 21). Instead, these are droplets of a homogeneously oscillating state, immersed in an oscillatory background with a different phase.
- [221] P. Coulet, J. Lega, B. Houchmandzadeh, and J. Lajzerowicz, Breaking chirality in nonequilibrium systems, *Physical review letters* **65**, 1352 (1990).
- [222] B. Benvegnen, O. Granek, S. Ro, R. Yaacoby, H. Chaté, Y. Kafri, D. Mukamel, A. Solon, and J. Tailleur, Metastability of discrete-symmetry flocks, *Physical review letters* **131**, 218301 (2023).
- [223] M. Kardar, *Statistical physics of fields* (Cambridge University Press, 2007).
- [224] J.-n. Teramae, H. Nakao, and G. B. Ermentrout, Stochastic phase reduction for a general class of noisy limit cycle oscillators, *Physical Review Letters* **102**, 194102 (2009).
- [225] Y. Kuramoto and H. Nakao, On the concept of dynamical reduction: the case of coupled oscillators, *Philosophical Transactions of the Royal Society A: Mathematical, Physical and Engineering Sciences* **377**, 20190041 (2019).
- [226] H. Nakao, Phase reduction approach to synchronisation of nonlinear oscillators, *Contemporary Physics* **57**, 188–214 (2015).
- [227] B. Pietras and A. Daffertshofer, Network dynamics of coupled oscillators and phase reduction techniques, *Physics Reports* **819**, 1–105 (2019).
- [228] R. Gutiérrez and R. Cuerno, Nonequilibrium criticality driven by kardar-parisi-zhang fluctuations in the syn-

- chronization of oscillator lattices, *Physical Review Research* **5**, 023047 (2023).
- [229] A. Kamenev, *Field theory of non-equilibrium systems* (Cambridge University Press, 2023).
- [230] L. M. Sieberer, G. Wachtel, E. Altman, and S. Diehl, Lattice duality for the compact kardar-parisi-zhang equation, *Physical Review B* **94**, 104521 (2016).
- [231] A. Zamora, L. M. Sieberer, K. Dunnett, S. Diehl, and M. H. Szymańska, Tuning across universalities with a driven open condensate, *Physical Review X* **7**, 041006 (2017).
- [232] L. M. Sieberer and E. Altman, Topological defects in anisotropic driven open systems, *Physical Review Letters* **121**, 085704 (2018).
- [233] P. A. Rikvold, H. Tomita, S. Miyashita, and S. W. Sides, Metastable lifetimes in a kinetic ising model: dependence on field and system size, *Physical Review E* **49**, 5080 (1994).
- [234] P. L. Krapivsky, S. Redner, and E. Ben-Naim, *A kinetic view of statistical physics* (Cambridge University Press, 2010).
- [235] J. Olejarz, P. L. Krapivsky, and S. Redner, Fate of 2d kinetic ferromagnets and critical percolation crossing probabilities, *Physical review letters* **109**, 195702 (2012).
- [236] C. Van den Broeck and M. Esposito, Ensemble and trajectory thermodynamics: A brief introduction, *Physica A: Statistical Mechanics and its Applications* **418**, 6 (2015).
- [237] K. Sekimoto, *Stochastic Energetics*, Lecture Notes in Physics (Springer Berlin Heidelberg, 2010).
- [238] J. A. Pachter, Y.-J. Yang, and K. A. Dill, Entropy, irreversibility and inference at the foundations of statistical physics, *Nature Reviews Physics* **6**, 382–393 (2024).
- [239] L. Onsager and S. Machlup, Fluctuations and irreversible processes, *Physical Review* **91**, 1505 (1953).
- [240] P. C. Martin, E. D. Siggia, and H. A. Rose, Statistical dynamics of classical systems, *Physical Review A* **8**, 423 (1973).
- [241] C. De Dominicis, A lagrangian version of halperin-hohenberg-ma models for the dynamics of critical phenomena, *Lettere al Nuovo Cimento* **12**, 567 (1975).
- [242] H.-K. Janssen, On a lagrangean for classical field dynamics and renormalization group calculations of dynamical critical properties, *Zeitschrift für Physik B Condensed Matter and Quanta* **23**, 377 (1976).
- [243] R. Kawai, J. M. R. Parrondo, and C. V. den Broeck, Dissipation: The phase-space perspective, *Physical Review Letters* **98**, 080602 (2007).
- [244] C. Nardini, É. Fodor, E. Tjhung, F. Van Wijland, J. Tailleur, and M. E. Cates, Entropy production in field theories without time-reversal symmetry: quantifying the non-equilibrium character of active matter, *Physical Review X* **7**, 021007 (2017).
- [245] S. Chen, D. S. Seara, A. Michaud, S. Kim, W. M. Bement, and M. P. Murrell, Energy partitioning in the cell cortex, *Nature Physics* **20**, 1824–1832 (2024).
- [246] B. Schönfisch and A. de Roos, Synchronous and asynchronous updating in cellular automata, *BioSystems* **51**, 123 (1999).
- [247] M. E. Cates, Active field theories (2019), [arXiv:1904.01330](https://arxiv.org/abs/1904.01330).